ÉCOLE DE TECHNOLOGIE SUPÉRIEURE
UNIVERSITÉ DU QUÉBEC

MANUSCRIPT-BASED THESIS PRESENTED TO
ÉCOLE DE TECHNOLOGIE SUPÉRIEURE

IN PARTIAL FULFILLMENT OF THE REQUIREMENTS
FOR THE DEGREE OF DOCTOR OF PHILOSOPHY
Ph. D.

BY
Longfei ZHAO

DESIGN AND VALIDATION OF A SYSTEM FOR CONTROLLING A ROBOT FOR 3D ULTRASOUND SCANNING OF THE LOWER LIMBS

MONTREAL, SEPTEMBER 3RD, 2015

BOARD OF EXAMINERS

THIS THESIS HAS BEEN EVALUATED

BY THE FOLLOWING BOARD OF EXAMINERS

Mr. Pascal Bigras, Thesis Supervisor
Automated Production Engineering Department at École de technologie supérieure

Mr. Ilian A. Bonev, Thesis Co-supervisor
Automated Production Engineering Department at École de technologie supérieure

Mr. Zhaoheng Liu, Chair, Board of Examiners
Mechanical Engineering Department at École de technologie supérieure

Mr. Vincent Duchaine, Member of the jury
Automated Production Engineering Department at École de technologie supérieure

Mr. Karim Khayati, External Evaluator
Department of Mechanical and Aerospace Engineering at Royal Military College of Canada

THIS THESIS WAS PRENSENTED AND DEFENDED

IN THE PRESENCE OF A BOARD OF EXAMINERS AND THE PUBLIC

AUGUST 24TH, 2015

AT ÉCOLE DE TECHNOLOGIE SUPÉRIEURE

ACKNOWLEDGMENTS

Foremost, I would like to thank my thesis supervisor Dr. Pascal Bigras, who has enlightened me a great deal in my research. Without his continuous support and guidance, the project could not have gone so far. He has also been a great mentor and dear friend throughout my research. I also express my gratitude to my co-supervisor Dr. Ilian A. Bonev, who provides and organizes an admirable working environment. His rigorous attitude to editing has improved the quality of the project's publications.

I would like to thank my colleagues who have assisted me in my project: Ahmed Joubair generously spent considerable time in helping me with robot calibration. Yousef Babazadeh Bedoustani shared his pertinent ideas on many problems during the project. Andy Kar Wah Yen spared me much initial preparatory work at the beginning of the project. Jonathan Coulombe helped with robot manufacturing/assembling, Yanick Noiseux helped with experiments, and there were many others. All of these remind me that any outcome of this project is a piece of teamwork.

Last but not least, I would like to thank my dearest family members, who consistently show their understanding and love, and replenish me with power and determination in times of difficulty.

CONCEPTION ET VALIDATION D'UN SYSTÈME DE COMMANDE D'UN ROBOT D'ÉCHOGRAPHIE 3D DESTINÉ AU BALAYAGE DES MEMBRES INFÉRIEURS

Longfei ZHAO

RÉSUMÉ

La maladie artérielle périphérique (MAP) est un problème circulatoire commun qui se manifeste habituellement par un rétrécissement artériel dans les membres inférieures. Sans approvisionnement sanguin suffisant, le patient peut souffrir de la claudication intermittente et peut même subir une amputation. Plusieurs personnes atteintes de la MAP ne le réalisent pas au premier stade. Par conséquent, le diagnostic devient très important.

Parmi les techniques d'imagerie médicale les plus courantes pour le diagnostic de la MAP, on retrouve l'échographie qui est une approche peu dispendieuse qui ne fait intervenir aucun rayonnement nocif pour la santé. Par contre, les radiologues et les techniciens qui utilisent régulièrement les échographes peuvent développer des troubles musculo-squelettiques à cause des mouvements qui doivent être appliqués à la sonde échographique. Qui plus est, les données obtenues à partir d'une échographie manuelle ne sont pas suffisantes pour reconstruire une image tridimensionnelle de l'artère, ce qui est nécessaire pour un diagnostic approfondi.

Les robots médicaux dédiés à l'automatisation de la prise d'échographies permettent de libérer le radiologue en plus de fournir des données précises pour la reconstruction d'une image tridimensionnelle de l'artère. Cependant, la plupart des robots d'échographie médicale existants ne sont pas adaptés au diagnostic de la MAP des membres inférieurs puisqu'ils sont conçus à d'autres fins.

Dans cette étude, nous présentons un robot d'échographie médical conçu spécifiquement pour le diagnostic de la MAP des membres inférieurs. La plate-forme robotique est d'abord présentée en détail. Les modèles cinématiques (directe et inverse) sont résolus grâce à la décomposition du robot parallèle en plusieurs sous-mécanismes simples. Les singularités et l'espace de travail sont également discutés.

Pour assurer la précision du système, le robot proposé est étalonné par des mesures directes des coordonnées de la sonde en utilisant un laser de poursuite. La méthode d'étalonnage utilisé est facile à mettre en œuvre sans nécessiter une connaissance avancée de l'étalonnage ni de calculs laborieux. Les résultats de cet étalonnage montrent que certaines erreurs sont occasionnées par la fabrication et l'assemblage de ce prototype. Néanmoins, l'étalonnage réalisé permet une amélioration significative de la précision du robot.

Un système de commande par admittance est ensuite proposé pour adapter la rigidité variable rencontrée lors de l'interaction humain-robot. Une utilisation intuitive de la théorie de la passivité est proposée pour garantir que le modèle d'admittance demeure toujours passif

malgré les variations des paramètres de masse et d'amortissement. Enfin, des analyses expérimentales impliquant une interaction avec un humain démontrent l'efficacité du système de commande proposé.

Mots-clés: robot médical, robot parallèle, maladie artérielle périphérique, diagnostic par échographie, étalonnage de robots, contrôle d'admittance, théorie de la passivité.

DESIGN AND VALIDATION OF A SYSTEM FOR CONTROLLING A ROBOT FOR 3D ULTRASOUND SCANNING OF THE LOWER LIMBS

Longfei ZHAO

ABSTRACT

Peripheral arterial disease (PAD) is a common circulatory problem featured by arterial narrowing or stenosis, usually in the lower limbs (i.e. legs). Without sufficient blood supply, in the case of PAD, the patient may suffer from intermittent claudication, or even require an amputation. Due to the PAD's high prevalence yet low public awareness in the early stages, its diagnosis becomes very important.

Among the most common medical imaging technologies in PAD diagnosis, the ultrasound probe has the advantages of lower cost and non-radiation. Traditional ultrasound scanning is conducted by sonographers and it causes musculoskeletal disorders in the operators. In addition, the data obtained from the manual operation are unable for the three-dimensional reconstruction of the artery needed for further study.

Medical ultrasound robots release sonographers from routine lifting strain and provide accurate data for three-dimensional reconstruction. However, most existing medical ultrasound robots are designed for other purposes, and are unsuited to PAD diagnosis in the lower limbs.

In this study, we present a novel medical ultrasound robot designed for PAD diagnosis in the lower limbs. The robot platform and the system setup are illustrated. Its forward and inverse kinematic models are solved by decomposing a complex parallel robot into several simple assemblies. Singularity issues and workspace are also discussed.

Robots need to meet certain accuracy requirements to perform dedicated tasks. Our robot is calibrated by direct measurement with a laser tracker. The calibration method used is easy to implement without requiring knowledge of advanced calibration or heavy computation. The calibration result shows that, as an early prototype, the robot has noticeable errors in manufacturing and assembling. The implemented calibration method greatly improves the robot's accuracy.

A force control design is essential when the robot needs to interact with an object/environment. Variable admittance controllers are implemented to adapt the variable stiffness encountered in human-robot interaction. An intuitive implementation of the passivity theory is proposed to ensure that the admittance model possesses a passivity property. Finally, experiments involving human interaction demonstrate the effectiveness of the proposed control design.

Keywords: medical robot, parallel robot manipulator, peripheral arterial disease, ultrasound diagnosis, robot calibration, variable admittance control, passivity theory.

TABLE OF CONTENTS

Page

LIST OF TABLES

Page

LIST OF FIGURES

LIST OF ABREVIATIONS

2D, 3D	two-dimensional, three-dimensional
ABI	Ankle Brachial Index
A/D	Analog to Digital converter
APA	Absolute Position Accuracy
CMM	Coordinate Measuring Machine
CTA	Computed Tomography Angiography
D/A	Digital to Analog converter
D-H	Denavit-hartenberg (table)
DOF	Degrees Of Freedom
F/T	Force and Torque
HIL	Hardware In the Loop
Hippocrate	Highly performing computer for robot-assisted surgery
ISO	International Organization for Standardization
LWR	Light Weight Robot
I/O	Input and Output
LTI	Linear Time Invariant
MedRUE	Medical Robot for vascular Ultrasound Examination
MRA	Magnetic Resonance Angiography
OTELO	mObile Tele-Echography using an ultra-Light rObot
PAD	Peripheral Arterial Disease
PC	Passivity Control
PID	Proportional Integral Derivative (controller)

PVL	Parameter Variation Law
RPA	Relative Position Accuracy
SMR	Spherical Mounted Retroreflector for laser tracker
TER	Tele-Echography Robot system
TERESA	from space research to ground tele-echography
US	UltraSound
w.r.t.	with respect to
WTA-2R	Waseda Tokyo Women's Medical Aloka Blood Flow Measurement Robot System No.2

LIST OF SYMBOLS AND UNITS OF MEASUREMENTS

c	virtual damping of admittance model in force controller of robot
$c_{\max}$	maximum value of c in deceleration
$c_{\min}$	minimum value of c in acceleration
c_r	reference value of c under constant speed
d_1	distance between O_i and A_i
d_2	offset between $O_0$and the robot symmetric line
d_3	offset between five-bar mechanism plane and the robot symmetric line
d_4	offset between five-bar mechanism plane and universal joint center
d_{ei}	offset between O_0 and E_i along x_0 axis
d_{fi}	offset between O_0 and F_i along x_0 axis
d_w	offset between O_0 and O_w along x_0 axis
f_h	interaction force between human and robot
g	dissipative power in passivity theory formula
g	gram
k	virtual stiffness of admittance model in force controller of robot
k_1, k_2, k_3	coefficients of time constant function
kg	kilogram
k_s	offset gain to keep a distance between Υ and estimated unstable region
l_{ij}	link length of j^{th} link of i^{th} five-bar mechanism
$l_{i\eta}$	distance between η^{th} measurement at P_i and average measured position of P_i
$\overline{l_i}$	average value of $l_{i\eta}$ in all n cycles measurement
m	virtual mass of admittance model in force controller of robot

m	meter
mm	millimeter
$\hat{m}$	modified virtual mass of admittance model after passivity control
$\tilde{m}$	modified virtual mass of admittance model after passivity control
$m_{\min}$	minimum virtual mass under certain virtual damping samples
m_{II}	instantaneous value of $m(t)$ when PC starts its execution
n	measurement times at each point in calibration
q_{Ai}	angle of l_{i1} in $\mathcal{F}_i$
q_{Bi}	angle of l_{i2} in $\mathcal{F}_i$
q_{Ci}	angle of l_{i3} in $\mathcal{F}_i$
q_{Di}	angle of l_{i4} in $\mathcal{F}_i$
q_i	joint value of actuators
$\tilde{q}_i$	joint offset errors of actuators
$\mathbf{p}_i$	measured coordinates of P_i
$\hat{\mathbf{p}}_i$	nominal coordinates of P_i
$\mathbf{p}_w$	coordinates of O_w w.r.t. $\mathcal{F}_0$
$\mathbf{p}_S$	coordinates of SMR w.r.t. $\mathcal{F}_0$
$\mathbf{r}$	3×1 vector between two three-dimensional points
rad	radian
s	second
t	time variable with unit of second
u	input of system in passivity theory formula

$\mathbf{u}$	unit vector
$\overline{x}_i, \overline{y}_i, \overline{z}_i$	average value of the coordinates of a point in multiple measurements
$\hat{x}_i, \hat{y}_i, \hat{z}_i$	command (reference) coordinates of P_i in calibration
x_{F1P}	offset of the $\mathcal{F}_P$ along x axis of $\mathcal{F}_w$
x_S, y_S, z_S	offset of the center of SMR w.r.t. $\mathcal{F}_w$
x_P, y_P, z_P	offset of the probe tip w.r.t. $\mathcal{F}_w$
x_W, y_W, z_W	offset of the origin of $\mathcal{F}_w$ w.r.t. $\mathcal{F}_0$
x_{Oi}, x_{O0Oi}	second coordinate of O_i w.r.t. $\mathcal{F}_0$
y	output of system in passivity theory formula
y_{Oi}, y_{O0Oi}	second coordinate of O_i w.r.t. $\mathcal{F}_0$
z_{F1P}	offset of the $\mathcal{F}_P$ along z axis of $\mathcal{F}_w$
z_{Oi}, z_{O0Oi}	third coordinate of O_i w.r.t. $\mathcal{F}_0$
α, β, γ	rotation along z,y,x axis respectively, the third, second and first variables of the expression of Euler angles (in order of Euler-XYZ)
$\alpha_W, \beta_W, \gamma_W$	Euler angles (in order of Euler-XYZ) of $\mathcal{F}_w$ w.r.t. $\mathcal{F}_0$
κ	threshold of virtual mass for chatter effect reduction in PC design
μm	micrometer
η	specified cycle of measurement in calibration
$\boldsymbol{\delta}_i$	relative displacement between two successive measured points based on measurement
$\hat{\boldsymbol{\delta}}_i$	nominal value of relative displacement between two successive measured points in calibration
θ_i	angle offset of $\mathcal{F}_i$ w.r.t. $\mathcal{F}_0$ in the five-bar mechanism plane

A_i, C_i	active joints of i^{th} five-bar mechanism, connection point between i^{th} five-bar mechanism and the robot base
B_i, D_i, E_i	passive joints of i^{th} five-bar mechanism
$\mathbf{D}_{x/y/z}(d)$	translation operation along $x/y/z$ axis with displacement of d
E	stored energy of the admittance model of robot
F_i	center of the i^{th} universal joint
$\mathcal{F}_0$	reference frame of robot base
$\mathcal{F}_i$	reference frame of i^{th} five-bar mechanism
$\mathcal{F}_L$	reference frame of the laser tracker
$\mathcal{F}_{Lij}$	reference frame of the robot link Lij
$\mathcal{F}_P$	reference frame of US probe tip
$\mathcal{F}_S$	reference frame of SMR in the calibration
$\mathcal{F}_w$	reference frame of the robot wrist
$\mathcal{F}_W$	world reference frame in the workspace
G_i	group of measurements in the multidirectional repeatability assessment
Hz	Hertz
K	Boolean flag of meeting the virtual mass threshold requirement
L_{ij}	j^{th} link of i^{th} five-bar mechanism
N	newton
Nm	newton-meter
N_i	nests of SMR on the robot for laser tracker measurement
O_0	the origin of robot base reference frame
O_i	the origin of reference frame of i^{th} five-bar mechanism

O_P	the origin of reference frame of probe tip
O_w	the origin of robot wrist reference frame
O_W	the origin of the world frame in work space
P	the execution state of passivity control
P_i	points in the target working space for the calibration
P_{Wi}	points to define the word reference frame in the target working space
Q_i	six actuators of the robot
$\mathbf{R}_{x/y/z}(\phi)$	rotation operation along $x/y/z$ axis with angle value of ϕ
${}^0\mathbf{R}_i$	rotation matrix of $\mathcal{F}_i$ w.r.t. $\mathcal{F}_0$
S	standard deviation in the formula of repeatability assessment
${}^0\mathbf{T}_i$	homogeneous transformation matrix of $\mathcal{F}_i$ w.r.t. $\mathcal{F}_0$
Υ	time constant function in the design of PVL of variable admittance model
Π	Boolean flag of active state of admittance model with parameters from PVL
Π^*	Boolean flag of meeting the criterion to execute passivity control
°	degree
$\vee$	logical OR operator
$\wedge$	logical AND operator
$\neg$	logical NOT operator

INTRODUCTION

Peripheral Arterial Disease – A serious condition of the arteries

Peripheral arterial disease (PAD) is a common vascular problem characterized by the obstruction of the blood flow in the arteries in limbs (Mohler, 2003; Ouriel, 2001). PAD usually develops in patient's legs, and the patient may suffer intermittent claudication (IC), or even amputation (Dormandy and Rutherford, 2000). Moreover, PAD can effectively predict cerebrovascular and cardiovascular problems (Criqui, Langer and Fronek, 1992; Hirsch, Criqui and Creager, 2001). Consequently, PAD is considered to be a manifestation of generalized arterial thrombotic disease, and its early diagnosis and treatment is very important. According to a non-invasive test on a population with average age 66, more than 10% of them had large-vessel PAD (Criqui et al., 1985). Another report revealed that 8% of men from 60 to 64 years old had a peripheral arterial occlusion (Widmer, Greensher and Kannel, 1964). Yet another study found a 14.3% prevalence for the disease in 666 men and women aged 60 (Schrolland Munck, 1981).

Request for a medical robot for peripheral arterial disease diagnosis

Preventive PAD examinations are quite important to protect patients from the serious consequences of the disease. There are already several ways to detect PAD, such as physical examination, the ankle-brachial index, segmental pressure and pulse volume recordings (Mohler, 2003). However, when it is necessary to pin-point occlusions more precisely or to fully characterize the morphologic features of occlusions, medical imaging techniques usually provide better results. Among the most common medical imaging techniques like angiography, ultrasound (US) scanning, computed tomography and magnetic resonance angiography, ultrasound outweighs the others due to the lower cost of its being a non-radiation technique (Norgren et al., 2007). Currently, most US examinations are manually operated by a sonographer. A survey has revealed that the repetitive strain of daily US examinations over many hours causes musculoskeletal disorders in sonographers (British

Columbia Ultrasonographer's Society, Healthcare Benefit Trust and Health Sciences Association, 1996; Vanderpool et al., 1993).

A medical US robot, however, can bear the load of the probe, and assist the sonographer in performing the PAD examination. Moreover, a medical US robot has the advantage of collecting the position data during the US scanning operation. Firstly, the robot obtains its joint position in real time from position sensors fixed on the actuator motors. Secondly, the position of the probe is calculated by the kinematic model of the robot. The US probe once calibrated, coordinates of the features of the US imagery are mapped onto the robot's workspace. This essential information can then be used for a three-dimensional (3D) reconstruction and further diagnosis. Much work has been undertaken in designing medical robots to perform US scanning, and they will be explored in the literature review in Chapter 2. However, most of them are designed to perform US scanning in the carotid or abdominal area. They are inadequate for PAD examination in the lower limbs due to the complexity of the arterial features in that area.

Project objective

The objective of this thesis is to provide a medical robot solution for a system to assist sonographers in performing PAD diagnosis in the lower limbs. A new medical robot prototype — the **Med**ical **R**obot for vascular **U**ltrasound **E**xamination (MedRUE) — is introduced to perform ultrasound scanning for PAD examinations of the lower limbs. The MedRUE is a parallel medical robot with six degrees of freedom (DOF). In this project, MedRUE will place an ultrasound U.S. probe to the desired location by providing reference coordinates, or under the guidance of the sonographer. The project objective can be demonstrated as three subtasks:

- Solve MedRUE's kinematic model, inverse kinematic model, and analyze the singularity issues and workspace
- Assess the repeatability and accuracy of MedRUE, and calibrate the kinematic parameters of MedRUE

- Design a motion and force controller to assist the sonographer in performing the PAD examination

Innovation & contribution

Based on our review of existing medical robots for ultrasound scanning, no sophisticated robot system has been designed for PAD diagnosis in the lower limbs. Consequently this thesis studies MedRUE, a prototype expressly designed for ultrasound scanning in the lower limbs. We demonstrate the distinctive kinematic model of MedRUE. Its complex parallel structure is deconstructed into four parts. With detailed study of each part, the kinematic solution is achieved in an easily-understood way.

A direct measurement method is used in the calibration of MedRUE. It requires no advanced calibration knowledge and is very practical and easy to implement. This approach identifies the parameters individually, and therefore reduces the nonlinear interference among parameters found in conventional calibration methods based on an optimization approach.

In MedRUE's force controller, a novel approach for integrating passivity theory and variable admittance control is demonstrated. On one hand, variable admittance control is a new approach in force control, but its stability issues remain uncertain for different parameter variation laws. On the other hand, passivity theory has been commonly used to ensure system stability in a conservative manner. We propose employing the passivity theory to ensure that the variable admittance controller possesses a passivity feature in a general way.

Organization

This thesis contains an introduction, four chapters, a conclusion and an appendix. The introduction briefly demonstrates the significance of this project and its contribution. Chapter 1 provides a comprehensive review of the project's three essential subject areas: the robot platform, calibration, and force control. Three articles, from Chapter 2 to Chapter 4

respectively, are presented to discuss the methods applied in these three areas. The conclusion summarizes the thesis, and introduces potential subjects for further development. The content of each Chapter and appendix is briefly outlined as follows:

Chapter 1. Literature Review: Background knowledge of PAD is first introduced, and then existing medical ultrasound robots are explored. We conclude that MedRUE is the unique medical robot expressly designed for PAD diagnosis in the lower limbs. We then discuss current knowledge and methods of robot calibration, as robots need the calibration process to meet certain accuracy criteria. Finally, the force control for the human-robot interaction in PAD diagnosis is reviewed at the end of the chapter.

Chapter 2. The kinematic analysis of a new medical robot for 3D vascular ultrasound examination: MedRUE — a robot dedicated to PAD diagnosis in the lower limbs — is presented in this chapter. The forward kinematic and inverse kinematic solutions are provided, together with the methods based on its intuitive geometric design. Its singularity issues and workspace are discussed at the end.

Chapter 3. Metrical evaluation of a novel medical robot and its kinematic calibration: A kinematic model for the calibration of MedRUE is provided with parameter errors. Its repeatability and accuracy are assessed before calibration. Then, the calibration method, which is based on direct measurement with a laser tracker, is presented. The calibrated parameters are provided, and the validation results show the improvement after calibration.

Chapter 4. A new passivity-based approach to the stability design of a variable admittance control: An admittance control with variable parameters is developed for human robot interaction, as the stiffness of humans varies according to muscle stimulation. The passivity theory is integrated into the variable admittance control to restrain the admittance model into remaining passive. The accompanying experiment shows that the proposed control can successfully retrieve the passivity property when the system attempts to be active.

Appendix I. Motion controller design of MedRUE: The dynamics of MedRUE is briefly introduced. Then , the design of motion controller is demonstrated. The motion controller of MedRUE consists of three parts: PID controller, friction compensator and gravity compensator. The appendix complements additional information which is not included in the Chapters.

CHAPTER 1

LITERATURE REVIEW

1.1 Introduction to peripheral arterial disease and its diagnosis

1.1.1 Definition of peripheral arterial disease and its prevalence

The circulatory system, also named the cardiovascular system, allows blood to circulate and transport nutrients, hormones, oxygen, et cetera. Humans have a closed network cardiovascular system consisting of arteries, which supply blood to the organs and extremities, and veins, which return blood to heart to be replenished with oxygen. Inside a healthy artery, the lining is smooth to promote a steady flow of blood. For certain reasons, the vessel walls may become sticky and substances in the blood start to accumulate on it, including fatty deposits, proteins, calcium, et cetera. A stenosis or thrombus forms in the artery after certain time. Then the artery is narrowed or progressively blocked, and nutritious are not able to arrive the organs and tissues. Peripheral arterial disease occurs and consequent symptom appears. Figure 1.1 illustrates the comparison between healthy artery and narrowed artery in PAD in lower limbs.

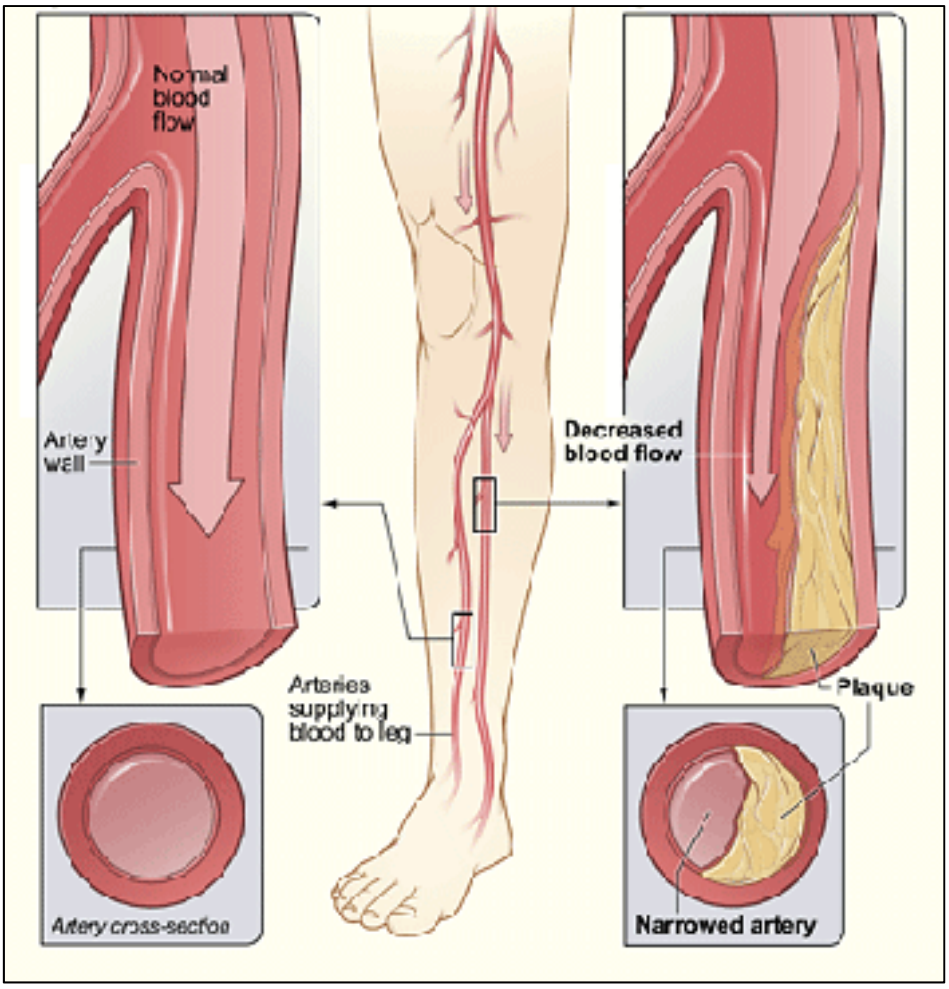

Figure 1.1 Comparison between healthy artery (left) and narrowed artery in PAD (right)
(Taken from https://www.nhlbi.nih.gov/health/health-topics/topics/pad)

PAD is a very common disease worldwide, and it has caught increasing public attention in recent years. Early research shows that the prevalence of PAD significantly increases with ages (Criqui et al., 1985), from less than 3% in under 60 years old to over 20% in over 75 years old. Numerous studies demonstrate the high prevalence of PAD (Criqui, Langer and Fronek, 1992; Gandhi et al., 2011; Gornik and Beckman, 2005; Hirsch, Criqui and Creager, 2001; Sharma and Aronow, 2012), and the result of one of them is illustrated in Figure 1.2. Moreover, a review based on 34 studies and 112 027 participants shows that the global prevalence of PAD increased by 24% between the year 2000 (164 million) and 2010 (202 million) (Fowkes et al., 2013).

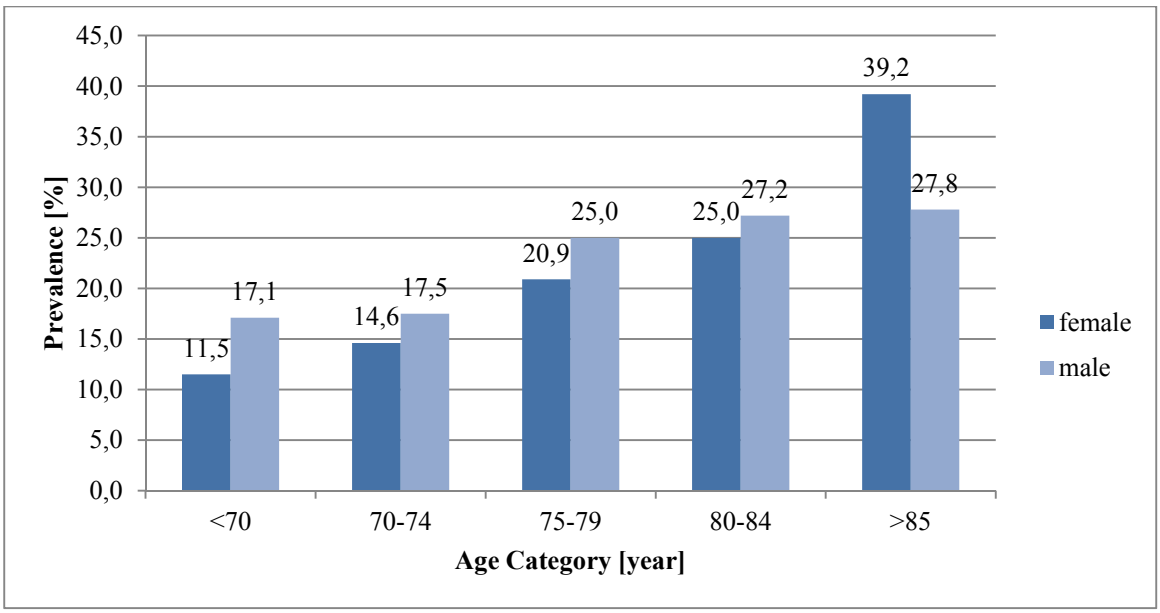

Figure 1.2 Prevalence of PAD by age and sex in 6880 patients (Diehm et al., 2004)

1.1.2 Symptoms and diagnosis of peripheral arterial disease

In terms of the high prevalence yet low public awareness of peripheral arterial disease, the condition is generally agreed to be the most underdiagnosed and least managed of the atherosclerotic diseases (Mohler, 2003). Approximately 40% of patients with PAD are asymptomatic, while 50% of patients have only atypical symptoms. Only 10% of patients have symptoms of intermittent claudication (Schirmang et al., 2009). As PAD develops more severely, arterial stenosis and occlusion may lead to critical limb ischemia or even gangrene (Minar, 2009). Table 1.1 shows the severity of PAD defined by Fontaine and Rutherford.

Early diagnosis is recommended to stop the development of PAD before intermittent claudication symptoms appear. Furthermore, the diagnosis of PAD predicates the presence of other arterial disease, such as coronary artery disease and cerebral artery disease (Hirsch, Criqui and Creager, 2001). PAD can be easily diagnosed by current technology, such as physical examination, the ankle-brachial index (ABI), segmental pressure and pulse volume

recording (Mohler, 2003). However, when it is necessary to locate occlusions precisely or to fully characterize the severity and morphologic features of occlusions, medical imaging techniques usually provide good results.

Table 1.1 The severity of PAD defined by Fontaine and Rutherford (Norgren et al., 2007)

Fontaine			**Rutherford**		
Stage	**Clinical**		**Grade**	**Category**	**Clinical**
I	Asymptomatic		0	0	Asymptomatic
IIa	Mild claudication		I	1	Mild claudication
IIb	Moderate to severe claudication		I	2	Moderate claudication
			I	3	Severe claudication
III	Ischemic rest pain		II	4	Ischemic rest pain
IV	Ulceration or gangrene		III	5	Minor tissue loss
			III	6	Major tissue loss

Table 1.2 provides a comprehensive list of medical imaging technologies that have been used or proposed for evaluating vulnerable plaque—the major cause of PAD and many other vascular diseases. The invasive methods used have become the traditional standard for vascular medical imaging. However, non-invasive technologies have the advantage of being painless and offering greater comfort during the examination. Among the non-invasive methods shown, computed tomography (CT) and nuclear scintigraphy produce medical images by radiation, which potentially raises the risk of complications. Magnetic resonance angiography (MRA) is free of radiation and, like computed tomography, is able to provide high-resolution 3D imaging (Chan, Anderson and Dolmatch, 2010). However, MRA equipment is very expensive and it consequently raises the cost per patient. In the case of PAD, patients are encouraged to undergo examination on a regular basis. To that end, ultrasound scanning scores over other non-invasive technologies in being low cost and free of radiation.

Table 1.2 Imaging modalities to evaluate vulnerable plaque (Lau et al., 2004)

Imaging Modality	Spatial Resolution(μm)	Vessel Wall Penetration (mm)	Features Detected						Comments
			Image of vessel wall	Fibrous Cap	Lipid Core	Inflammation	Calcium	Thrombus	
Invasive Methods									
Angiography		NA	√				√	√	Reference standard for stenotic lesions
Intravascular Ultrasound	40~100	~10	√	√	√		√	√	Characterizes vessel wall and morphology; good for calcified plaque, poor for lipids
Angioscopy	Visual	Poor	√	√	√			√	Affords direct visualization of the lumen surface, using colour and surface appearance to identify vulnerable plaques
Optical Coherence Tomography	2~30	1~2		√	√	√	√	√	Provides cross-sectional images of the vessel wall and quantifies fibrous cap thickness and the extent of lipid collections
Thermography	500	Poor							Images temperature heterogeneity due to rises in temperature in macrophage-rich areas in plaque
Raman Spectroscopy	NA	1~1.5		√	√	√	√		Analyzes the Raman spectrum for the chemical composition of atherosclerotic plaque
Near infrared Spectroscopy		2							
Intravascular MRI	160	Good		√	√	√	√	√	Measures cap thickness and characterizes atherosclerotic lesions
Non-invasive Methods									
Surface Ultrasound	**400**	**Good**	√	√	√		√	√	**Characterizes vessel wall and morphology; good for calcified plaque, poor for lipids**
Computed Tomography		NA					√	√	More useful for the detection of calcified plaques
Nuclear Scintigraphy		NA			√			√	Based on the specific binding of radioactive-labeled molecules to the target tissue
Standard MRI	300	Good		√	√	√	√	√	Measures cap thickness and characterizes atherosclerotic lesions

1.2 Medical ultrasound robots for diagnosis of peripheral arterial disease

Traditional ultrasound scanning, such as B-mode scanning, does not map stenosis in the 3D required for further treatment such as an intervention. Some enhanced 3D/4D ultrasound probes can obtain 3D images in a localized area, but operators are still needed to perform the scan through over the lower limbs. The medical image and the corresponding position of the probe are essential for 3D reconstruction of interested artery. However, the position data of the probe is lost when sonographers manually perform the US scanning. Furthermore, sonographers suffer from musculoskeletal disorders due to constantly repeating the procedure over time, and the strain of holding the equipment (Craig, 1985; Vanderpool et al., 1993).

According to a survey of 232 sonographers, work-related musculoskeletal symptoms are high, and two thirds have to seek medical help for their symptoms (Evans, Roll and Baker, 2009). Those sonographers who examine PAD in the lower limbs are even more at risk of suffering from musculoskeletal disorders as the procedure takes longer than others.

Medical robots have therefore been developed to assist human beings in various health issues (Speich and Rosen, 2004). Performing ultrasound scanning with robots has the following advantages:

i. Robots offer high degrees of precision, dexterity and repeatability. Furthermore the US images can be easily paired with the pose (position and orientation) data. This information is essential to carry out the 3D reconstruction required for further intervention.
ii. The robot releases sonographers from the physical strain of a lengthy operation procedure, and therefore protects them from potential risk of musculoskeletal disorders.
iii. The medical US robot system can be controlled remotely. This provides a solution in long-distance medical assistance where no medical experts are present.

Many US scanning robots have been designed for various implementations (Priester, Natarajan and Culjat, 2013). Some representative projects are reviewed in the following subsections. Grouped by the area scanned, most medical US robots are designed to perform examinations in the abdomen, neck and lower limbs. General information on these robots is introduced as follows, and their capabilities for PAD scanning are summarized.

1.2.1 Medical ultrasound robots designed for chest and abdomen area diagnosis

Portable ultrasound robots are easily placed on the scanning area, but their workspace of the robot itself is quite limited. TERESA is tele-echography project, which allows experts on a master site to control a medical US robot on a slave site (Arbeille et al., 2003; Gourdon et al., 1999; Vieyres et al., 2003). Later, OTELO, a European project based on the TERESA system

was proposed. In the OTELO system, the master site and the slave site communicate via satellite or 3G network. In addition, OTELO has 6-DOF as opposed to 4-DOF in TERESA (Courreges, Vieyres and Istepanian, 2004; Vieyres et al., 2006). As a result, extra translation motion has been added to extend the flexibility of the control from the master site.

Figure 1.3 The TERESA robot in US scanning, held by a paramedic
(Vieyres et al., 2003)

As illustrated in Figure 1.3, portable medical ultrasound robots have the advantage over other robots of easier storage and displacement (Vieyres et al., 2003). However, a paramedic has to hold the robot during the scanning process. The robot system is about 3kg in weight, which can cause fatigue and distraction to the paramedic after a lengthy session. In the long run, the paramedic has a high risk of suffering from musculoskeletal disorders. Moreover, the corresponding position of the robot when US image is recorded remains unknown.

Kohji Masuda and his colleagues have developed a medical ultrasound robot for abdominal examinations (Masuda et al., 2001a; Masuda et al., 2002). The US robot consists of a gimbal mechanism, a pantograph mechanism and a slide mechanism as shown in Figure 1.4. The probe is fixed on the gimbal, which provides orientations through 3 independent motors. The 3-DOF translations are achieved by two symmetric pantograph and slide mechanisms. A motor is located at the bottom of the each of the two pantograph mechanisms. Latitudinal or altitudinal translation is controlled by driving the two pantograph mechanisms in the same or opposite directions. Longitudinal translation is controlled by the slide mechanism.

Figure 1.4 Medical US robot from Ehime University, Japan
(Masuda et al., 2002)

The medical US robot from Ehime University frees the sonographer or paramedic from the exertion of holding the equipment. However, the robot's load is transferred to the patient, who has to bear the entire robot's weight (about 3.3kg) during the examination. This may lead to an unpleasant experience for specific patients, such as the elderly or pregnant women.

The cable medical ultrasound robot, TER, is another featured robot developed for US scanning in the abdomen (Gonzales et al., 2001; Martinelli et al., 2007; Vilchis et al., 2002). This particular cable-driven robot is lightweight and semi-rigid. It consists of four straps on four corners and a gimbal in the center as shown in Figure 1.5. The four straps are connected to the gimbal mechanism and control the translation motion in the horizontal plane. The gimbal mechanism is a serial robot with four independent motors. Three of the motors control the orientation of the probe, and the last motor controls the translation motion along the probe axis.

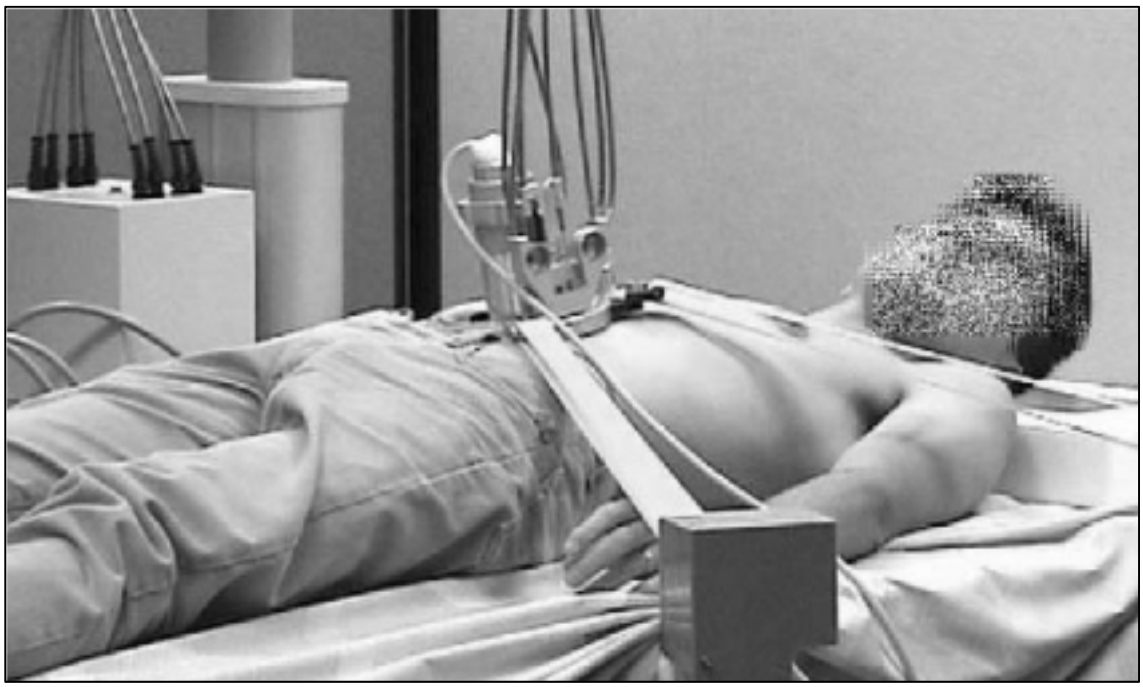

Figure 1.5 The cable US robot TER on a patient
(Vilchis et al., 2003)

TER's advantages lie in its compact and light design in relation to its large workspace. However, the system is only capable of performing US scanning on a flat surface. The non-rigid property of the cables severely curtails the precision of the robot as well. Experiment results (Vilchis et al., 2003) show that the error of the translation motion is around ±20mm. Therefore, the TER system can hardly provide reliable and precise data for further treatment.

1.2.2 Medical ultrasound robots designed for neck area diagnosis

WTA-2R has a 6-DOF serial link passive arm and a 6-DOF parallel link manipulator (i.e. probe holder) as shown in Figure 1.6. In the serial passive arm, each joint is equipped with a magnetic brake. When the power of the brakes is cut off, the joints are locked for safety. A gravity compensation mechanism is also implemented in the passive arm. The parallel probe holder is attached to the end of the passive arm. The parallel manipulator consists of six serial legs, and each leg is composed of a linear actuator, a universal joint and a spherical joint.

Figure 1.6 WTA-2R, a robot system for carotid ultrasound diagnosis (Nakadate et al., 2009)

The sonographer holds the passive serial arm to place the parallel probe holder close the area to be examined, and then locks the passive arm. Next, he controls the parallel probe holder to perform the US scan. However, the workspace of the parallel probe holder is very small

when the passive serial arm is locked. The robot is suitable for carotid area scanning, but not for larger areas. If the serial arm is actuated, the system will become a 6-DOF parallel robot mounted on a 6-DOF serial robot. Consequently the redundancy will be very high and the controller design will be very complex.

Hippocrate (HIghly PerfOrming Computer for Robot-AssisTEd Surgery) project employs an industrial robot (PA-10 from Mitsubishi Heavy Industry) for medical ultrasound scanning (Pierrot et al., 1999). It is a 6-DOF manipulator hanging above the patient as shown in Figure 1.7. Redundant resolvers and brakes are equipped on certain joints for safety. A Harmonic drive is mounted on each motor output shaft to limit the motion velocity. The action of the foot pedal authorizes any motion of the robot in joint space or Cartesian space.

Figure 1.7 The Hippocrate medical robot
(Taken from http://www.goetgheluck.com/REPORT/robots/report-fr/xxx_3of3.html)

The manipulator for Hippocrate was validated on phantoms of vascular carotid (neck artery), but the workspace is not well suited to performing ultrasound scanning of the lower limbs. It can only cover the femoral area, rather than the complete leg artery. Furthermore, the control system is limited to enslave the probe to follow a trajectory interpolated between the initial

and final tapes. This is sufficient for the carotid artery which is short and straight, but inadequate for the lower limb artery which is long and curved in 3D.

Figure 1.8 A fully-balanced medical US robot from University of British Columbia (Abolmasesumi et al., 2002)

Figure 1.8 features a medical ultrasound robot with its fully balanced design. Three adjustable counterweights are used to balance the weight of the link. This fully-balanced design, while alleviating the danger of unexpected power cuts, obviously adds extra weight to the platform. The robot's probe can tilt ±75° around the patient's neck axis, and less than ±50° around the patient's shoulder axis, which can fulfill the requirements of a carotid artery check. The translation range of the robot is less than 15 cm in each direction. However this small displacement is not sufficient for performing US scanning of the lower limbs.

1.2.3 Medical ultrasound robots designed for lower limb diagnosis

A medical imaging system was built to evaluate the positioning and inter-distance accuracies of ultrasound scans of the lower limbs (Janvier et al., 2008). The evaluation is based on an industrial serial robot arm (F3 from CRS Robotics Corporation) as shown in Figure 1.9. The robot has 6-DOF and a force sensor at its end-effector. In the teach mode, the force and torque information acquired by the force sensor generates a trajectory for the robot. In the relay mode, the saved trajectory is transmitted to the robot's controller to repeat the corresponding motion. Meanwhile, the 2D US probe takes images and saves them for further 3D reconstruction.

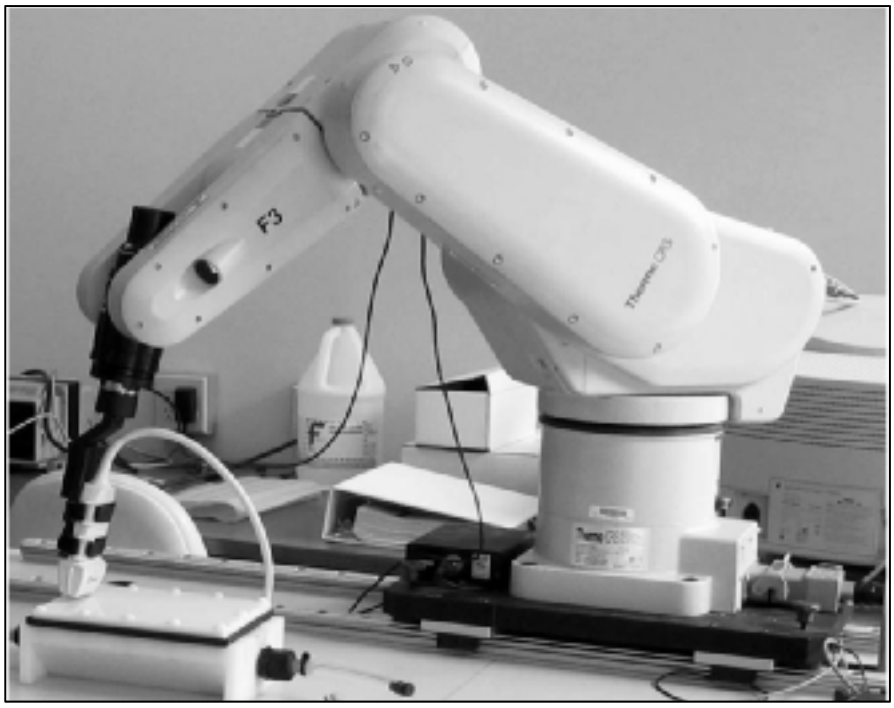

Figure 1.9 Prototype of a medical US robotic imaging system at the University of Montreal
(Janvier et al., 2010)

The project's objective is to evaluate the accuracy of medical ultrasound robot imaging systems. The robot platform is an industrial robot, whose mechanical structure is predefined for general use and whose controller is sealed against customized development. Though the

metrological evaluation is performed on a phantom of lower limb, the robot has to be relocated to predefined positions to cover the entire lower limb workspace.

Figure 1.10 Prototype for MedRUE

MedRUE (**Med**ical **R**obot for vascular **U**ltrasound **E**xamination) is a prototype of a medical parallel robot designed expressly for PAD diagnosis in the lower limbs (Zhao et al., 2013). The initial concept of MedRUE is being proposed based on optimizing its mechanical design to cover the lower limbs (Lessard, 2008). To that end, MedRUE is a 6-DOF parallel robot which can cover the entire lower limb area during the medical US scanning process. MedRUE consists of four parts, namely *the mobile base*, two *five-bar mechanisms* and *the tool part* as shown in Figure 1.10. Under the mobile base, a linear guide is fixed in the workspace, aligning lengthwise with the patient's leg. The U-shaped robot base is mounted on the linear guide, and the remaining structure of MedRUE is built on the robot base. The five heaviest motors are installed on the robot base and linear guide, and only the lightest

motor is sustained by the robot links. The “motor-on-base” design allows the robot links to be lightweight, and thus agile and safe to control. The two five-bar mechanisms are symmetrically assembled on the robot base, and they are linked by the tool part. The synchronized and unsynchronized motions of these two five-bar mechanisms result in the translation and orientation of the tool part respectively. A six-channel force sensor is mounted on the tool part, where connecting with the dummy probe. Safety issues are also taken into account in the robot's design. In line with research on static balancing (Lessard, Bigras and Bonev, 2007), the torque spring has been chosen as the optimal solution due to its simplicity of installation, lightness in weight and its linear property in computation.

1.2.4 Summary of medical ultrasound robots

To conclude the review of medical ultrasound robots, quite a few projects have been devoted to ultrasound scanning in lower limbs, where PAD mostly occurs. However, most existing medical US robots are designed for the US scanning of the chest, abdomen and neck areas. The features of different categories of medical US robots are summarized below:

- The robots dedicated to US scanning in the chest and abdomen areas have a flat scanning surface. They are designed to cover a large and flat working space, rather than fulfill the dexterity requirement for US scanning in the lower limbs. Their gimbal mechanism has the advantage of easily controlling orientation, but it also reduces the robot's dexterity in narrow areas, such as the lower limbs.
- The robot designed for US scanning in the neck area has a very limited workspace, which is sufficient for the carotid artery. However, the lower limb artery is much longer and twisted, and beyond the capability of a medical US robot developed for the carotid artery.
- The robot designed for US scanning in the lower limbs must have a long workspace, to cover the entire lower limb artery. The geometric structure of the robot needs to be more complex to track the twisted artery.

Up until our review, there has been no dedicated medical robot design for US scanning in the lower limbs, except the MedRUE prototype — the robot studied in our project. More information on MedRUE is provided in Chapter 2.

1.3 Review of the robot's calibration

Robot calibration is very important in applications requiring reliable accuracy. The calibration of a medical ultrasound robot involves both probe and kinematic calibration. The probe calibration identifies the constant transformation between the probe body and the US images (Kim et al., 2013; Lindseth et al., 2003; Mercier et al., 2005). It is more highly related to the US imaging system in the examination, than to the properties of the robot itself. This thesis focuses on the kinematic calibration, which determines the geometric property of the robot platform. The kinematic calibration of medical robots is similar to robots used in other fields, though the requirements vary according to their applications. The geometric calibration of the robot may depend on both the individual implementation and the robot platform. However, in general, it is divided into four steps (Khalil and Dombre, 2004):

i. Mathematical modeling of the robot with geometric parameters and joint values
ii. Position data measurement in predefined robot configurations
iii. Parameter identification
iv. Parameter error compensation in the robot model

In this review of robot calibration, certain important concepts of robot calibration are first introduced, followed by the methods for the four calibration procedures.

1.3.1 The robot's repeatability, accuracy and causes of accuracy error

Robots are generally required to meet certain metrological criteria, such as repeatability and accuracy. Position repeatability and accuracy are common essential features for fulfilling robotic tasks. The position repeatability describes the robot's ability to return to the same

position, while the position accuracy describes its ability to reach a given reference position. In most cases, the position accuracy is evaluated with respect to (w.r.t.) the world frame or the robot base frame by default. Therefore, it is also called the absolute position accuracy. In certain cases, relative accuracy is invoked to demonstrate the accuracy between each position. Absolute accuracy and relative accuracy are bundled, but they emphasize on different features of the robot. When the global coordinates of the robot are being considered, the absolute accuracy shows the ability to achieve the reference position in a straightforward manner. When the step motion from the previous position is more important, the relative position accuracy is preferred. Repeatability is considered to be the most important feature of industrial robots. These robots normally perform much better in repeatability than accuracy. As a rule of thumb, the position errors are about 0.5% of the robot's dimensions, or at least five times larger than its repeatability (Kirchner, Gurumoorthy and Prinz, 1987). The achievable repeatability of current industrial robots is below 100μm, while the standard robot accuracy ranges between 5mm and 15mm (Fixel, 2006).

For medical ultrasound scanning applications, the robot should meet certain accuracy to assist an experienced sonographer. The 3D reconstruction of the artery after scanning also has an accuracy requirement. There are no standard accuracy criteria for medical US robots. However, some accuracy specifications of existing medical US robots are provided as a reference. The TER cable robot has an accuracy of about 20mm for general inspections. The industrial robot in the Hippocrate project has an accuracy of about 0.5mm (Pierrot et al., 1999). The accuracy of the parallel manipulator of WTA-2R is 0.1mm within a distance of 5mm (the workspace is 10mm). Twenty-five medical US robots for needle guided ultrasound are listed in (Priester, Natarajan and Culjat, 2013), and much of their accuracy ranges from 1mm to 3mm. The robot used to evaluate US scanning performance in the lower limbs provides a pertinent reference (Janvier et al., 2010). Its accuracy ranges from 0.46mm to 0.75mm.

Accuracy depends on many geometric and non-geometric aspects that are listed in Table 1.3. The geometric causes demonstrate the static differences between the designed model and the

real robot platform. In the model's design phase, tolerance is introduced to secure certain precision in the machining process. Very strict tolerance is hard to achieve, and it raises the cost of manufacture. Thus, tolerance is an unavoidable source of accuracy error in the robot. Also, in the manufacturing and assembling phases, errors either by the machines or machinists are inevitable. Some common are as follows: the robot links have different lengths from their nominal values; the robot base has a different dimension; the joint axes are not aligned in the assembling, et cetera. The joint values can have offsets due to the resolution of encoders and other facts. Inaccurate representation of the world frame and the base frame will also add global errors in the workspace.

Table 1.3 Causes of robot in accuracy

Geometric	**Non-Geometric**
Link length manufacuring inaccuracy	Joint compliance
Assembling position offsets	Backlash and Friction
Joint offsets	Model simplification, computing errors
World frame and base frame locations	Environment

Geometric facts are generally easy to handle by calibration methods, and they contribute more than 90% to the robot's inaccuracy (Costa and Smaby, 1997; Judd and Knasinski, 1990). By contrast, non-geometric facts are more complex and difficult to model. They may vary depending on the load, running time, environment, et cetera. Some non-geometric facts can be calibrated, but generally at more cost than geometric facts and with less profit. Therefore, in this thesis, the calibration of geometric parameters is reviewed, and non-geometric facts are considered as randomly-distributed errors.

1.3.2 The robot's kinematic model

A robot's geometric model is essential to the robot's calibration. The nominal kinematic model derives from the design phase of the robot. This being the case, the components have

ideal dimensions and the assembling of each component is error free. The kinematic model for calibration is built to include geometric errors in manufacturing and assembling, et cetera. These geometric errors are represented by parameters, whose values will be optimized with the calibration methods introduced in subsection 1.3.4.

Among the notations for illustrating a robot's kinematic model, the Denavit-Hartenberg (D-H) table is the most widely used to describe open serial robots (Denavit, 1955). The D-H table was further developed for adapting more complex parallel robots in (Sheth and Uicker, 1971). Alternative notations for general robots such as the S-model are used (Stone, 1987) and the Zero-reference model. However, some parallel robots are represented according to their instinctive geometric structures, rather than their general characteristics.

1.3.3 Measurement methods in calibration

Few calibration measurements are completed by the inner structure of the robot. However, with inner sensors, the robot can be calibrated with no need for external equipment (Hanqi, 1997; Klodmann et al., 2011; Yang et al., 2002). Nevertheless, the manufacturing process and the robot model will be more complex. Moreover, most robots only need to be calibrated a few times in certain cases. Therefore, installed redundant sensors will not be used in most working phases.

Most calibration measurements are completed by external measuring equipment. The most common categories of calibration measuring equipment are: laser-based systems (Bai, Zhuang and Roth, 2003; Lei et al., 2004; Xueyou and Shenghua, 2007), stereo vision-based systems (De Ma, 1996; Deep et al., 2013; Zhuang and Roth, 1996; Zhuang, 1994) and mechanics-based systems (Driels, Swayze and Potter, 1993; Joubair, Slamani and Bonev, 2012b; Wu et al., 2011). Figure 1.11 shows three products of these three different types.

As shown in Figure 1.11(a), the laser tracker head emits a laser beam, which is then reflected back to the receiver on the head by a mirror reflector. This laser-based measuring system has

the advantages of long range and high accuracy. It can measure distances over 50m, and the head can track the target through very large angle variations. The distance accuracy of the FARO ION laser tracker is 8μm + 0.4μm/m, and the angular accuracy is 10μm + 2.5μm /m. However, the reflector's orientation must always be visible to the laser tracker while the robot is in motion.

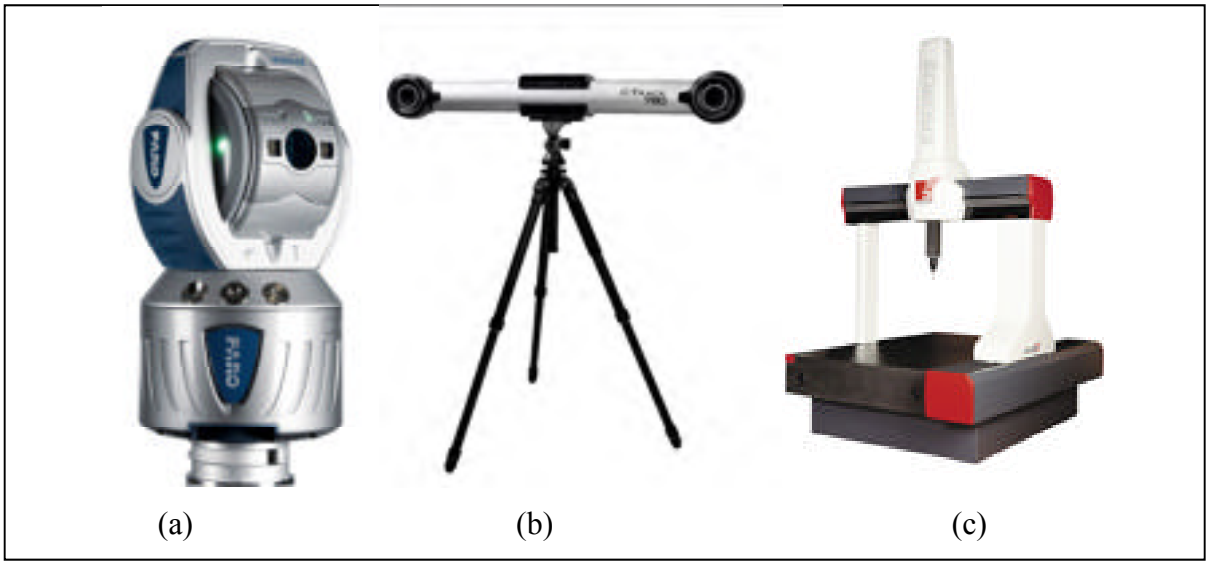

Figure 1.11 Calibration measuring equipment. (a) Laser-based: FARO laser tracker; (b) Stereo vision-based: CreaForm C-Track ; (c) mechanics-based: COORD3 coordinated measuring machines
(Taken from http://www.deskeng.com/de/faro-launches-vantage-portable-3d-laser-tracker/; http://www.creaform3d.com/en/ndt-solutions/c-track; http://www.cmm-metrology.co.in/large-coordinate-measuring-machine/)

The stereo vision-based system has multiple cameras taking images in real-time. Computer vision technology compares the images from different cameras and produces position information w.r.t. the camera frame. Specified markers are often provided to enhance light reflection. The accuracy of the stereo vision system is generally lower than that of the laser-based system (Creaform C-Track 78 in Figure 1.11(b) has an accuracy of 25μm), and accuracy may suffer in poor light conditions. Nevertheless, the stereo vision system has the advantage of measuring multiple targets at the same time. This is a significant merit when great amounts of measuring targets are needed, such as the point cloud for reverse-engineering.

The mechanics-based measuring system uses a probe to physically touch the measured object. Such mechanical measuring systems are assumed to be precisely manufactured and modeled. When the probe touches the target object, the value of each joint is recorded and the position of the probe is obtained based on the forward kinematic model of the mechanical system. The mechanical measuring system is reliable and less influenced by the environment. However, the workspace of this system is quite limited due to its dimensions. The coordinate measuring machine (CMM) in Figure 1.11(c) is highlighted for its decoupled translation structure, and it shows measurements directly in Cartesian space. Other mechanical measuring systems such as the FaroArm series have a light and portable passive arm. The accuracy of CMM in Figure 1.11(c) is below 5μm, while the passive FaroArm reaches 50μm.

1.3.4 Review of parameter identification methods

Kinematic calibration methods in serial robots are mostly for identifying D-H parameters (Mooring, Driels and Roth, 1991; Roning and Korzun, 1997). However, the calibration methods of parallel robots vary depending on the different geometric structures of parallel robots. Calibration methods have been studied for various parallel robots, such as planar robots (Joubair and Bonev, 2013; Joubair, Slamani and Bonev, 2012a), Gough-Stewart platform (Nahvi, Hollerbach and Hayward, 1994b; Ren, Feng and Su, 2009; Zhuang, Yan and Masory, 1998) and Delta robots (Maurine and Dombre, 1996; Traslosheros et al., 2011).

Identification problems are usually in finding the optimized values for parameters to minimize the position error of the robot. Conventional ways to identify the geometric parameters involve the least square optimization procedure. The linearized approach converges more rapidly, but it may encounter the ill-condition of the identification Jacobian. Various nonlinear algorithms have been implemented to solve calibration optimization problems, such as the Levenberg-Marquardt algorithm (Bennett and John, 1991), the Gauss-Newton algorithm (Guillaume and Pintelon, 1996; Maye, Furgale and Siegwart, 2013), and the gradient-based algorithm (Baharin and Hasan, 1994; Nahvi, Hollerbach and Hayward,

1994a; Powell, 1964; Yamane, 2011). It is noteworthy that not all geometric parameters are identifiable. Khalil et al. propose a general method to determine identifiable parameters (Khalil and Dombre, 2004).

1.3.5 Compensation and implementation

By using the identification methods discussed in 1.3.4, optimal geometric parameters can be found for the kinematic model for calibration. The compensation step is, in concept, to implement the identified parameters into the kinematic model for calibration. This can be realized straightforwardly if both the forward and inverse kinematic models of the robot controller are fully accessible.

However, most manufacturers of robot products seal their controllers from users. In such cases, the kinematic parameters of the robot controller are unable to be directly updated. A way of overcoming this problem is by implementing the identified parameters in the inverse kinematic model as a preprocessor that is identical to the robot controller (Mooring, Driels and Roth, 1991). Another proposed method to compensate for kinematic parameter errors is by adding joint offsets (Dombre and Khalil, 2010). In this approach, the identified parameters are implemented in the forward kinematic model. Numerical algorithms, such as the Newton-Raphson method, have also been studied to find the joint offsets for compensating the position errors in Cartesian space (Kirchner, Gurumoorthy and Prinz, 1987; Mirman and Gupta, 1992).

1.3.6 Summary of robot kinematic calibration

The concept for the robot's calibration and the procedure steps are introduced in this section. Alternative methods are reviewed for accomplishing each stage of the calibration.

In the reviewed robot calibrations, the parameters are generally identified by using optimization methods. However, quite a few studies on calibration methods are based on

direct measurement. One such calibration method, based on direct measurement, has been used to calibrate the parallel robot MedRUE. The contribution of the proposed calibration method is elaborated in Chapter 3.

1.4 Force control in human-robot interaction

Conventional motion control is inadequate for human-robot interaction. The reference motion in motion control requires an accurate model of both robot and human limbs. The robot's model is discussed in 1.3.2, while the model of human limbs is often difficult to obtain. Meanwhile, interaction with the environment normally brings constraints to the robot's motion. If the desired position is unreachable, the motion controller forces the robot to continue until current saturation of the motors is reached, or the interactive parts are broken.

Force control is developed to regulate the robot's reaction during interactive encounters and can be generalized into two general categories, namely direct force control and indirect force control (Siciliano and Villani, 2000). Direct force control operates force feedback directly to compensate for interaction force errors, and aims to meet the accurate force requirement. A typical implementation of direct force control is the hybrid position/force control, which controls position in the unconstrained directions and the force in the constrained directions (Doulgeri, Fahantidis and Paul, 1998; Fisher and Mujtaba, 1992; Raibert and Craig, 1981). However, hybrid position/force control requires an accurate modeling of the environment, and it is intended for rigid surface contact (i.e. environments with high stiffness), rather than interaction with humans. In contrast, indirect force control associates the position error with the contact force through a virtual model. In most cases, the purpose of force control in human-robot interaction is to structure proper motion behavior under certain interaction forces, rather than to achieve a precise force value on an industrial level. Consequently, indirect force control is widely implemented in human-robot interaction. Stiffness control, impedance control and admittance control are the major topics of indirect force control, and they are discussed in 1.4.1. An adaptive concept is introduced to enhance the force

controller's interaction with a variable environment in 1.4.2. At the end of this section, stability issues are discussed, with an emphasis on a passivity-based approach, in 1.4.3.

1.4.1 Conventional force control in human-robot interaction

The human-robot interaction is often designed as a virtual mass-damping model. The stiffness control is implemented in a static robot-environment interaction. The impedance control demonstrates the dynamic properties of the interaction. Impedance control takes motion (position, velocity and acceleration) as input and generates a force. By contrast, admittance control takes force as input and provides motion as output, and it is considered the reverse of impedance control (Hayward and MacLean, 2007; van der Linde and Lammertse, 2003).

In the force controller design, the causes and effects of virtual mass-damping models can often be chosen arbitrarily, but different approaches will generate different performances and features (Lawrence, 1988; Yamada, Huang and Yabuta). Stiffness control is often used to achieve a static contact. Impedance control is preferred when the robot should act as a generalized spring with a rigid environment. Admittance control is implemented when the robot is considered as a generalized mass. There are plenty of research results in the literature on impedance control (Buchli et al., 2011; Cortesao, Sousa and Queiros, 2010; Dong et al., 2013; Hace, Jezernik and Uran, 1996), but fewer on admittance control (Augugliaro and D'Andrea, 2013; Newman and Zhang, 1994). Impedance control shows its advantages when interacting with high stiffness environments, but it does so with lower accuracy (Hayward and MacLean, 2007; Ott, Mukherjee and Nakamura, 2010). Given the low stiffness of humans, an admittance control approach has been chosen as the candidate force control for MedRUE.

1.4.2 Adaptive force control in a variable environment

In conventional force control, the parameters of the virtual model are constants in the interaction. However, conventional force control may present problems when the stiffness of the environment changes. If admittance control is taken as an example, the constant parameters of the admittance control will produce a sluggish response in a softer environment, while they may become unstable in a harder environment. More advanced force control is therefore required to adapt to an unknown or changeable environment.

Adaptive impedance/admittance control is gaining increasing attention in force control design. It can be designed for different purposes:

- To regulate the motion of robots with uncertain dynamic parameters in invariant environments (Chan et al., 1991; Tee, Yan and Li, 2010; Park and Lee, 2004).
- To regulate the motion of robots without dynamic models through neural network and function approximation techniques (Chien and Huang, 2004; Li et al., 2013).
- To enhance the performance of the robot's interaction with an unknown, but constant environment (Seraji, 1994).
- To enhance the performance of the robot's interaction with a varying environment. Adaptive laws are designed to modify the parameters of the admittance model in run-time.

In human-robot interaction, the stiffness and damping properties of human limbs vary as a result of complex muscular stimulation (Ikeura and Inooka, 1995). Consequently, adaptive impedance/admittance controls for varying environments have been explored. Schemas involving human cooperation have been analyzed and stiffness in humans has been evaluated (Ikeura and Inooka, 1995; Tsumugiwa, Yokogawa and Hara, 2002). Based on the stiffness estimation, a variable impedance controller was developed to drive the robot cooperating with the human.

A general model for human-robot cooperation was proposed based on variable impedance control (Duchaine and Gosselin, 2007). The differentiation of force was examined as a predictor of human intention, and it varies the parameters of impedance control. The result of this paper also reveals that the performance of velocity control overcomes position control in human-friendly robots. Another similar approach, but with variable admittance control, was proposed in (Lecours, Mayer-St-Onge and Gosselin, 2012). Rather than using force as the direct indicator of human intention, designed velocity and acceleration are used. In practice, a stable region is evaluated according to the instinctive dynamic property of the robot. The reference values for the admittance parameters are then defined based on the estimated stable region.

1.4.3 Stability issues in force control design

Stability is a key feature of controller design, and it is very important in controller implementation. In linear time invariant (LTI) systems, many sophisticated methods have been developed to guarantee system stability. In the design of a controller, the poles which cause instability in a system can be displaced to a desired position. The Root-Locus method and the Nyquist plot are very convenient methods for regulating a simple force controller (Eppinger and Seering, 1987; 1989; Tarn et al., 1996). The Proportional-integral-derivative (PID) control method and its variants can also be implemented to meet more advanced dynamic requirements through properly tuning the parameters. Pole placement methods have equally been developed for modern control approaches in state space (Ogata, 1997). However, stability analysis is generally very difficult in nonlinear or time-varying systems.

The stability analysis of various force controls is generally discussed in (Lawrence, 1988; Waibel and Kazerooni, 1991; Whitney, 1987; Zeng and Hemami, 1997). Linearization techniques are used to cancel the nonlinear dynamics of the robot, and stability can be achieved in the linearized system with sophisticated methods (Yoshikawa, Sugie and Tanaka, 1988). However, a linearization approach requires exact models of the robot and the environment. In force control, it is common to interact with an uncertain or varying

environment. Consequently, the nonlinearity of an adaptive law may be necessary to achieve the target property of the system. Therefore, advanced stability methods for nonlinear force control are needed. In the following content, two important approaches (i.e. The Lyapunov stability theory and the passivity theory) for nonlinear stability are introduced, and their implementations in force control reviewed.

The Lyapunov stability theory was originally proposed in 1892, and it has been widely used in nonlinear system design in recent decades (Lyapunov, 1992). There are two methods included in Lyapunov theory, but the second (or direct) method is more widely used and referred as the Lyapunov theory by default in most cases. The Lyapunov direct method determines the stability of a system without solving the state differential equations. This is the key feature of its popularity since state differential equations of nonlinear systems are very difficult to obtain in general.

In the Lyapunov direct method, if a system is asymptotically stable, its stored energy decreases until reaching a minimum value at the equilibrium state. A straightforward interpretation of the Lyapunov direct method is the fact that the energy of a vibratory system decays to its minimum at the equilibrium point. The proof and implementation of Lyapunov theory are detailed in many monographs (de Queiroz, 2000; Kurfess, 2005; Ogata, 1997; Slotine and Li, 1991).

The Lyapunov direct method is the fundamental stability analysis method in many interaction cases. It is implemented to analyze the stability of the robot's system when influenced by external forces (Wen and Murphy, 1991). The Lyapunov direct method is also used for more complicated cases, such as redundant manipulator (Khatib, 1987; Ott, Kugi and Nakamura, 2008), and multiple manipulator cooperation (Wen and Kreutz-Delgado, 1992). The Lyapunov direct method is also implemented in adaptive control (Siciliano and Villani, 2000) and robust control (Slotine, 1984).

Passivity theory is considered as another conservative approach to maintaining system stability from an energy viewpoint. A passive system is defined in (Slotine and Li, 1991), and passive systems have proved to be stable in a conservative approach (Bao and Lee, 2007; Sepulchre, Janković and Kokotović, 1997).

Conventional passive control in force controllers is achieved by designing a control law based on the estimation of the nonlinear system model. Its approach is similar to inverse dynamic control design. However, rather than fully cancelling the nonlinearity of the system, the passive control is designed to preserve the passivity property for the closed-loop system (Byrnes, Isidori and Willems, 1991; Kawai et al., 2011; Siciliano and Villani, 1996; Wimboeck, Ott and Hirzinger, 2006). This method has also been extended to the control of flexible robots (Albu-Schäffer, Ott and Hirzinger, 2007; Ott et al., 2008) and in modeling dynamic friction (Canudas-de-Wit and Kelly, 2007).

In recent years, a time domain passivity approach has been gaining increasing attention for its simple and intuitive control design strategy (Hannaford and Jee-Hwan, 2002; Jee-Hwan, Dong-Soo and Hannaford, 2004; Ryu, Kwon and Hannaford, 2004). If a system derives from a passive status (monitored by a passivity observer), the passivity control executes and modifies the system output to return the system to passive status. When the passivity controller is activated to retrieve the passivity property, there is a potential risk of generating a large pulse, which is undesirable in terms of system stability. This transient behavior is regulated by introducing reference-energy (Jee-Hwan et al., 2005). The time domain passivity approach to haptic human-robot interaction has been widely studied. (Gosline and Hayward, 2007; Hannaford and Jee-Hwan, 2002; Yongqiang et al., 2011).

1.4.4 Summary of force control in human-robot interaction

Force control design is an essential subject in human-robot interaction. It regulates the robot's behavior through the presence of an external interaction force. Conventional force control methods have been introduced for general interaction purposes, such as stiffness control,

impedance control and admittance control. For more uncertain or changing environments, variable parameters are employed in the force controller model to adapt to the varying environment. Diverse variation laws of model parameters have been discussed, and a general method for the stability of nonlinear systems is needed. The implementation of two celebrated nonlinear system stability analysis methods — the Lyapunov direct method and passivity theory — have also been reviewed.

In the reviewed research, there exists no implementation for integrating the passivity theory into a general variable admittance controller. This approach ensures the passivity of the variable admittance model regardless of the parameter variation law. The passivity based variable control design of MedRUE is illustrated in Chapter 4.

CHAPTER 2

KINEMATIC ANALYSES OF A NEW MEDICAL ROBOT FOR 3D VASCULAR ULTRASOUND EXAMINATION

Longfei Zhao, Andy Kar Wah Yen, Jonathan Coulombe, Pascal Bigras and Ilian A. Bonev
Department of Automated Manufacturing Engineering, École de technologie supérieure,
1100 Rue Notre-Dame Ouest, Montréal, Québec H3C 1K3

This paper has been published as an article in
Transactions of the Canadian Society for Mechanical Engineering
Vol. 38, No. 2 (2014), pp 227-239

Abstract

Peripheral artery disease (PAD) is a common vascular disease which can have serious consequences for older people. Owing to the complexity of the vessels in the lower limbs, current PAD medical robots are not desirable to diagnose PAD in this area. The kinematic model of a novel six-axis serial-parallel robot for 3D vascular ultrasound examination of the lower limbs is presented in this paper. The prototype of the robot is described, and then the direct and inverse kinematic problems are solved in closed form.

Keywords: serial-parallel robot; medical robot; kinematics.

2.1 Introduction

Peripheral arterial disease (PAD) is a very common, but serious disease that occurs in the lower limbs. It narrows, and can even block, the vessels that carry blood from the heart to the limbs (Ouriel, 2001). According to (Sharma and Aronow, 2012), the prevalence of PAD of a

group over 70 years old is nearly 15%, but only 10% of them have observable symptoms. If PAD is not detected and diagnosed in time, patients will suffer intermittent claudication, and the limb may even require amputation (Dormandy and Rutherford, 2000). Medical imaging techniques are generally used in the diagnosis of PAD to precisely locate blockages, or occlusions, and characterize their morphological features. Among the most common techniques, which include angiography, ultrasound scan, computed tomography angiography (CTA), and magnetic resonance angiography (MRA), ultrasound scan outweighs the others regarding to its non-radiation lower cost (Norgren et al., 2007).

Several handheld medical robots have been developed for PAD diagnosis using ultrasound imaging, such as TERESA (Arbeille et al., 2003; Vieyres et al., 2003) and OTELO (Courreges, Vieyres and Istepanian, 2004; Vieyres et al., 2006). This type of PAD robot requires quite a small workspace, and should be held by the technician during operation. A survey of 232 sonographers (Evans, Roll and Baker, 2009) has revealed that the repetitive strain of carrying this load over many working hours leads to musculoskeletal disorders. Several other robots have been developed for ultrasound imaging of the abdominal area, such as Ehime University's robot (Masuda et al., 2001a; Masuda et al., 2002) and a cable robot, TER (Martinelli et al., 2007). However, the abdominal area is flatter for ultrasound scan purposes than a leg, and the geometric design of these robots indicates that they are unsuitable for examining the lower limbs. The Hippocrate robot in France (Pierrot et al., 1999) and the fully statically balanced medical robot at the University of British Columbia (Abolmasesumi et al., 2002) are designed for PAD diagnosis in the carotid area, where the artery concerned is fairly short and straight. Finally, in (Lessard, Bigras and Bonev, 2007), we propose a new serial-parallel robot architecture for PAD diagnosis in the lower limbs, where blood vessels are long, complex, and twisted. That paper presents the architecture and a static balancing optimization for this robot, but its kinematic model is not analyzed, nor is its prototype presented.

This paper presents hardware setup and a detailed kinematic analysis of the new medical robot (MedRUE) shown in Figure 2.1(a), which is based on the architecture proposed in

(Lessard, Bigras and Bonev, 2007). MedRUE (Medical Robot for vascular Ultrasound Examination) is suitable for lower limb PAD diagnosis as shown in Figure 2.1(b), and the workspace covers the entire lower limb area that needs to be scanned. Moreover, the robot has sufficient dexterity to insert and rotate a probe in the narrow space of a lower limb. The remaining sections are organized as follows. In section 2, the robot specifications and setup are discussed in detail. In sections 3 and 4, we present the direct and inverse kinematics of MedRUE respectively. In section 5, we address the singularity issues. Our conclusions are given in section 6.

2.2 Robot architecture and hardware setup

MedRUE has a patented serial-parallel architecture (Lessard, Bonev and Bigras, 2010) designed to follow the complex and twisted structure of the artery in lower limbs. It can be regarded as comprising four components: a mobile base, two five-bar mechanisms, and a tool part as shown in Figure 2.1(b).

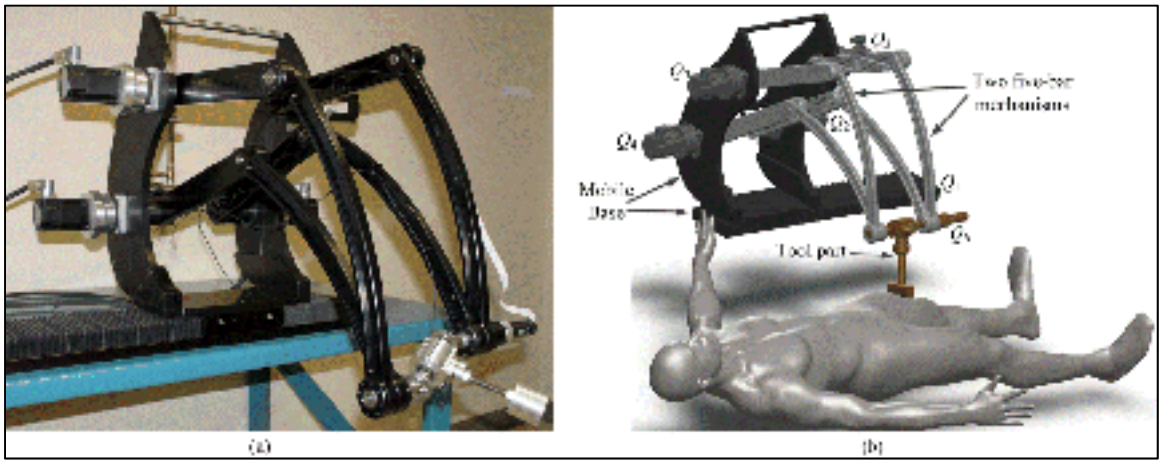

Figure 2.1 (a) MedRUE robot prototype; (b) MedRUE simulation

The mobile base is attached to the carriage of a LinTech 150 series linear guide. This allows MedRUE to translate along the x_0 axis off the base frame O_0, and it covers the length of a typical lower limb. This decoupled design has made it possible to minimize MedRUE's

dimensions. Furthermore, because four of its six motors are mounted on the mobile base, the rest links of the robot is relatively light and nimble.

The two symmetrical five-bar mechanisms are attached to the mobile base. They work in parallel planes perpendicular to the direction of the base linear guide. The combined motion of these two mechanisms enables the translation and orientation of the ultrasound probe along y_0 and z_0 axes.

Table 2.1 Specifications of the Main Components

	Mass	Length	Other features
Robot	45 kg	0.91 m (linear guide)	Full extension: 0.687 m
Five-bar mechanism inks			
actuated bars	0.68 kg	0.40 m	Inertia: 0.013 kg·m^2
passive bars	0.82 kg	0.52 m	Inertia: 0.024 kg·m^2
Tool part			
Telescoping double universal joint	0.90 kg	0.080 m	Radius: 0.030 m
force sensor and ultrasound probe	0.50 kg	0.176 m	Radius: 0.020 m

The tool part connects the extremities of the two five-bar mechanisms through two passive universal joints. A passive prismatic joint is located between the two universal joints to compensate for the change in distance between the two extremities of the five-bar mechanisms. A small motor is located on one of the mechanisms to drive the rotation of the tool part.

The general specifications of the robot and main components of MedRUE are listed in Table 2.1. They are based on of an optimal design for MedRUE workspace as detailed in section 5.

The main components are made of aluminum alloy 6061-T6, and the shafts and pins are fabricated with alloy steel 4140.

Table 2.2 MedRUE Motors and Drivers

Actuators	Q_1	Q_2, Q_3, Q_4, Q_5	Q_6
Drivers	Danaher S20660VTS	Danaher S20260VTS	Maxon ADS 50/5
Servomotors	Kollmorgen AKM42G	Kollmorgen AKM31E	Maxon 31007SP
Mass	3.4 kg	1.6 kg	0.24 kg
Inertia	1.5×10^{-4} kg.m^2	0.33×10^{-4} kg.m^2	0.033×10^{-4} kg.m^2
Gear box	LinTech 150836-WC1-1-S129-M04	HD CSF-20-80	HD CSF-08-50
Gear ratio	100 π rad: 1 m	80:1	50:1

The motors and drivers that were selected are listed in Table 2.2. The selection criterion mainly takes the size, precision, and nominal speed into account. A Mini40 force/torque sensor from ATI is attached between the ultrasound probe (only a dummy probe is shown in Figure 2.1 (a)) and the tool flange of the robot. Although it is small (a radius of 0.02 m and a height of 0.014 m), it can measure forces up to 60 N and torques up to 1 Nm. This is sufficient in ultrasound scan application, since the estimated force is typically below 10 N and the torques are less than 1 Nm (Salcudean et al., 1999a).

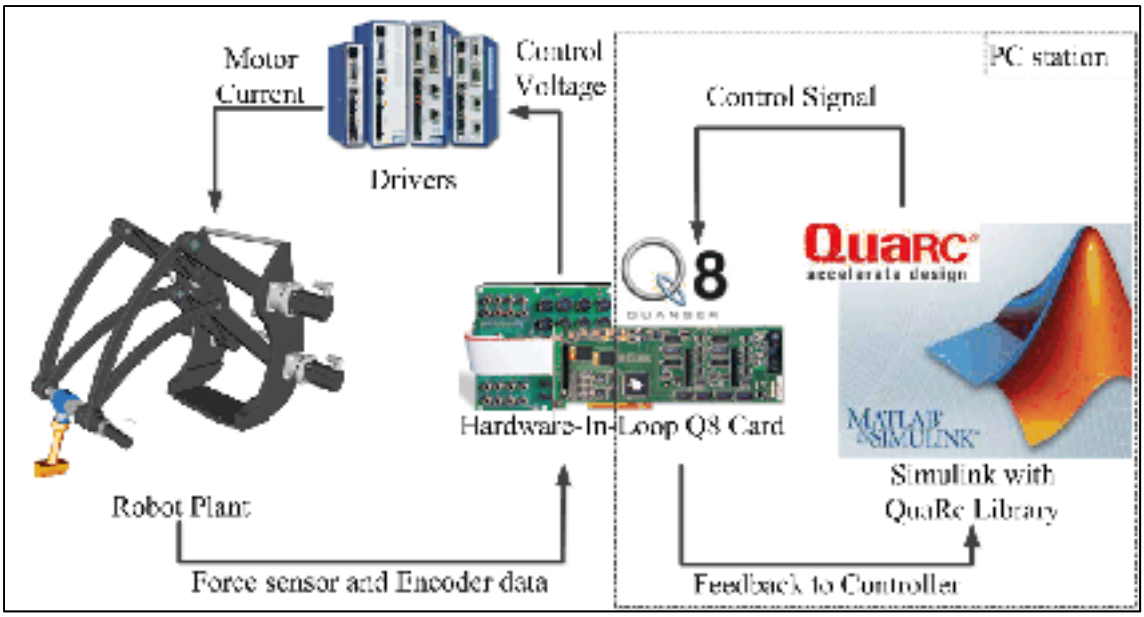

Figure 2.2 Setup of MedRUE

Figure 2.2 shows the setup of the robot system. A Q8 I/O card from Quanser provides eight A/D ports, eight D/A ports, eight encoder inputs, and thirty two digital I/O ports. Six A/D ports are used for reading the force/torque sensor data, and six encoder inputs are used for position data. On a personal computer (PC) station, these sensor data can be read and serve as feedback for the robot controller using the Quanser library QuaRC in Simulink. A real-time thread is created by QuaRC to run the program code generated by Simulink. While MedRUE is moving, the user can start/stop the program or modify/observe the controller's parameters in Simulink. The Q8 card sends the control command from six D/A ports to drivers to generate torques for motors on the robot.

2.3 Direct kinematic model

A geometric approach based on MedRUE's four components is used to find its direct kinematic model. First, a kinematic model of a general five-bar mechanism is analyzed, and its results are then adapted to MedRUE's kinematic model.

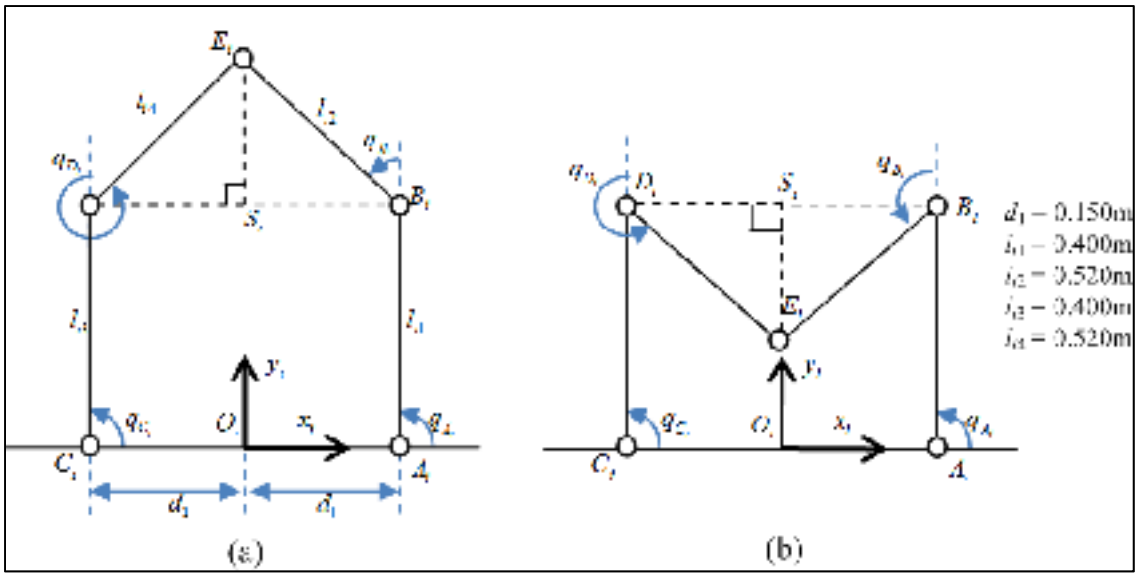

Figure 2.3 General five-bar mechanism: (a) positive assembly mode; (b) negative assembly mode

Figure 2.3 shows a general five-bar mechanism in the x_iy_i plane of the frame O_i (i = 1, 2 throughout this paper to indicate the number of five-bar mechanism) in two assembly modes. The link A_iC_i with length $2d_1$ is fixed with the x_i axis of frame O_i, while other four links can rotate with axes located at their geometric ends. Lengths of four movable links are denoted as l_{ij} where j = 1 to 4. Variables q_{Ai} and q_{Ci} are the values of the actuated revolute joints, while q_{Bi} and q_{Di} are passive revolute joints values. E_i is considered as the end point of this mechanism.

The vectors from the origin point O_i to A_i and C_i are represented as

$$\mathbf{r}_{O_iA_i} = \begin{bmatrix} x_{O_iA_i} & y_{O_iA_i} & z_{O_iA_i} \end{bmatrix}^T = \begin{bmatrix} d_1 & 0 & 0 \end{bmatrix}^T \tag{2.1}$$

$$\mathbf{r}_{O_iC_i} = \begin{bmatrix} x_{O_iC_i} & y_{O_iC_i} & z_{O_iC_i} \end{bmatrix}^T = \begin{bmatrix} -d_1 & 0 & 0 \end{bmatrix}^T \tag{2.2}$$

Thus the vectors from the origin point O_i to B_i and D_i are obtained as

$$\mathbf{r}_{O_iB_i}\left(q_{A_i}\right)=\begin{bmatrix} x_{O_iA_i}+l_{i1}\cos q_{A_i} \\ y_{O_iA_i}+l_{i1}\sin q_{A_i} \\ 0 \end{bmatrix} \tag{2.3}$$

$$\mathbf{r}_{O_iD_i}\left(q_{C_i}\right)=\begin{bmatrix} x_{O_iC_i}+l_{i3}\cos q_{C_i} \\ y_{O_iC_i}+l_{i3}\sin q_{C_i} \\ 0 \end{bmatrix} \tag{2.4}$$

As shown in Figure 2.3, S_i is defined as the projection of E_i on the vector $\mathbf{r}_{DiBi} = \mathbf{r}_{OiBi} - \mathbf{r}_{OiDi}$. If $\left\|\mathbf{r}_{D_iB_i}\right\|=\sqrt{\mathbf{r}_{D_iB_i}^T\mathbf{r}_{D_iB_i}} > l_{i4}+l_{i2}$, there will be no solution, since the distance between q_{Bi} and q_{Di} exceeds the sum of the link lengths. Otherwise, applying the Pythagorean theorem on the two right triangles $D_iS_iE_i$ and $B_iS_iE_i$, we have:

$$\left.\begin{aligned} \left\|\mathbf{r}_{S_iE_i}\right\|^2+\left\|\mathbf{r}_{D_iS_i}\right\|^2 &= l_{i4}^2 \\ \left\|\mathbf{r}_{S_iE_i}\right\|^2+\left(\left\|\mathbf{r}_{D_iB_i}\right\|-\left\|\mathbf{r}_{D_iS_i}\right\|\right)^2 &= l_{i2}^2 \end{aligned}\right\} \tag{2.5}$$

Equation (2.5) gives the solution:

$$\left.\begin{aligned} \mathbf{r}_{D_iS_i}\left(q_{A_i},q_{C_i}\right) &= \frac{l_{i4}^2-l_{i2}^2+\left\|\mathbf{r}_{D_iB_i}\right\|^2}{2\left\|\mathbf{r}_{D_iB_i}\right\|}\frac{\mathbf{r}_{D_iB_i}}{\left\|\mathbf{r}_{D_iB_i}\right\|} \\ \mathbf{r}_{S_iE_i}\left(q_{A_i},q_{C_i}\right) &= \sqrt{l_{i4}^2-\left\|\mathbf{r}_{D_iS_i}\right\|^2}\begin{bmatrix} 0 & -1 & 0 \\ 1 & 0 & 0 \\ 0 & 0 & 0 \end{bmatrix}\frac{\mathbf{r}_{D_iB_i}}{\left\|\mathbf{r}_{D_iB_i}\right\|} \end{aligned}\right\} \tag{2.6}$$

The solution for the end point E_i is

$$\mathbf{r}_{O_iE_i}\left(q_{A_i},q_{C_i}\right)=\mathbf{r}_{O_iD_i}+\mathbf{r}_{D_iS_i}\pm\mathbf{r}_{S_iE_i} \tag{2.7}$$

This sign in front of vector $\mathbf{r}_{SiEi}$ is positive if the mechanism is in positive assembly mode, as indicated in Figure 2.3(a), and negative when in negative assembly mode, as shown in Figure 2.3(b). The five-bar mechanism in MedRUE is the first case. Then, the angle values of the passive joints are

$$q_{B_i}\left(q_{A_i}\right)=\text{atan2}\left(y_{O_iE_i}-y_{O_iB_i},x_{O_iE_i}-x_{O_iB_i}\right)-q_{A_i} \tag{2.8}$$

$$q_{D_i}\left(q_{C_i}\right)=\text{atan2}\left(y_{O_iE_i}-y_{O_iD_i},x_{O_iE_i}-x_{O_iD_i}\right)-q_{C_i} \tag{2.9}$$

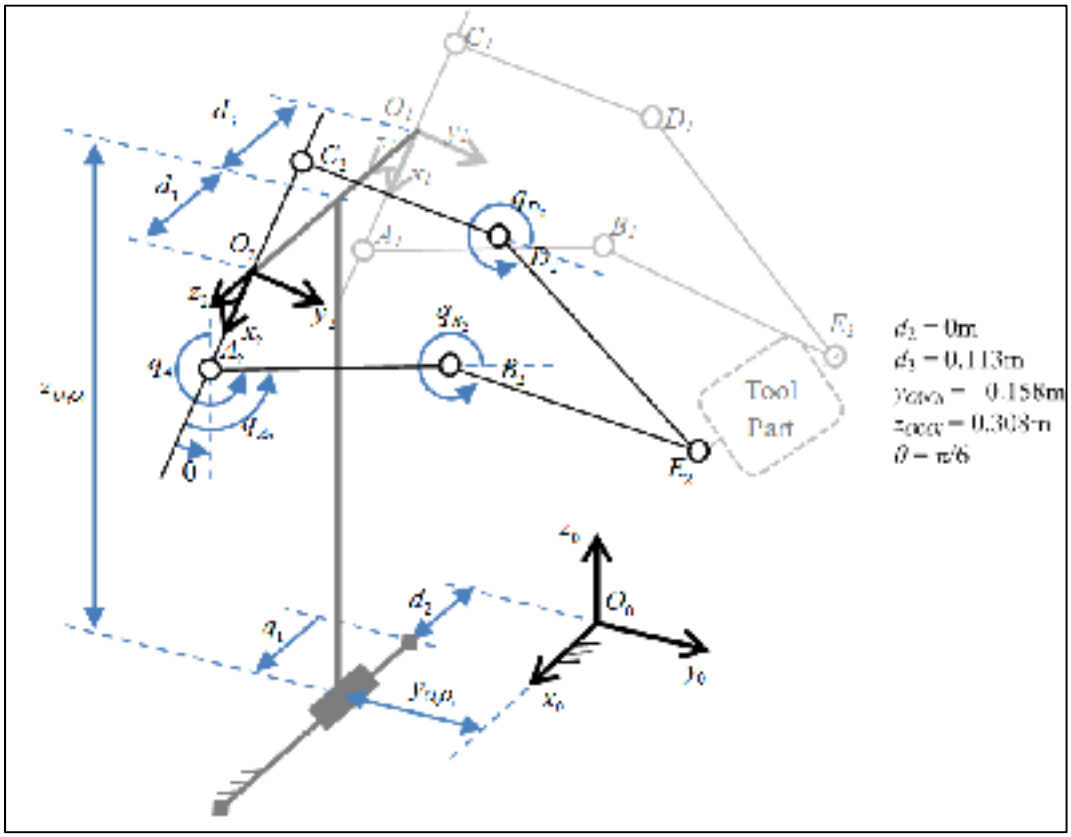

Figure 2.4 MedRUE architecture

If the i^{th} five-bar mechanism in Figure 2.4 is rotated around the z_i axis at a constant angle of $-(\theta+\pi/2)$, and then duplicated onto the mobile base, the architecture of MedRUE in Figure 2.1 (b) can be redrawn as in Figure 2.4. It is notable that both q_{Bi} and q_{Di} in Figure 2.4 are always greater than π rad, for providing space for patients under the robot arms. The two five-bar planes are parallel and perpendicular to the x_0 axis of the base frame O_0. Referring to the definition of q_4 in Figure 2.4, four actuated revolute joint values are defined as

$$q_4=\pi-\theta+q_{A_2},\ q_5=\pi-\theta+q_{C_2},\ q_2=\pi-\theta+q_{A_1},\ q_3=\pi-\theta+q_{C_1} \tag{2.10}$$

The homogeneous transformation matrix of the frames O_i w.r.t. the base frame O_0 is

$$
\begin{aligned}
{}^{0}\mathbf{T}_i(q_1) &= \mathbf{D}_x\left(x_{O_0O_i}\right)\mathbf{D}_y\left(y_{O_0O_i}\right)\mathbf{D}_z\left(z_{O_0O_i}\right)\mathbf{R}_y\left(\frac{\pi}{2}\right)\mathbf{R}_z(-\theta) \\
&= \begin{bmatrix} 0 & 0 & 1 & x_{O_0O_i} \\ -\sin(\theta) & \cos(\theta) & 0 & y_{O_0O_i} \\ -\cos(\theta) & -\sin(\theta) & 0 & z_{O_0O_i} \\ 0 & 0 & 0 & 1 \end{bmatrix}
\end{aligned} \tag{2.11}
$$

where $x_{O0Oi}(q_1) = d_2 + q_1 + (-1)^i d_3$, θ is a constant value in the mechanical design of MedRUE in Figure 2.4.

The coordinates of E_i can be represented in the base frame by parameters defined in Eq. (2.10), combined with the five-bar model Eq. (2.7) and transformation Eq. (2.11):

$$\mathbf{r}_{O_0E_1}(q_1, q_2, q_3) = {}^{0}\mathbf{T}_1(q_1)\,\mathbf{r}_{O_1E_1}\left(q_{A_1}, q_{C_1}\right) \tag{2.12}$$

$$\mathbf{r}_{O_0E_2}(q_1, q_4, q_5) = {}^{0}\mathbf{T}_2(q_1)\,\mathbf{r}_{O_2E_2}\left(q_{A_2}, q_{C_2}\right) \tag{2.13}$$

As shown in Figure 2.5(a), the coordinates of the universal joint centers are

$$\mathbf{r}_{O_0F_1}(q_1, q_2, q_3) = \mathbf{r}_{O_0E_1} + \begin{bmatrix} d_4 & 0 & 0 \end{bmatrix}^T \tag{2.14}$$

$$\mathbf{r}_{O_0F_2}(q_1, q_4, q_5) = \mathbf{r}_{O_0E_2} - \begin{bmatrix} d_4 & 0 & 0 \end{bmatrix}^T \tag{2.15}$$

The dashed box in Figure 2.5(b) demonstrates the physical revolution sequence of the tool part: rotation along the temporal axes *x'* and *y'*, and *z'*. Owing to the mechanical design of the tool part, *x'* always aligns with x_0, and *z'* aligns with z_P. As defined in Figure 2.5(b), when $\alpha = \beta = \gamma = 0$, then *x'*, *y'* and *z'* are parallel to the corresponding axes of the base frame.

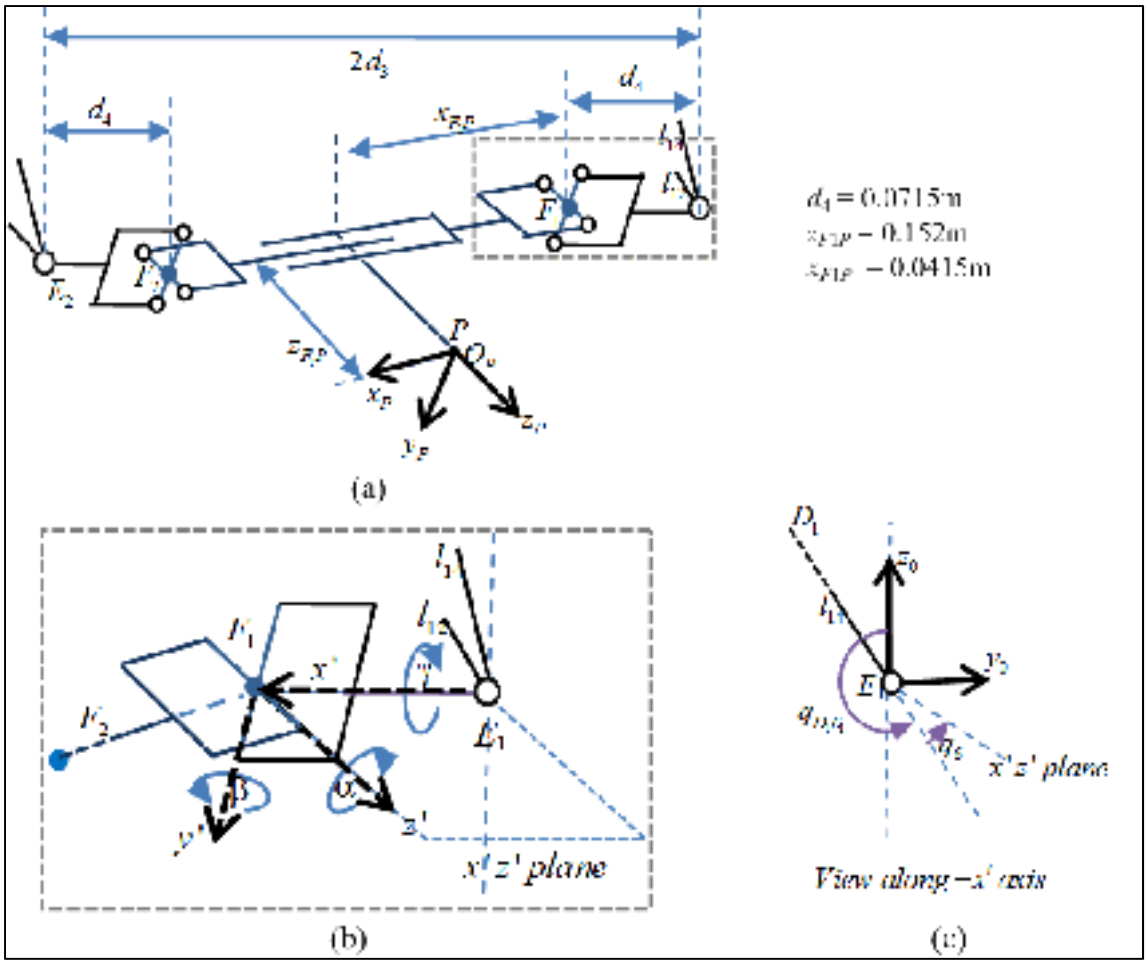

Figure 2.5 Architecture of the MedRUE tool part: (a) overall structure; (b) microscopic view of the dashed block in (a); (c) view on (b) from right to left

Confirming the revolution sequence of the tool part, Euler-XYZ angles (Craig, 2004) are chosen to express the orientation of the probe frame O_P w.r.t. the base frame O_0. In this context, γ is the sum of the rotations along x' as in Figure 2.5(c), and can be obtained by

$$\gamma(q_2, q_3, q_6) = q_{D_1E_1} + q_6 \tag{2.16}$$

where $q_{D_1E_1} = q_3 + q_{D_1}$.

Actuator Q_6 is fixed on l_{14} between D_1 and E_1, and so q_6 is defined as the angle starting from l_{14} to the $x'z'$ plane. Since the probe will always point down to the skin surface during the scan process, γ is restrained in the open interval (π/2, 3π/2).

The unit vector from F_1 to F_2 is parallel to x_P axis of the frame O_P, yielding

$$\mathbf{u}_{F_1F_2} = \mathbf{R}_x(\gamma)\mathbf{R}_y(\beta)\mathbf{R}_z(\alpha)\begin{bmatrix}1 & 0 & 0\end{bmatrix}^T = \begin{bmatrix}\cos\beta\cos\alpha \\ \sin\gamma\sin\beta\cos\alpha + \cos\gamma\sin\alpha \\ -\cos\gamma\sin\beta\cos\alpha + \sin\gamma\sin\alpha\end{bmatrix} \tag{2.17}$$

Equation (2.17) can also be represented by variables defined in Eq. (2.14) and Eq. (2.15):

$$\mathbf{u}_{F_1F_2}(q_2, q_3, q_4, q_5) = \frac{\mathbf{r}_{O_0F_2} - \mathbf{r}_{O_0F_1}}{\left\|\mathbf{r}_{O_0F_2} - \mathbf{r}_{O_0F_1}\right\|} = \begin{bmatrix}u_x \\ u_y \\ u_z\end{bmatrix} \tag{2.18}$$

If it were assumed that $|\alpha|$, $|\beta|$ can reach $\pi/2$, then the projection of F_1 and F_2 on x_0 axis would be equal in Figure 2.5. This is impossible, because F_1 and F_2 are rigidly attached to the two parallel five-bar mechanisms, and the distance along between F_1 and F_2 along x_0 axis is a constant:

$$u_x\left\|\mathbf{r}_{O_0F_2} - \mathbf{r}_{O_0F_1}\right\| = x_{O_0F_2} - x_{O_0F_1} = 2(d_3 - d_4) \tag{2.19}$$

Thus, the inequalities $|\alpha| < \pi/2$ and $|\beta| < \pi/2$ must stand, and $\cos\alpha \neq 0$ in Eq. (2.17). In the design of MedRUE, the mechanical limit of a universal joint is $|\alpha| \leqslant \pi/6$, $|\beta| \leqslant \pi/6$. Then, α and β can be computed by Eq. (2.17) and Eq. (2.18):

$$\alpha(q_2, q_3, q_4, q_5) = \sin^{-1}(u_y\cos\gamma + u_z\sin\gamma) \tag{2.20}$$

$$\beta(q_2, q_3, q_4, q_5) = \sin^{-1}\left(\frac{u_y\sin\gamma - u_z\cos\gamma}{\cos\alpha}\right) \tag{2.21}$$

The coordinates of the probe tip P can be represented by

$$\mathbf{r}_{O_0P}(q_1, q_2, q_3, q_4, q_5, q_6) = \mathbf{r}_{O_0F_1} + {}^0\mathbf{R}_P\mathbf{r}_{F_1P} \tag{2.22}$$

where $\mathbf{r}_{F_1P} = \begin{bmatrix}x_{F_1P}, 0, z_{F_1P}\end{bmatrix}^T$ is a constant vector in Figure 2.5(a), ${}^0\mathbf{R}_P(q_2, q_3, q_4, q_5, q_6) = \mathbf{R}_x(\gamma)\mathbf{R}_y(\beta)\mathbf{R}_z(\alpha)$. Thus, the homogeneous transformation matrix of O_P w.r.t. O_0 is ${}^0\mathbf{T}_P(q_1, q_2, q_3, q_4, q_5, q_6) = \begin{bmatrix}{}^0\mathbf{R}_P & \mathbf{r}_{O_0P} \\ \mathbf{0} & 1\end{bmatrix}$.

2.4 Inverse kinematic model

The inverse kinematic model will be solved based on the MedRUE components, in the same way that the direct kinematic model was solved in the previous section. In this case, the coordinates of E_i are computed based on the features of the tool part, and then be transformed into the local frames O_i of five-bar mechanisms. Finally, all the joint values are obtained by solving the inverse kinematic model for a five-bar mechanism.

Given the pose [x_{O0P}, y_{O0P}, z_{O0P}, α, β, γ] of the probe frame O_P, the coordinates of F_1 can be obtained by inverting Eq. (2.22):

$$\mathbf{r}_{O_0F_1}\left(x_{O_0P}, y_{O_0P}, z_{O_0P}, \alpha, \beta, \gamma\right) = \mathbf{r}_{O_0P}\left(x_{O_0P}, y_{O_0P}, z_{O_0P}\right) - \mathbf{R}_x(\gamma)\mathbf{R}_y(\beta)\mathbf{R}_z(\alpha)\mathbf{r}_{F_1P} \tag{2.23}$$

To obtain the coordinates of F_2, Eq. (2.18) can be rewritten as

$$\mathbf{r}_{O_0F_2} = \left\|\mathbf{r}_{O_0F_2} - \mathbf{r}_{O_0F_1}\right\|\mathbf{u}_{F_1F_2} + \mathbf{r}_{O_0F_1} \tag{2.24}$$

where $\mathbf{u}_{F1F2}$ can be calculated from Eq. (2.17). By combining Eq. (2.17) and Eq. (2.19), the distance between F_1 and F_2 can be represented as

$$\left\|\mathbf{r}_{O_0F_2} - \mathbf{r}_{O_0F_1}\right\| = \frac{2\left(d_3 - d_4\right)}{\cos\beta\cos\alpha} \tag{2.25}$$

Adding the offsets according to Eq. (2.14) and Eq. (2.15), the end points of the two five-bar mechanisms are

$$\mathbf{r}_{O_0E_i} = \mathbf{r}_{O_0F_i} + (-1)^i \begin{bmatrix} d_4 & 0 & 0 \end{bmatrix}^T, \quad \text{for } i = 1, 2 \tag{2.26}$$

From Eq. (2.11), the translation joint value is

$$q_1 = x_{O_0O_1} + d_3 - d_2 \tag{2.27}$$

Since the five-bar mechanism is located in the plane perpendicular to the x_0 axis of frame O_0, Eq. (2.27) can be rewritten as

$$q_1 = x_{O_0E_1} + d_3 - d_2 \tag{2.28}$$

With the constant transformation matrix ${}^0\mathbf{T}_i(\theta)$ that we introduced in Eq. (2.11), the coordinates of the end points of the five-bar mechanisms can be represented in their local

frame O_i, as in Eq. (2.29). In this way, the rest of the inverse geometric model of the robot is transformed into an inverse geometric model for a five-bar mechanism:

$$\mathbf{r}_{O_iE_i} = {}^{0}\mathbf{T}_i^{-1}(q_1)\mathbf{r}_{O_0E_i}, \text{ for } i=1,2 \tag{2.29}$$

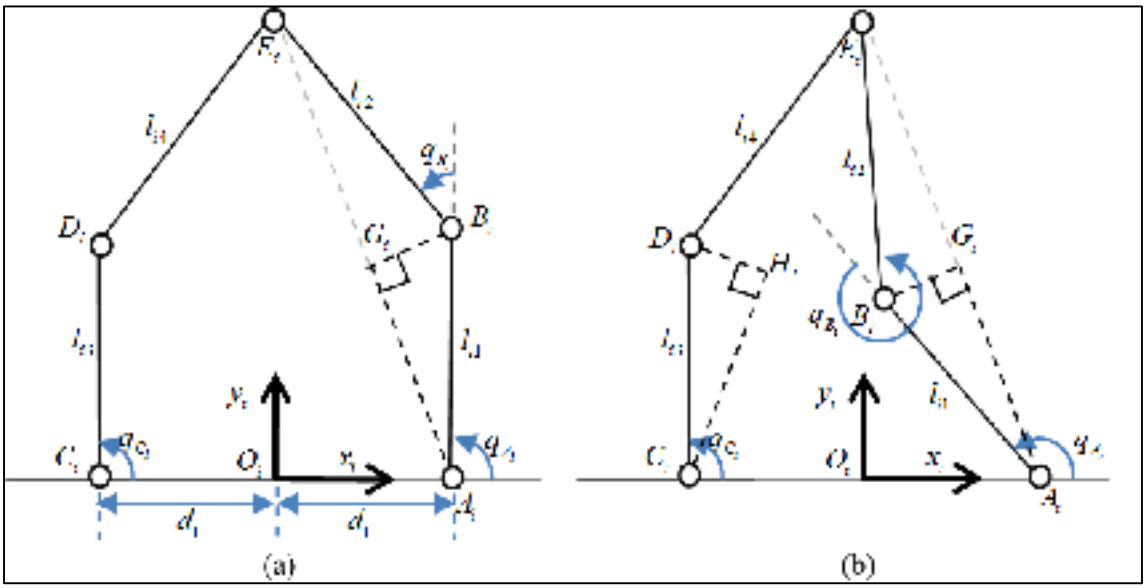

Figure 2.6 Two solutions for the inverse kinematic model of a five-bar mechanism

There will be no solution for q_{Ai}, if $\left\|\mathbf{r}_{A_iE_i}\right\| > l_{i1}+l_{i2}$, where $\mathbf{r}_{AiEi} = \mathbf{r}_{OiAi} - \mathbf{r}_{OiEi}$. As shown in Figure 2.6, G_i is defined as the projection of B_i on the vector $\mathbf{r}_{AiEi} = \mathbf{r}_{OiEi} - \mathbf{r}_{OiAi}$ and H_i is defined as the projection of D_i on the vector $\mathbf{r}_{CiEi} = \mathbf{r}_{OiEi} - \mathbf{r}_{OiCi}$. Applying the same method used in Eq. (2.5) on both left and right half sides of the five-bar mechanism,

$$\left.\begin{aligned}
\mathbf{r}_{A_iG_i} &= \frac{l_{i1}^2 - l_{i2}^2 + \left\|\mathbf{r}_{A_iE_i}\right\|^2}{2\left\|\mathbf{r}_{A_iE_i}\right\|}\frac{\mathbf{r}_{A_iE_i}}{\left\|\mathbf{r}_{A_iE_i}\right\|} \\
\mathbf{r}_{G_iB_i} &= \sqrt{l_{i1}^2 - \left\|\mathbf{r}_{A_iG_i}\right\|^2}\begin{bmatrix} 0 & -1 & 0 \\ 1 & 0 & 0 \\ 0 & 0 & 0 \end{bmatrix}\frac{\mathbf{r}_{A_iE_i}}{\left\|\mathbf{r}_{A_iE_i}\right\|}
\end{aligned}\right\} \tag{2.30}$$

$$\left.\begin{aligned}\mathbf{r}_{C_iH_i} &= \frac{l_{i3}^2 - l_{i4}^2 + \left\|\mathbf{r}_{C_iE_i}\right\|^2}{2\left\|\mathbf{r}_{C_iE_i}\right\|}\frac{\mathbf{r}_{C_iE_i}}{\left\|\mathbf{r}_{C_iE_i}\right\|} \\ \mathbf{r}_{H_iD_i} &= \sqrt{l_{i3}^2 - \left\|\mathbf{r}_{C_iH_i}\right\|^2}\begin{bmatrix}0 & -1 & 0\\ 1 & 0 & 0\\ 0 & 0 & 0\end{bmatrix}\frac{\mathbf{r}_{C_iE_i}}{\left\|\mathbf{r}_{C_iE_i}\right\|}\end{aligned}\right\} \tag{2.31}$$

Confirming the MedRUE configuration, the vector $\mathbf{r}_{OiBi}$ can be obtained by

$$\mathbf{r}_{O_iB_i} = \mathbf{r}_{O_iA_i} + \mathbf{r}_{A_iG_i} \pm \mathbf{r}_{G_iB_i} \tag{2.32}$$

$$\mathbf{r}_{O_iD_i} = \mathbf{r}_{O_iC_i} + \mathbf{r}_{C_iH_i} \pm \mathbf{r}_{H_iD_i} \tag{2.33}$$

The signs in Eq. (2.32) and Eq. (2.33) demonstrate two different solutions of the configurations of a unit, given the pose of the end points of the five-bar mechanism. The sign is negative when the configuration is as in Figure 2.6(a), and positive when it is as shown in Figure 2.6(b). MedRUE always works in the latter case for both five-bar mechanisms. Knowing the coordinates of B_i and D_i, the active joint values can be obtained by

$$q_{A_i} = \operatorname{atan2}\left(y_{O_iB_i} - y_{O_iA_i}, x_{O_iB_i} - x_{O_iA_i}\right) \tag{2.34}$$

$$q_{C_i} = \operatorname{atan2}\left(y_{O_iD_i} - y_{O_iC_i}, x_{O_iD_i} - x_{O_iC_i}\right) \tag{2.35}$$

Finally, by submitting the results q_{Ai} and q_{Ci} to Eq. (2.10), we obtain the joint values q_2, q_3, q_4 and q_5. The translation joint q_1 is obtained in Eq. (2.28), and the last joint value can be deduced from Eq. (2.9) and Eq. (2.16),

$$q_6 = \gamma - q_3 - q_{D_1} \tag{2.36}$$

2.5 Singularity issues and workspace

Singularities only exist in the two five-bar mechanisms of MedRUE. For each mechanism, there are two types of singularity. A Type I singularity occurs when any side of the five-bar mechanism fully extends in Figure 2.7(a) or overlaps in Figure 2.7(b). A Type II singularity occurs when two adjacent bars around the end point overlap in Figure 2.7(c) or are aligned in

Figure 2.7(d). Because of the physical joint limits for q_{Ai} and q_{Ci}, only the singularity in Figure 2.7(a) is achievable in reality. A safety mechanism will freeze the motors when the robot approaches the singularity region.

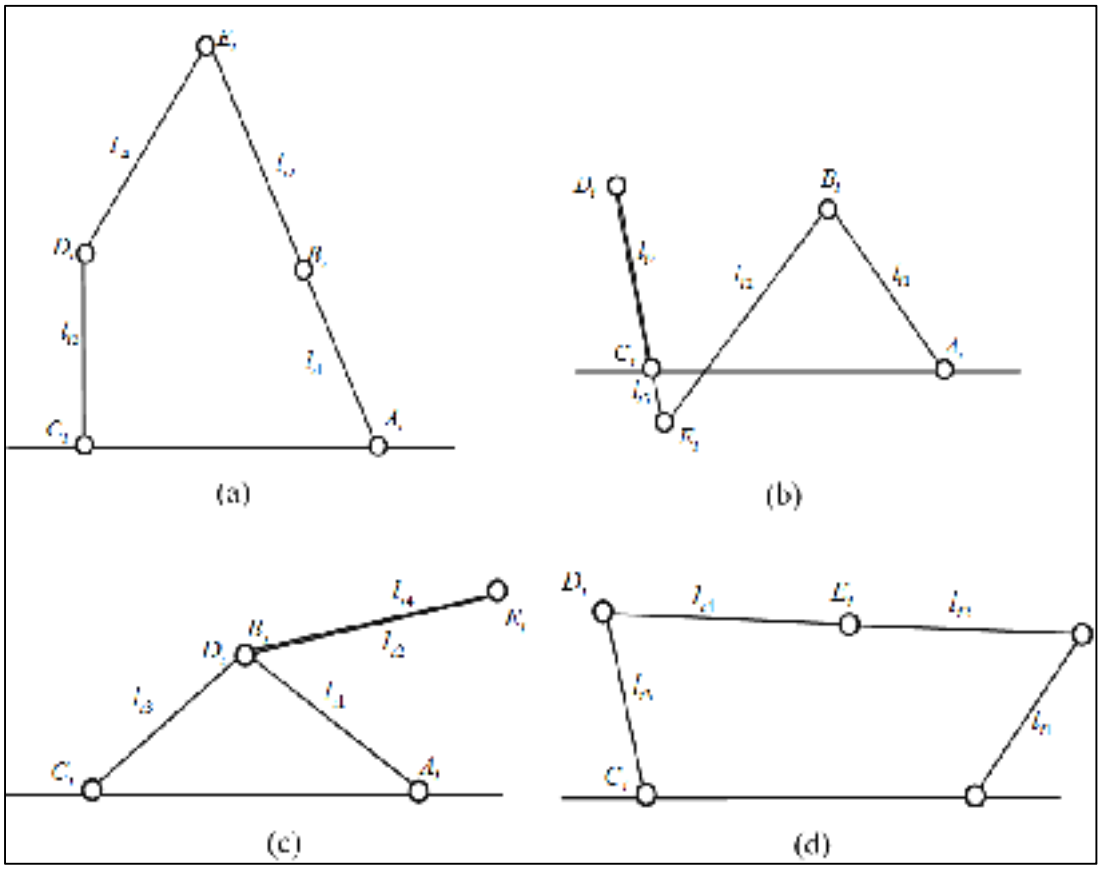

Figure 2.7 Singularities in the five-bar mechanism

A simulation is done to demonstrate the workspace of MedRUE. Since linear motion of q_1 dominates the motion along x direction of base frame, the workspace of MedRUE can be obtained by extending its workspace in y_0z_0 plane along x_0 axis. The position of probe in y_0z_0 plane is mainly determined by the symmetrically assembled two five-bar mechanisms, thus, the analysis of the workspace of one five-bar mechanism will lead to the workspace of MedRUE.

In Figure 2.8, we take 22 samples for q_2 and 17 samples for q_3 throughout their joint limits respectively ($q_{Ai} \in [130^o, 235^o]$, $q_{Ci} \in [120^o, 210^o]$). After eliminating the counterpart solution as in Figure 2.6(a), 298 positions of E_i are presented in small red circle in Figure 2.8. The outline of E_i positions are constituted by five curves, either due to joint limits or singularity case when $q_{Bi} = 2\pi$.

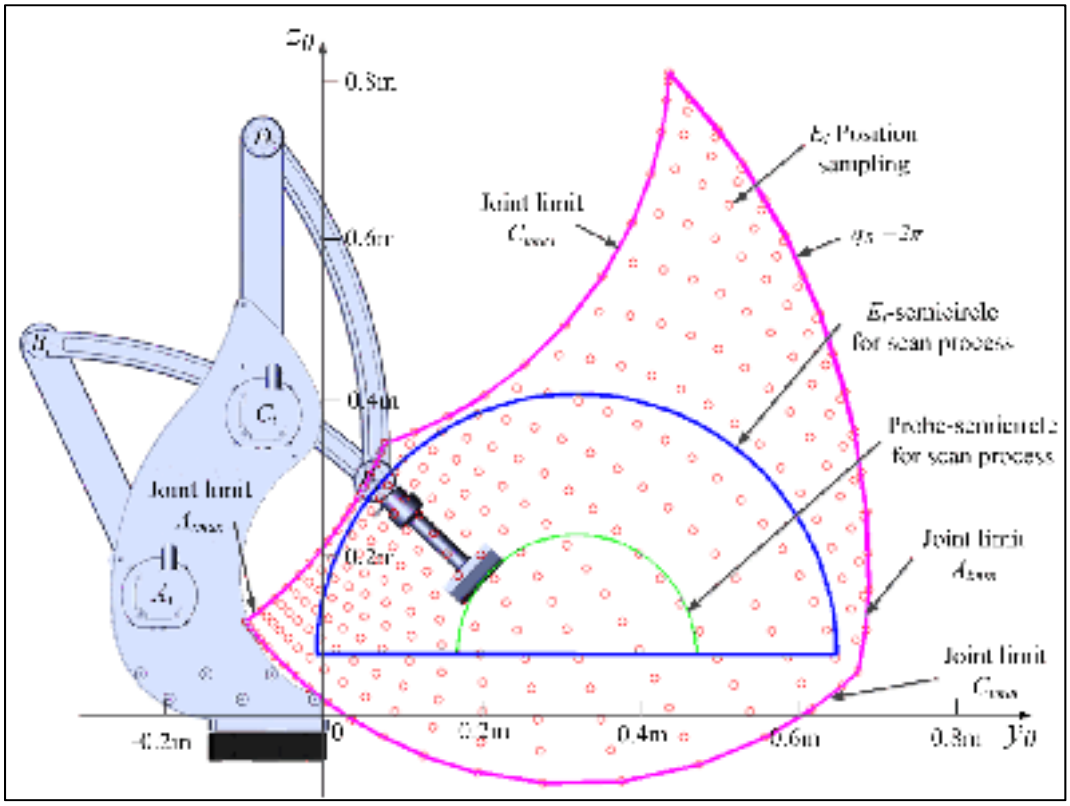

Figure 2.8 Workspace analysis of MedRUE

During the ultrasound scan process, the trajectory of probe will follow curves on the surface of the patient legs. For simplification purposes, it can be approximated as a semicircle. In Figure 2.8, the outer blue curve (E_i-semicircle) is the maximum radius of semicircle the point E_i can reach in its workspace. With an offset of the probe length, the inner green one (probe-semicircle) demonstrates the maximum radius of semicircle for the probe when probe is pointing to the normal of the surface.

The physical orientation limit of MedRUE probe is [0° 360°) along x_0 axis and [-30° 30°] along y_0/z_0 axes. In the scan process, only (0° 180°) is needed for rotation along $x_0$axis. Because of the offset of the probe length and the outer boundary E_i-semicircle in Figure 2.8, only the points inside the probe-semicircle can meet the orientation requirements for ultrasound scan process. The points outside probe-semicircle have difficulties to point to the circle center without violating the E_i-semicircle constrains. Rotations along y_0/z_0 axis skew the probe tip off the y_0z_0 plane and it reduces the scan workspace along x_0 axis. To allow the robot to performance the orientation of y_0/z_0 axes, a distance of $z_{F1P}\sin(\pi/6)$ must be reserved for the linear guide on each side of its limit. In summary, the workspace during ultrasound scan is an extension of probe-semicircle along x_0 axis. Under the specification of Table 2.1, it is a semi-cylinder shaped volume with 0.734 meter in length and 0.3 meter in diameter, (0° 180°) along x_0 axis and [-30° 30°] along y_0/z_0 axes orientation.

2.6 Conclusion

A new medical robot, MedRUE, is presented in this paper. It has the ability to diagnose PAD in the large, complex and twisted arterial system of the lower limbs. An intuitive solution for its direct and inverse kinematic model is discussed. Using this method, a complex serial-parallel robot system is decomposed into several simplified sub-mechanisms. This system will be proposed to relieve sonographers of their daily physical load of carrying an ultrasound imaging equipment. The robot will not only help in the diagnosis of PAD automatically, but also provide reliable data for 3D reconstruction in future research.

CHAPTER 3

METROLOGICAL EVALUATION OF A NOVEL MEDICAL ROBOT AND ITS KINEMATIC CALIBRATION

Longfei Zhao, Ahmed Joubair, Ilian A. Bonev and Pascal Bigras
Department of Automated Manufacturing Engineering, École de technologie supérieure,
1100 Rue Notre-Dame Ouest, Montréal, Québec H3C 1K3

This paper has been accepted on May 16th, 2015 as an article in
International Journal of Advanced Robotic Systems

Abstract

The vessels are twisted in a longitudinal 3D space in the lower limbs of human. Thus, it is difficult to perform an ultrasound scanning examination automatically in this area. In this paper, a new medical parallel robot is introduced to effectively diagnose the vessel disease in the lower limbs. Also, the robot's position repeatability and accuracy are evaluated. Furthermore, the robot's accuracy is improved through a calibration process in which the kinematic parameters are identified through a simple identification approach.

Keywords: medical robot; parallel robot, kinematic calibration, laser tracker.

3.1 Introduction

Ultrasound (US) scanning examination is one of the major diagnostic modality in daily medicine. It shows advantages in low cost and non-radiation to the human body. However, a survey reveals that the repetitive strain of daily US examination over many hours causes

musculoskeletal disorders to sonographers (Evans, Roll and Baker, 2009). Thus, many works are engaged to design medical robots to perform the US scanning examination. Furthermore, the US medical robot can collect the position data during the examination process, which provides the essential information for 3D reconstruction of the scanned area.

Several works on US medical robots have been performed. A portable US medical robot was proposed in a tele-scanning robot project (Gourdon et al., 1999). It has 4 degrees of freedom (DOF) and assists a doctor in controlling a US probe remotely. The robot prototype is extended to 6 DOF in the OTELO project (Delgorge et al., 2005). It is agile and able to cover the large scan area. Nevertheless, the US scanning examination requires an assistant to hold the robot during the examination process. In general, the portable medical US robot does not reduce the workload of sonographers. Many US medical robot systems are developed based on industrial robots. The Hippocrate system employs a PA-10 robot arm from Mitsubishi Heavy Industry to scan the carotid artery (Pierrot et al., 1999). An F3 industrial robot from CRS Robotics was used in (Nelson et al., 2012) to diagnose breast cancer. A lightweight robot LWR from KUKA was used in (Conti, Park and Khatib, 2014) to assist the sonographer. However, the industrial robots are mostly designed for general use, and medical applications are limited due to the closed architecture of the controllers. Thus, some serial robots are designed for US medical implement, such as an abdominal US scanning robot in (Koizumi et al., 2008), and a self-balanced robot from the University of British Columbia (Abolmasesumi et al., 2002; Salcudean et al., 1999b). Serial robots, however, have relatively low stiffness and their position errors are accumulated and amplified from link to link. Besides, the motors are generally mounted on links successively. Thus, each link has to support the weight of all the subsequent links and actuators. Several medical US robots were designed with parallel structures. A parallel robot was developed to hold the US probe in (Onogi et al., 2013). It consists of three legs displaced on both sides of the patient and a probe gripper hanged over the scanned area. A cable robot was developed in the TER project (Vilchis et al., 2003). A sliding mechanism was used in a parallel robot to perform echographic diagnosis (Masuda et al., 2001a; Masuda et al., 2001b). The patient has to support the weight of the robot since the mechanism is placed on the scanning area. WTA-2R was

designed to hold the US probe and perform an automated scanning based on US image feedback in (Nakadate et al., 2010).

The medical robots mentioned above are mainly designed for carotid or abdominal US scanning, and are not appropriate for the examination in the lower limbs due to their limited workspace, dexterity, etc. MedRUE (for **M**edical **R**obot for vascular **U**ltrasound **E**xamination) is a new parallel robot designed to perform US scanning examination in lower limbs, improved based on its first concept proposed in (Lessard, Bigras and Bonev, 2007). It has a longitudinal workspace aligned with the patient's leg, but relatively small size and low weight (Zhao et al., 2013). Since MedRUE needs to know the position of its end-effector with high accuracy, in order to reconstruct a 3D volume from US images, it needs to be calibrated.

The calibration of an US medical robot involves probe calibration and kinematic calibration. The probe calibration identifies the constant transformation between the probe body and US image (Lindseth et al., 2003; Mercier et al., 2005). However, in this article, we focus only on the kinematic calibration of the robot. The kinematic calibration methods for serial robots are mostly on identifying the Denavit-Hartenberg parameters (Lee, 2013; Mooring, Driels and Roth, 1991). These parameters are widely used to develop the kinematic model of serial robots. However, they are not always the simplest way to model parallel robots. The calibration methods of parallel robots vary depending on the different geometric structures of parallel robots. There are many calibration studies regarding planar robots, the Gough-Stewart platform and the Delta robot (Joubair and Bonev, 2013; Joubair, Slamani and Bonev, 2012a; Li et al., 2014; Maurine and Dombre, 1996).

In this paper, we present a new medical robot with its repeatability and accuracy assessment. The position accuracy is improved by a calibration method based on direct position measurements with a laser tracker. The method is easy to implement on the robot without elaborate knowledge of the advanced kinematic calibration. In addition, the proposed calibration method identifies kinematic parameters individually, and the nonlinear interferences

between kinematic parameters are significantly reduced. Therefore, the identified kinematic parameters are more accurate, and they are important for further research, such as temporal stiffness calibration. By contrast, other calibration methods using optimization identify all kinematic parameters simultaneously (Barati, Khoogar and Nasirian, 2011; Joubair et al., 2015; Renders et al., 1991). The optimization approach may achieve better end-effector position accuracy, but it sacrifices the precisions for individual parameters. The MedRUE robot is briefly described in section 2 and its kinematic model and calibrated parameters are presented as well. The section 3 discusses the assessment of repeatability and accuracy. Then the proposed calibration method and the result are demonstrated in section 4. At the end, a conclusion is addressed in section 5.

3.2 Robot description and kinematic

In this section, the new medical robot is introduced and its intuitive kinematic model is discussed. The kinematic model considers the errors of link lengths and offsets which need to be calibrated, and thereafter the calibrated parameters are listed. The robot base reference frame ($\mathcal{F}_0$) and the world reference frame ($\mathcal{F}_W$) are also defined in this section. The parameters to describe these two frames are identified with a laser tracker.

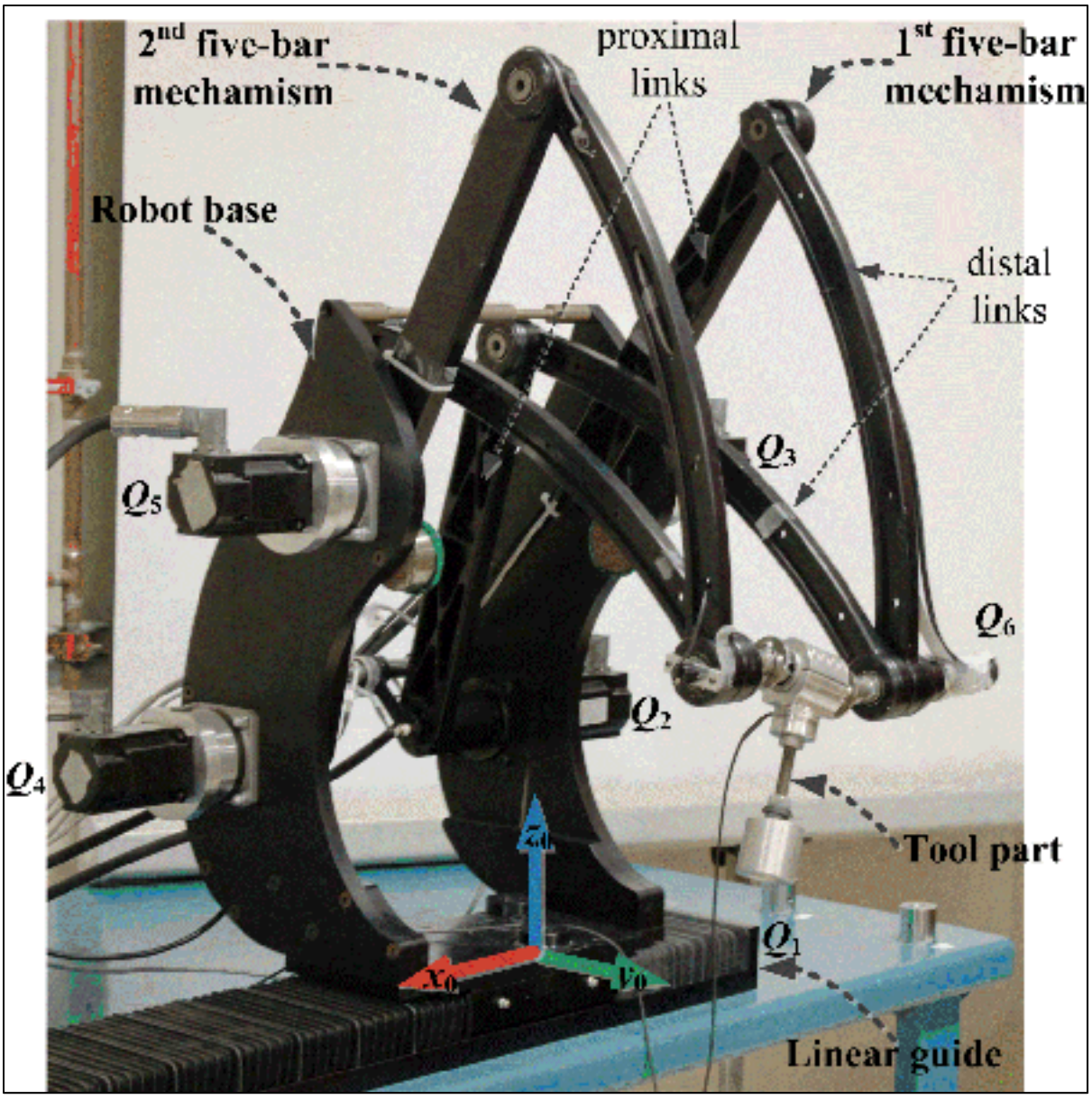

Figure 3.1 MedRUE : a new prototype of medical US robot

3.2.1 Introduction of MedRUE

MedRUE (Medical Robot for vascular Ultrasound Examination) is a prototype of medical parallel robot designed for the diagnosis of the peripheral arterial disease in the lower limbs.

As shown in Figure 3.1, MedRUE is a 6-DOF parallel robot consisting of a robot base with a linear guide, two five-bar mechanisms and the *tool part* to carry the US probe. The U-shaped robot base is mounted on a linear guide (driven by actuator Q_1). The two five-bar mechanisms are assembled symmetrically on the robot's base, and they are driven by actuators Q_2, Q_3, Q_4 and Q_5. Considering the first five-bar mechanism as an example, the two links driven by actuators are called *proximal links*, and the two links farther from the robot base are called *distal links*. The distal links connect at the shaft of the tool part. The tool part consists of a force/torque sensor and a dummy probe at the end. It is driven to rotate along the shaft by a small actuator Q_6 mounted on a distal link.

Since most actuators of MedRUE are located on the robot's base, the links of the five-bar mechanisms do not need to bear the heavy load of motors. Thus, the robot is relatively light-weight and agile. The linear guide extends the workspace along the length of the patient's leg and the curved distal links avoid mechanical interferences between the robot arms and the patient leg during the examination.

Frame $\mathcal{F}_0$, also referred to as the robot frame, is defined on the robot base plate. The top surface of the robot base plate is defined as the x_0y_0 plane, and its normal is the z_0 axis. The linear guide determines the direction of the x_0 axis, and then the front side of the robot is the direction of y_0 axis. The origin of $\mathcal{F}_0$ is located in the front center hole of the bottom plate.

3.2.2 Kinematic model of MedRUE

The kinematic model of MedRUE and its kinematic parameters are illustrated in Figure 3.2. The two five-bar mechanisms are symmetrically assembled on the robot's base, and can therefore be modelled in the same way. As shown in Figure 3.2(a), the links of the i^{th} five-bar mechanism are named L_{ij}, where $i = 1, 2$ and $j = 0, \ldots, 4$. The corresponding link lengths are denoted by l_{ij}. Link L_{i0} is fixed on the robot's base with an angle θ_i offset. Four actuators Q_{2i} and Q_{2i+1} are mounted on the robot's base, and the corresponding active joint variables are q_{2i} and q_{2i+1} at A_i and C_i respectively. The other joints q_{Bi}, q_{Di} and q_{DEi} are passive. The two five-

bar mechanisms are parallel to the y_0z_0 plane. In Figure 3.2(b), the tool part connects the two five-bar mechanisms at E_i (with an offset d_{ei}). Two universal joints are located at F_i (with an offset d_{fi}) to provide orientation of the probe-support. The synchronized motion (i.e. same speed and direction) of two five-bar mechanisms provide translation motions to the tool part, while the unsynchronized motion provides rotation motions. During the rotational motion, the distance variation between the two universal joints F_i is compensated by a passive translation joint located between the probe-support and F_2. Actuator Q_6 is attached on L_{14} to provide a rotation motion of the tool part along x_0. The probe-support is considered as the wrist of MedRUE, and a reference frame $\mathcal{F}_w$ is located at its geometric center. Axis x_w is collinear with vector $\overrightarrow{F_1F_2}$ and z_w is pointing to the probe tip.

Given the joint values (q_1,…, q_6), the forward kinematic solution of MedRUE can be obtained as follows:

For the i^{th} (i = 1,2) five-bar mechanism, the coordinates of A_i and C_i are represented as:

$$\mathbf{a}_i = \begin{bmatrix} x_{O_i} & y_{O_i} - \frac{l_{i0}}{2}\sin\theta_i & z_{O_i} + \frac{l_{i0}}{2}\cos\theta_i \end{bmatrix}, \tag{3.1}$$

$$\mathbf{c}_i = \begin{bmatrix} x_{O_i} & y_{O_i} + \frac{l_{i0}}{2}\sin\theta_i & z_{O_i} - \frac{l_{i0}}{2}\cos\theta_i \end{bmatrix}^T, \tag{3.2}$$

where O_i is the midpoint of L_{i0} with

$$x_{O_i} = (-1)^i d_{ei} + q_1 + \tilde{q}_1, \tag{3.3}$$

and $\tilde{q}_k$ is the offset error of k^{th} active joint. Then the coordinates of B_i and D_i are

$$\mathbf{b}_i = \mathbf{a}_i + l_{i1}\Psi(q_{2i} + \tilde{q}_{2i}), \tag{3.4}$$

$$\mathbf{d}_i = \mathbf{c}_i + l_{i3}\Psi(q_{2i+1} + \tilde{q}_{2i+1}), \tag{3.5}$$

where $\Psi(\varphi) = \begin{bmatrix} 0 & -\sin(\varphi) & \cos(\varphi) \end{bmatrix}^T$.

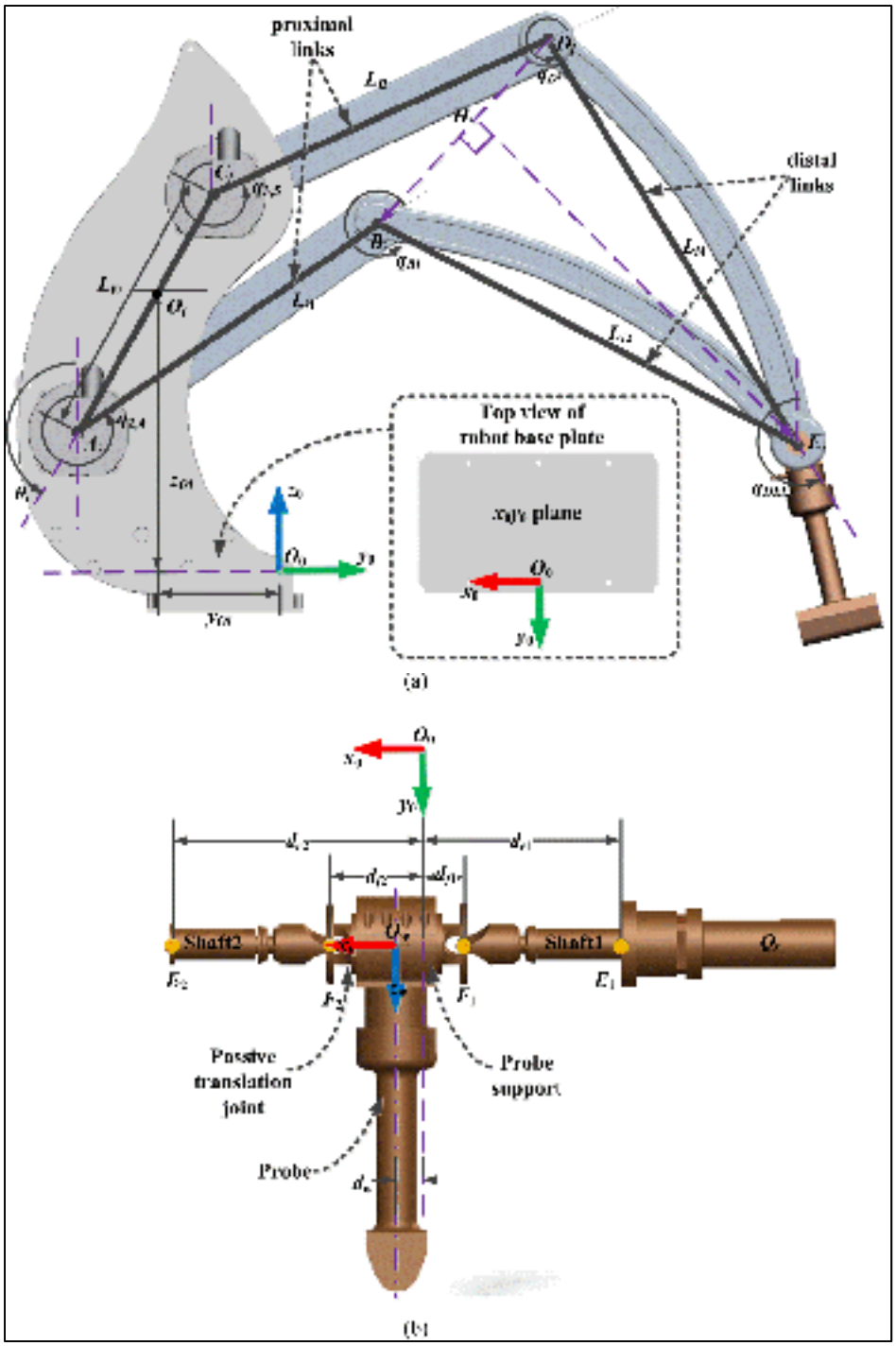

Figure 3.2 Kinematic model and parameters of MedRUE: (a) five-bar mechanism and robot base; (b) the tool part

With the coordinates of B_i and D_i, all side lengths of the triangle $B_iD_iE_i$ are known. Then the coordinates of E_i are obtained as

$$\mathbf{e}_i = \mathbf{d}_i + \overrightarrow{D_iH_i} + \overrightarrow{H_iE_i}, \tag{3.6}$$

where

$$\overrightarrow{D_iH_i} = \frac{l_{i4}^2 - l_{i2}^2 + \left\|\overrightarrow{D_iB_i}\right\|^2}{2\left\|\overrightarrow{D_iB_i}\right\|}\mathbf{u}_{\overrightarrow{D_iB_i}}, \tag{3.7}$$

$$\overrightarrow{H_iE_i} = \sqrt{l_{i4}^2 - \left\|\overrightarrow{D_iH_i}\right\|^2}\begin{bmatrix} 0 & -1 & 0 \\ 1 & 0 & 0 \\ 0 & 0 & 0 \end{bmatrix}\mathbf{u}_{\overrightarrow{D_iB_i}}, \tag{3.8}$$

and **u** represents a unit vector. As shown in Figure 3.2(a), F_i has an offset $(-1)^i(d_{fi} - d_{ei})$ w.r.t. E_i along x_0. Thus the coordinates of F_i are

$$\mathbf{f}_i = \mathbf{D}\left((-1)^i\left(d_{fi} - d_{ei}\right), 0, 0\right)\mathbf{e}_i \tag{3.9}$$

where $\mathbf{D}(x, y, z)$ is the translation operation.

Assuming the orientation of the wrist reference frame $\mathcal{F}_w$ is represented in the XYZ Euler angles, then

$$\mathbf{R}(\gamma, \beta, \alpha)\begin{bmatrix} 1 \\ 0 \\ 0 \end{bmatrix} = \mathbf{u}_{\overrightarrow{F_1F_2}} = \begin{bmatrix} u_x \\ u_y \\ u_z \end{bmatrix} \tag{3.10}$$

where $\mathbf{R}(\gamma, \beta, \alpha)$ is the rotation matrix. Since actuator Q_6 is fixed on L_{14}, the first Euler angle is obtained as

$$\gamma = q_{D_1E_1} + q_6 + \tilde{q}_6 \tag{3.11}$$

where $q_{DE_1} = \text{atan2}\left(-\left(y_{E_1} - y_{D_1}\right), z_{E_1} - z_{D_1}\right)$. The other two Euler angles are obtained by substituting Eq. (3.11) into Eq. (3.10):

$$\alpha = \sin^{-1}\left(u_y \cos\gamma + u_z \sin\gamma\right), \tag{3.12}$$

$$\beta = \sin^{-1}\left(\frac{u_y \sin\gamma - u_z \cos\gamma}{\cos\alpha}\right). \tag{3.13}$$

Thus, the coordinates of O_w (the origin of wrist reference frame $\mathcal{F}_w$) w.r.t. $\mathcal{F}_0$ are

$$\mathbf{p}_w = \mathbf{f}_1 + \mathbf{R}(\gamma, \beta, \alpha)\begin{bmatrix} d_{f1} + d_w & 0 & 0 \end{bmatrix}^T. \tag{3.14}$$

In our calibration process, a Spherically Mounted Retroreflector (SMR) is attached to the probe. The coordinates of the SMR center w.r.t. $\mathcal{F}_w$ are x_S, y_S and z_S. Thus, the coordinates of SMR w.r.t. $\mathcal{F}_0$ are

$$\mathbf{p}_S = \mathbf{p}_w + \mathbf{R}(\gamma, \beta, \alpha)\begin{bmatrix} x_S & y_S & z_S \end{bmatrix}^T. \tag{3.15}$$

Assuming the transformation matrix from the world reference frame $\mathcal{F}_W$ to $\mathcal{F}_0$ is represented by six parameters x_W, y_W, z_W, γ_W, β_W and α_W. Then $\mathbf{p}_S$ is represented w.r.t. $\mathcal{F}_W$ as:

$${}^W\mathbf{p}_S = {}^0_W\mathbf{T}^{-1}\mathbf{p}_S \tag{3.16}$$

where ${}^0_W\mathbf{T} = \mathbf{D}(x_W, y_W, z_W)\,\mathbf{R}(\gamma_W, \beta_W, \alpha_W)$.

3.3 Repeatability and accuracy assessment

In this section, the robot repeatability and accuracy are assessed before calibration. Our assessment method is an adaptation of the International Standard on robot performance and test method (ISO-9283, 1998). The nominal kinematic model (i.e., the model before calibration) is assessed in this section, and the calibrated kinematic model is validated in section 4.

In the nominal kinematic model (Zhao et al., 2013), the corresponding parameters of the two five-bar mechanisms in Figure 3.2 are identical (*e.g.*, $l_{1j} = l_{2j}$, $j = 0, \ldots, 4$). Moreover, each five-bar mechanism is symmetrically designed. In other words, the proximal links are identical ($l_{i1} = l_{i3}$, $i = 1, 2$), and so are the distal links ($l_{i2} = l_{i4}$, $i = 1, 2$). Also, the offset joint values are considered to be equal to zero.

3.3.1 Robot path design and measurement points

In our implementation, the position accuracy has the priority since it is required both for safety reasons and 3D reconstruction. Orientation errors can be compensated in the 3D

reconstruction with well-developed techniques, such as scale-invariant feature transform. In this article, only the position repeatability and accuracy are studied, while the orientation is kept constant during the measurement procedure. Before taking measurements, it is necessary to define the robot trajectory and the measured positions during the data acquisition.

Knowing that the robot is dedicated to lower limb scans, the effective robot's workspace is considered to be a half-cylinder, which covers the top surface area of a patient's leg. As shown in Figure 3.3(a), nine measurement points P_i (i = 1, …, 9) are considered in this target workspace. Namely, eight corners C_j (j = 1, …, 8) are created on both sides of the target workspace and form two planes $C_1C_2C_7C_8$ as well as $C_3C_4C_5C_6$. Point P_1 is located at the barycenter of all eight corners. Point P_2 is defined on the vector $\overrightarrow{P_1C_1}$, with $\left\|\overrightarrow{P_1P_2}\right\| = 0.8\left\|\overrightarrow{P_1C_1}\right\|$, points P_3 to P_9 are similarly defined.

The used measurement path is an extension of the path design proposed in (Joubair, Slamani and Bonev, 2012b). The robot end-effector is initially located at P_1, and trajectory of the robot end-effector is demonstrated in Figure 3.3(b). When the process started, the robot end-effector is following the trajectory on the plane $C_3C_4C_5C_6$, which is composed of the sequence $P_9 \rightarrow P_1 \rightarrow P_8 \rightarrow P_1 \rightarrow P_7 \rightarrow P_1 \rightarrow P_6 \rightarrow P_1$. Then, the robot trajectory continues on the plane $C_1C_2C_7C_8$, and it follows the sequence $P_5 \rightarrow P_1 \rightarrow P_4 \rightarrow P_1 \rightarrow P_3 \rightarrow P_1 \rightarrow P_2 \rightarrow P_1$ to finish a measurement cycle. In our experiment, 30 measurement cycles are taken.

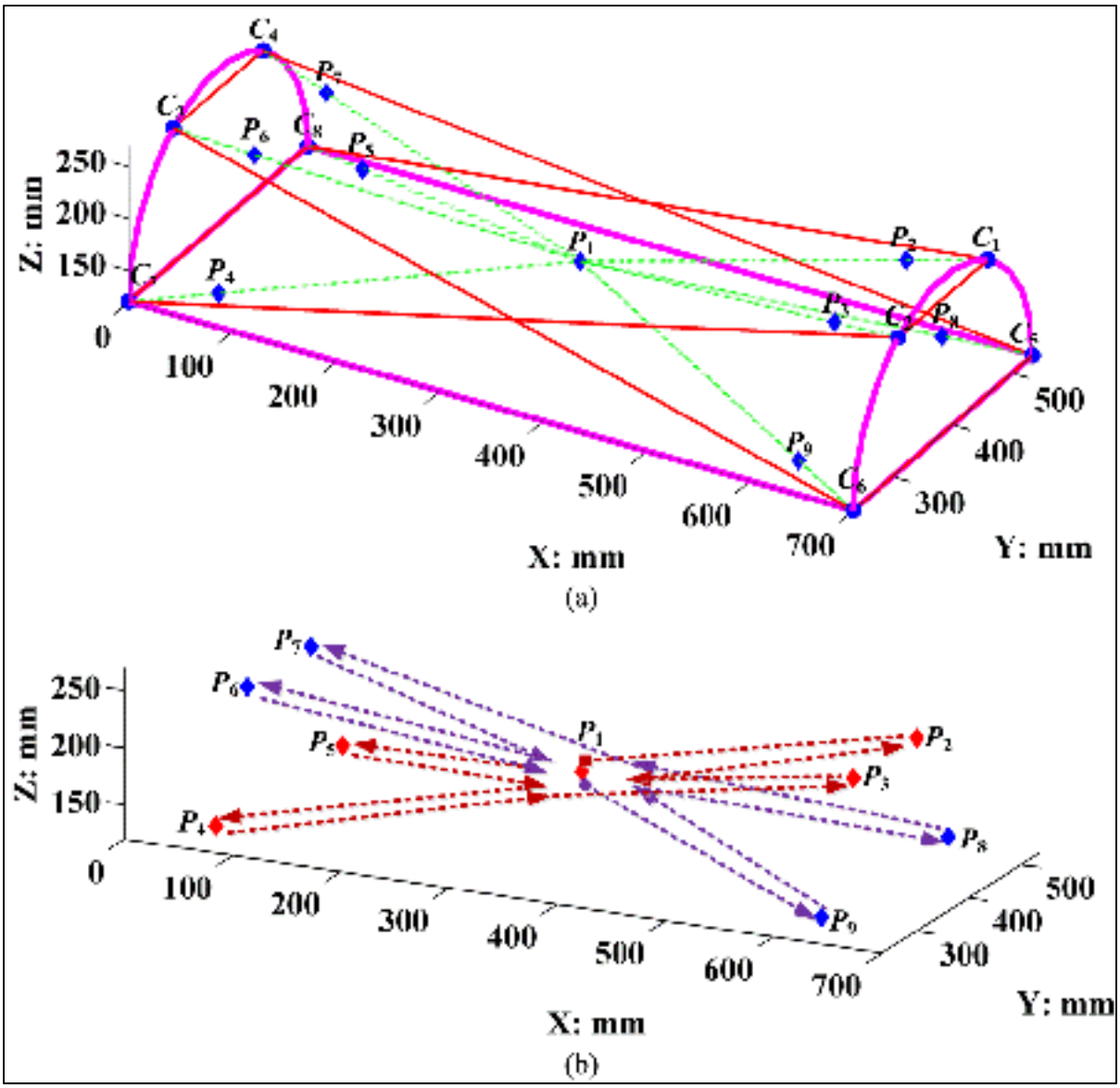

Figure 3.3 The measurement points in the workspace of MedRUE:
(a) measurement points definition, (b) measurement path.

In this method, P_1 is visited from eight different directions, while all other measurement points are visited in a unidirectional approach (direction from P_1). Thus, the experiment design is used to estimate multidirectional repeatability at position P_1 and unidirectional repeatability at positions P_2 to P_8.

3.3.2 Accuracy and repeatability definition

At each measurement point P_i (i = 1, …, 9), the position of the end-effector is measured n times, where n = 8 directions × 30 cycles = 240 at P_1, and n = 30 at each of the other eight measurement points. A set of n measurements on a measurement point P_i is called a *cluster* of P_i. For any cluster, the *barycenter* is defined as a virtual point whose coordinates $[\bar{x}_i \quad \bar{y}_i \quad \bar{z}_i]$ are the mean values of all the n measurements:

$$\bar{x}_i = \frac{1}{n}\sum_{\eta=1}^{n} x_{i\eta}, \tag{3.17}$$

$$\bar{y}_i = \frac{1}{n}\sum_{\eta=1}^{n} y_{i\eta}, \tag{3.18}$$

$$\bar{z}_i = \frac{1}{n}\sum_{\eta=1}^{n} z_{i\eta}, \tag{3.19}$$

The distance between the η^{th} cycle measurement at P_i and the barycenter of the cluster of P_i is

$$l_{i\eta} = \sqrt{\left(x_{i\eta} - \bar{x}_i\right)^2 + \left(y_{i\eta} - \bar{y}_i\right)^2 + \left(z_{i\eta} - \bar{z}_i\right)^2}. \tag{3.20}$$

Then the repeatability at P_i is defined as follows (ISO-9283, 1998):

$$RP_{P_i} = \bar{l}_i + 3S_{li}, \tag{3.21}$$

where $\bar{l}_i = \frac{1}{n}\sum_{\eta=1}^{n} l_{i\eta}$ and $S_{li} = \sqrt{\frac{\sum_{\eta=1}^{n}\left(l_{i\eta} - \bar{l}_i\right)^2}{n-1}}$.

The absolute position accuracy of P_i is defined by (ISO-9283, 1998):

$$APA_i = \sqrt{\left(\bar{x}_i - \hat{x}_i\right)^2 + \left(\bar{y}_i - \hat{y}_i\right)^2 + \left(\bar{z}_i - \hat{z}_i\right)^2}, \tag{3.22}$$

where $\hat{x}_i, \hat{y}_i$ and $\hat{z}_i$ are the command positions (reference positions) of P_i, and $\bar{x}, \bar{y}$ and $\bar{z}$ are barycenter coordinates defined in Eqs. (3.17) to (3.19).

MeRUE will be used to take US images at prescribed intervals. These US images will then be used to reconstruct the 3D model of the blood vessel. For the purposes of the medical examination, the accuracy in measuring the position of a given US image is important w.r.t. the neighboring images. In other words, the relative accuracy is important for our robot.

A *relative position accuracy* of a point can be defined as the accuracy of the distance between adjacent points (e.g., the distance accuracy between P_1 and P_2). Since each point P_i (i = 2, …, 9) is reached starting from P_1 in Figure 3.3(b), the nominal relative displacement of P_i (i = 2, …, 9) is calculated as follows:

$$\hat{\boldsymbol{\delta}}_i = \hat{\mathbf{p}}_i - \hat{\mathbf{p}}_1,\ i = 2,...,9\,. \tag{3.23}$$

where $\hat{\mathbf{p}}_i$ is the nominal coordinates vector. Then Eq. (3.22) is modified to compute the relative position accuracy as

$$RPA_i = \left\| \boldsymbol{\delta}_i - \hat{\boldsymbol{\delta}}_i \right\|, i = 2,...,9 \tag{3.24}$$

where $\boldsymbol{\delta}_i = \mathbf{p}_i - \mathbf{p}_{1i}$ is the measured relative displacement based on laser tracker. The notation $\mathbf{p}_{1i}$ is the measurement value of P_1 before moving towards to each P_i (i = 2, …, 9).

3.3.3 Experiment setup and results

The measurement setup is shown in Figure 3.4. The measurements are taken with a Faro Laser Tracker ION having a distance accuracy of 8 μm + 0.4 μm/m, and angular accuracy of 10 μm + 2.5 μm/m. The emitted laser is reflected by an SMR, which is magnetically attached to a *nest*. In our experiment, the target measurement is a 1.5 inch SMR mounted on the tool part. The measured positions are expressed w.r.t. the laser reference frame ($\mathcal{F}_L$) and transformed w.r.t. $\mathcal{F}_W$.

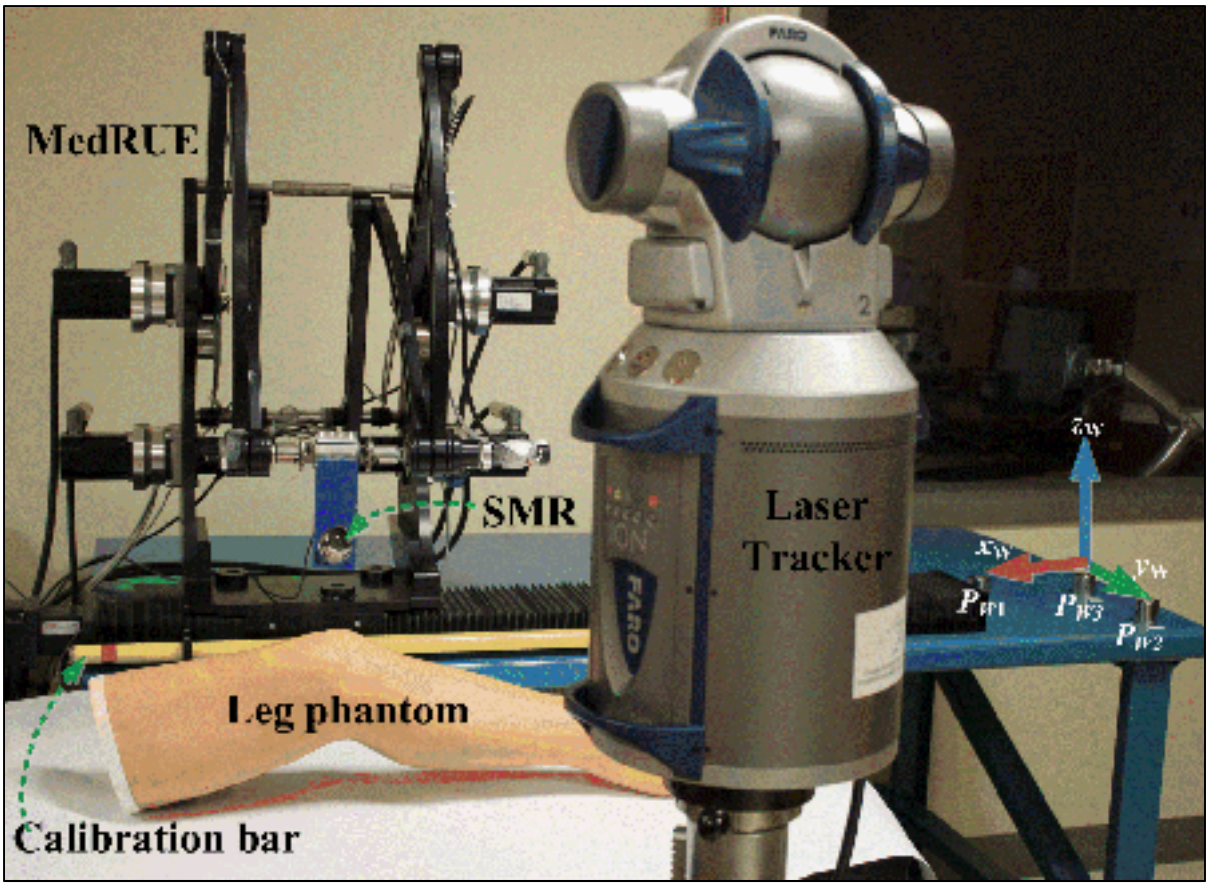

Figure 3.4 Experiment setup of MedRUE positioning performance assessment and calibration

Table 3.1 Position repeatability (in μm)

	P_1	P_2	P_3	P_4	P_5	P_6	P_7	P_8	P_9
RP	143	141	54	60	105	99	84	77	50
RP_x	139	136	43	47	96	88	71	61	38
RP_y	74	43	39	43	48	51	52	49	39
RP_z	54	19	18	21	33	28	24	27	18

We note that the measurement accuracy might be influenced by many aspects such as, environment, duration of operation, as well as the distance between the target and the laser tracker. Therefore, we evaluated the laser tracker accuracy for our own set-up. A calibrated bar with a known length was measured ten times and the distance error was found to be

47μm according to Eq. (3.21). However, the measurement errors were reduced by taking several measurements at each position.

The result for the position repeatability at the nine measurement points are shown in Table 3.1. The first row shows the composed repeatability defined in Eq. (3.21), and the other three rows list the repeatability according to the x, y and z axes. Naturally, the position repeatability at P_1 is worse, which is mainly because the arrivals at P_1 are from eight different directions. Furthermore, the position repeatability along x at P_1 is poorer than along y and z. This is caused by the fact that the motion along the x axis is dominated by the linear guide, which has a backlash of 76 μm according to its manufacturer.

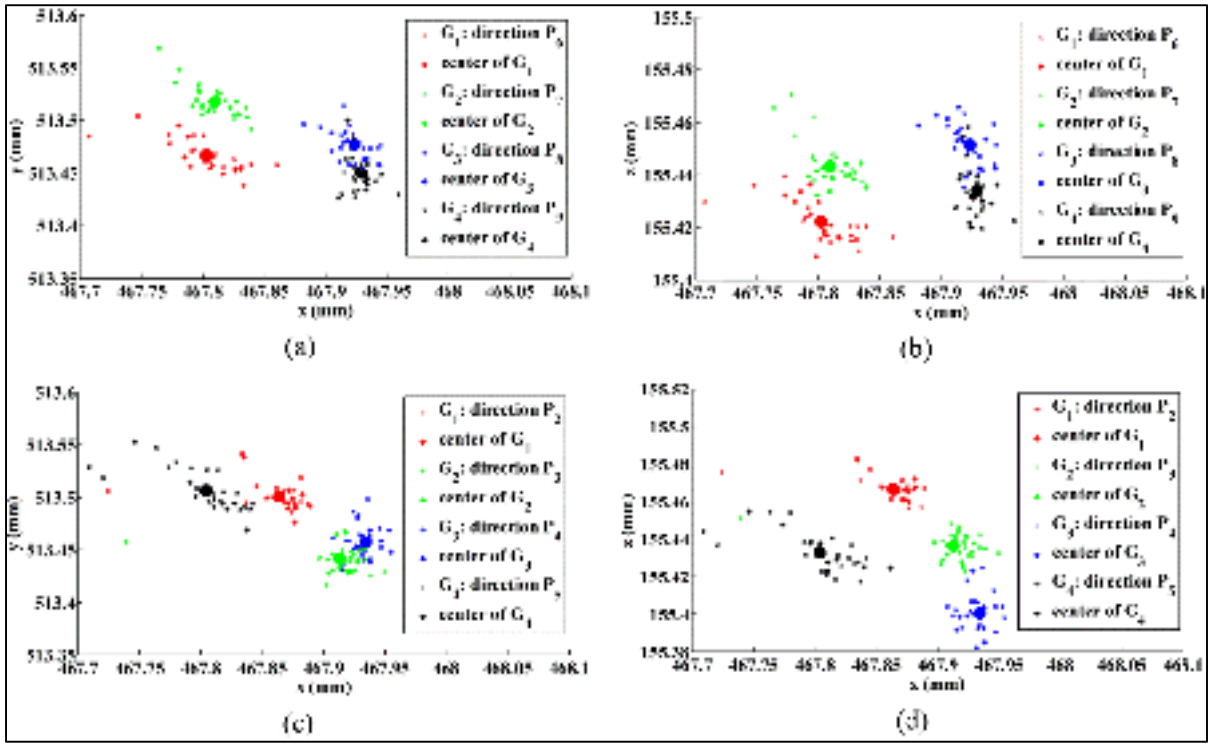

Figure 3.5 Measurements at P_1, for arrivals from multiple directions: (a) on measurement plane $C_3C_4C_5C_6$, view in xy plane; (b) on measurement plane $C_3C_4C_5C_6$, view in xz plane (c) on measurement plane $C_1C_2C_7C_8$; view in xy plane (d) on measurement plane $C_1C_2C_7C_8$, view in xz plane

The results for the repeatability at P_1 in the two measurement planes (i.e. planes $C_1C_2C_7C_8$ and $C_3C_4C_5C_6$) are illustrated in Figure 3.5. On each plane, there are four groups (G_1, G_2, G_3, G_4) of data in different colors indicating four different directions to reach P_1. The measured data are illustrated with an asterisk marker while the barycenter of each group is a solid circle. The cluster groups are clearly separated from each other. The divergence of measurement on P_1 shows the imperfection of the multidirectional movement caused mainly by the backlash of the mechanical parts of our robot.

Table 3.2 Absolute position accuracy (*APA*) and relative position accuracy (*RPA*) before calibration (in mm)

	P_1	P_2	P_3	P_4	P_5	P_6	P_7	P_8	P_9
APA	4.264	1.271	3.849	5.770	0.885	3.788	2.183	2.155	4.792
APA_x	2.217	0.432	1.386	1.823	0.103	1.463	0.568	0.118	2.022
APA_y	1.127	0.129	1.586	2.978	0.677	0.157	1.877	2.124	0.192
APA_z	3.463	1.188	3.222	4.594	0.560	3.491	0.960	0.346	4.340
RPA	—	1.822	1.665	3.018	1.656	2.068	2.058	2.042	1.829
RPA_x	—	0.617	0.886	0.377	0.886	1.074	0.427	0.977	0.569
RPA_y	—	0.340	0.445	2.273	0.460	0.871	0.565	0.896	0.506
RPA_z	—	1.680	1.337	1.950	1.321	1.538	1.932	1.554	1.663

The position absolute accuracy and relative accuracy before calibration is given in Table 3.2. As an early prototype, the robot's poor accuracy is mainly due to its manufacture and assembling errors. The worst case of the absolute accuracy before calibration is about 6 mm. While the worst relative accuracy before calibration is about 3 mm.

3.4 Kinematic calibration experiment

In this section the proposed calibration approach is explained. The actual values of the robot parameters are identified to improve the robot accuracy.

Table 3.3 Kinematic parameters

Group	Description	Parameters
(1)	The world reference frame	x_W, y_W, z_W, γ_W, β_W, α_W
(2)	Active joint offset error	$\tilde{q}_2, \tilde{q}_3, \tilde{q}_4, \tilde{q}_5$
(3)	Assembling of five-bar mechanisms	y_{O1}, z_{O1}, y_{O2}, z_{O2}, θ_1, θ_2
(4)	Link lengths of five-bar mechanisms	l_{10}, l_{11}, l_{12}, l_{13}, l_{14}, l_{20}, l_{21}, l_{22}, l_{23}, l_{24}

The parameters expected to be identified are summarized in four groups, as shown in Table 3.3. Parameters in Group 1 define $\mathcal{F}_W$ which is demonstrated later in Eq. (3.30). Group 2 represents the offset of active joints at the home position. Group 3 is named *assembling parameters*, which specifies how the two five-bar mechanisms are assembled on the robot base, by illustrating the position and angle of link L_{i0} on the robot base (Figure 3.2(a)). Group 4 englobes the lengths of the links of the two five-bar mechanisms.

3.4.1 The world reference frame parameters

The world reference frame $\mathcal{F}_W$ is defined in the robot's workspace by three SMR nests P_{W1}, P_{W2} and P_{W3} as shown in Figure 3.4. Assuming P_{W3} is the origin of $\mathcal{F}_W$ and P_{W1} is a point on the x_W axis, then the three unit vectors of $\mathcal{F}_W$ are defined w.r.t. the $\mathcal{F}_L$. The unit vector $\mathbf{x}_W$ is determined by the normalized vector $\frac{\mathbf{p}_{W_{31}}}{\left\|\mathbf{p}_{W_{31}}\right\|}$, where $\mathbf{p}_{W31}$ is a vector from P_{W3} to P_{W1} in $\mathcal{F}_L$.

The z_W axis of $\mathcal{F}_W$ is defined as the normal of the plane defined by P_{W1}, P_{W2} and P_{W3}. The y_W axis is defined by axes x_W and z_W. The rotation matrix of $\mathcal{F}_W$ w.r.t. $\mathcal{F}_L$ is written as:

$$ {}^{L}_{W}\mathbf{R} = \left[\mathbf{x}_W, \mathbf{y}_W, \mathbf{z}_W\right]. \tag{3.25} $$

The transformation matrix of $\mathcal{F}_W$ w.r.t. $\mathcal{F}_L$ is defined as follows:

$$ {}^{L}_{W}\mathbf{T} = \begin{bmatrix} {}^{L}_{W}\mathbf{R} & \mathbf{o}_W \\ \mathbf{0} & 1 \end{bmatrix}, \tag{3.26} $$

where vector $\mathbf{o}_W$ is the composed by the coordinates of P_{W3} w.r.t. $\mathcal{F}_L$. All measured position data can be represented w.r.t. $\mathcal{F}_W$ by using the transformation matrix ${}^{L}_{W}\mathbf{T}$. A point ${}^{W}\mathbf{P}$ is derived from the laser measured data ${}^{L}\mathbf{P}$ by the following equation:

$$\begin{bmatrix} {}^{W}\mathbf{p} \\ 1 \end{bmatrix} = {}^{L}_{W}\mathbf{T}^{-1} \begin{bmatrix} {}^{L}\mathbf{p} \\ 1 \end{bmatrix} \tag{3.27}$$

For convenience, all the further measured positions, in this paper, are implicitly expressed w.r.t. $\mathcal{F}_W$.

Frame $\mathcal{F}_0$ is defined on the robot base plate, as shown in Figure 3.1. The top surface of the plate is considered as the x_0y_0 plane. By placing the SMR in n positions on the x_0y_0 plane, a reference plane is fitted from the laser tracker measurement data ($3\times n$ matrix $\mathbf{P}_\text{n} = [\mathbf{p}_1, \ldots, \mathbf{p}_\text{n}]$, where vector $\mathbf{p}_\text{n}$ is the n^{th} measurement). The barycenter of $\mathbf{P}_n$ is $\overline{\mathbf{p}} = \frac{1}{n}\sum_{k=1}^{n}\mathbf{p}_k$. For the smallest eigenvalue of $\overline{\mathbf{P}}_n^T\overline{\mathbf{P}}_n$ (where $\overline{\mathbf{P}}_n = [\mathbf{p}_1 - \overline{\mathbf{p}}, \mathbf{p}_2 - \overline{\mathbf{p}}, \cdots, \mathbf{p}_n - \overline{\mathbf{p}}]$), its corresponding eigenvector approximates the normal vector $\mathbf{z}_0$ of the fitted plane x_0y_0. Finally, the x_0y_0 plane is determined by a point $\overline{\mathbf{p}}$ and the normal vector $\mathbf{z}_0$. The x_0 axis is aligned with the direction of the linear guide and it is estimated by measuring an SMR on the robot base, while actuating the linear guide. The method to fit a line from 3D cluster points is similar to the method to estimate the normal vector $\mathbf{z}_0$, except that the vector $\mathbf{x}_0$ is estimated as the eigenvector with largest eigenvalue. Then the rotation matrix of $\mathcal{F}_0$ w.r.t. $\mathcal{F}_W$ is found as:

$${}^{W}_{0}\mathbf{R} = [\mathbf{x}_0, \mathbf{y}_0, \mathbf{z}_0]. \tag{3.28}$$

The origin O_0 of $\mathcal{F}_0$ is located on the robot base plate as shown in Figure 3.2(a). Its coordinates w.r.t. $\mathcal{F}_W$ are obtained by placing an SMR above the robot base plate. The projection of the SMR on x_0y_0 plane provides the coordinates of O_0 as follows:

$$\mathbf{o}_0 = \mathbf{o}_0' - \left((\mathbf{o}_0' - \overline{\mathbf{p}}) \cdot \mathbf{z}_0\right)\mathbf{z}_0, \tag{3.29}$$

where $\mathbf{o}_0'$ is the vector of measured coordinates of the SMR. Then, the transformation matrix of $\mathcal{F}_0$ w.r.t. $\mathcal{F}_W$ is obtained as

$$ {}^{W}_{0}\mathbf{T}(x_W, y_W, z_W, \gamma_W, \beta_W, \alpha_W) = \begin{bmatrix} {}^{W}_{0}\mathbf{R} & \mathbf{o}_0 \\ \mathbf{0} & 1 \end{bmatrix}. \tag{3.30} $$

where x_W, y_W, z_W, γ_W, β_W and α_W are the $\mathcal{F}_W$ parameters to be identified: x_W, y_W, and z_W are the coordinates of $\mathbf{o}_0$, and Euler angles γ_W, β_W, α_W are obtained from the rotation matrix ${}^{W}_{0}\mathbf{R}$.

3.4.2 Active joint offset errors

The objective of this subsection is to evaluate the difference between the nominal and the real joint offsets. Active joints q_2, q_3, q_4 and q_5 are considered. As mentioned earlier, the five-bar mechanisms are symmetrically assembled, and therefore, they are calibrated with the same method. For simplicity, only the calibration of the second five-bar mechanism is demonstrated.

As shown in Figure 3.6, ten nests (N_i, i = 1, …, 10) are attached on the five-bar mechanism for measurement purpose. Four nests (N_i, i = 3, 4, 7, 10) are used in this experiment, and the remaining nests are used to identify other parameters.

Active joint q_4 directly drives the rotation motion of L_{21}. Thus, the joint offset error of q_4 is assessed via the evaluation of the orientation error of link L_{21} (Figure 3.2(a)). The orientation of L_{21} is determined by the coordinates of A_2 and B_2. Similarly, the joint offset error of q_5 is assessed via the orientation of link L_{23}, which is determined by the coordinates of C_2 and D_2. Two experiments are designed to obtain the coordinates of A_2, B_2, C_2 and D_2 at the robot home position. Then, the joint offset errors are evaluated.

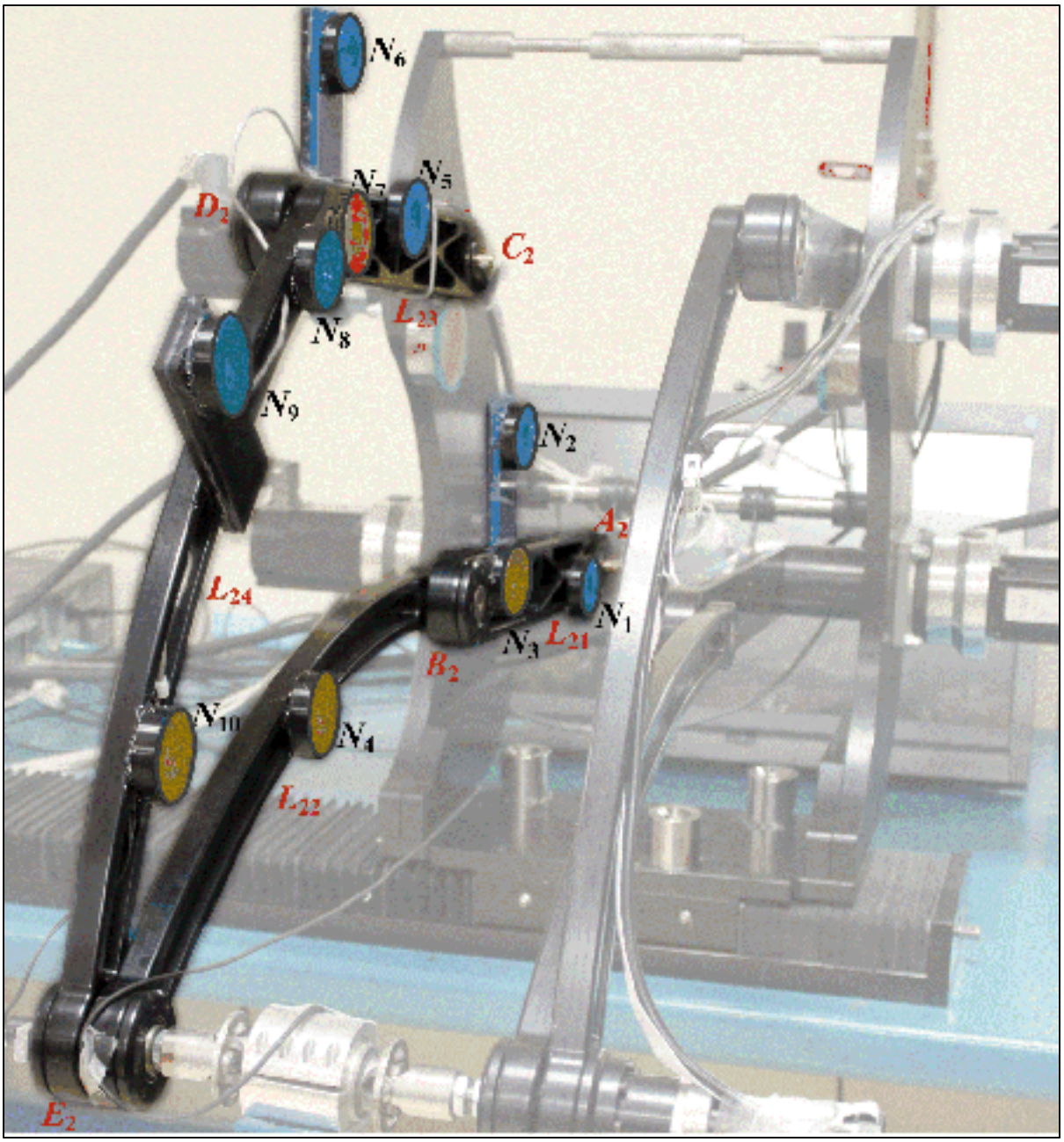

Figure 3.6 Experiment setup for active joint offset value estimation (nests in orange) and link length estimation (nests in orange and blue) on the second five-bar mechanism

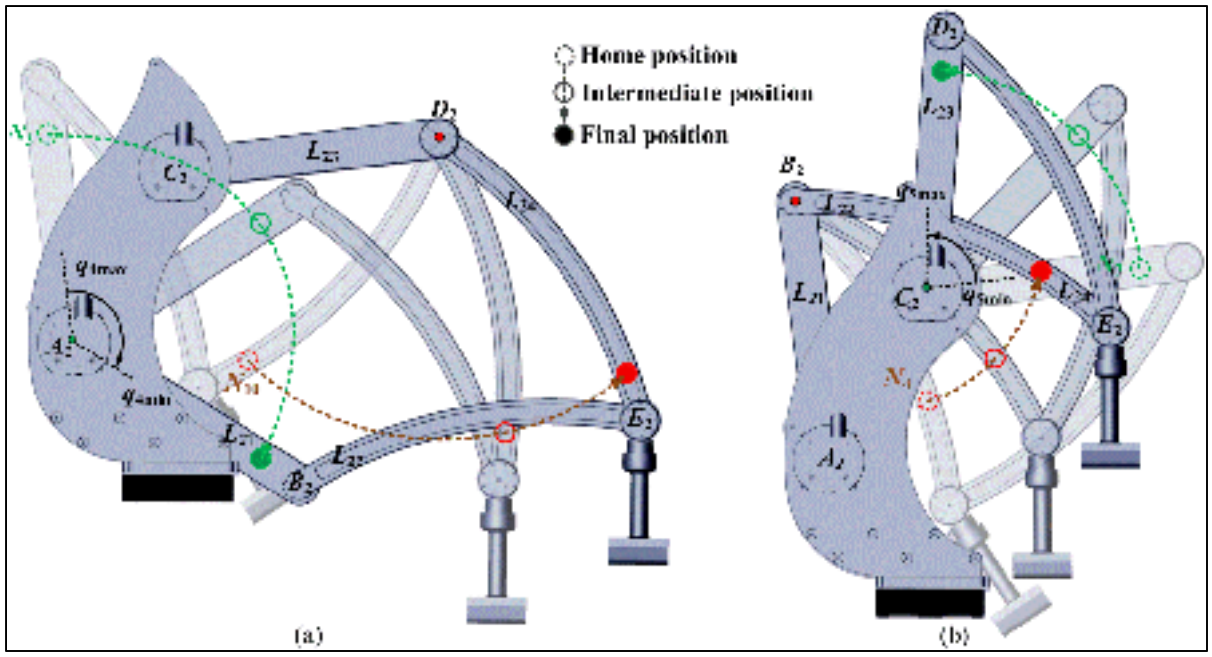

Figure 3.7 Path planning in the experiment of active joint offset error (i=1,2): (a) determine coordinates of A_i and D_i, (b) determine coordinates of B_i and C_i

The first experiment is designed to determine the coordinates of A_2 and D_2 (Figure 3.7(a)) as follows:

i. Two nests denoted N_3 and N_{10} are attached to links L_{21} and L_{24} respectively, as shown in Figure 3.6 and Figure 3.7(a).The robot starts from its home position, which is illustrated with the highest transparent image in Figure 3.7(a).

ii. The angle of joint q_4 is increased gradually with a step of 2°, within a range of 130°. Meanwhile, link L_{23} is kept in its home position throughout experiment process. At each motion step, the robot motion is halted, and measurements of N_3 and N_{10} are taken.

iii. The measured positions of N_3 and N_{10} — which follow circular curves centered at A_2 and D_2 respectively — are fitted to two circles (Taubin, 1991) in order to determine the coordinate of A_2 and D_2.

For illustration purposes, an intermediate position of MedRUE is illustrated with intermediate transparency, and the opaque image shows the final position of MedRUE. The

nests N_3 and N_{10} are demonstrated with dashed circle, solid circle and filled circle in these positions respectively.

To determine the coordinates of B_2 and C_2 we used the same approach as for A_2 and D_2. The used nests are denoted N_4 and N_7, and are attached to links L_{22} and L_{23} respectively, as shown in Figure 3.6. The experiment is illustrated in Figure 3.7(b).

As shown in Figure 3.2(a), the coordinates of A_2 and B_2 evaluate the orientation of links L_{21} in the y_0z_0 plane. The orientation of the link L_{21} is driven directly by active joint q_4. Thus, the joint offset $\tilde{q}_4$ is represented by the difference between the nominal value $\hat{q}_4$ and the evaluated orientation of L_{21} at the home position:

$$\tilde{q}_4 = \text{atan2}\left(-\left(y_{B_2} - y_{A_2}\right), \left(z_{B_2} - z_{A_2}\right)\right) - \hat{q}_4, \tag{3.31}$$

where y_{A2} and z_{A2} are the y and z coordinates of A_2 w.r.t. $\mathcal{F}_0$. Similarly, the joint offset error of q_5 is evaluated by the coordinates of C_2 and D_2.

$$\tilde{q}_5 = \text{atan2}\left(-\left(y_{D_2} - y_{C_2}\right), \left(z_{D_2} - z_{C_2}\right)\right) - \hat{q}_5. \tag{3.32}$$

The active joint offsets of q_2 and q_3, related to the first five-bar mechanism, are assessed similarly to q_4 and q_5, by using the coordinates of A_1, B_1, C_1 and D_1.

3.4.3 Assembling parameters

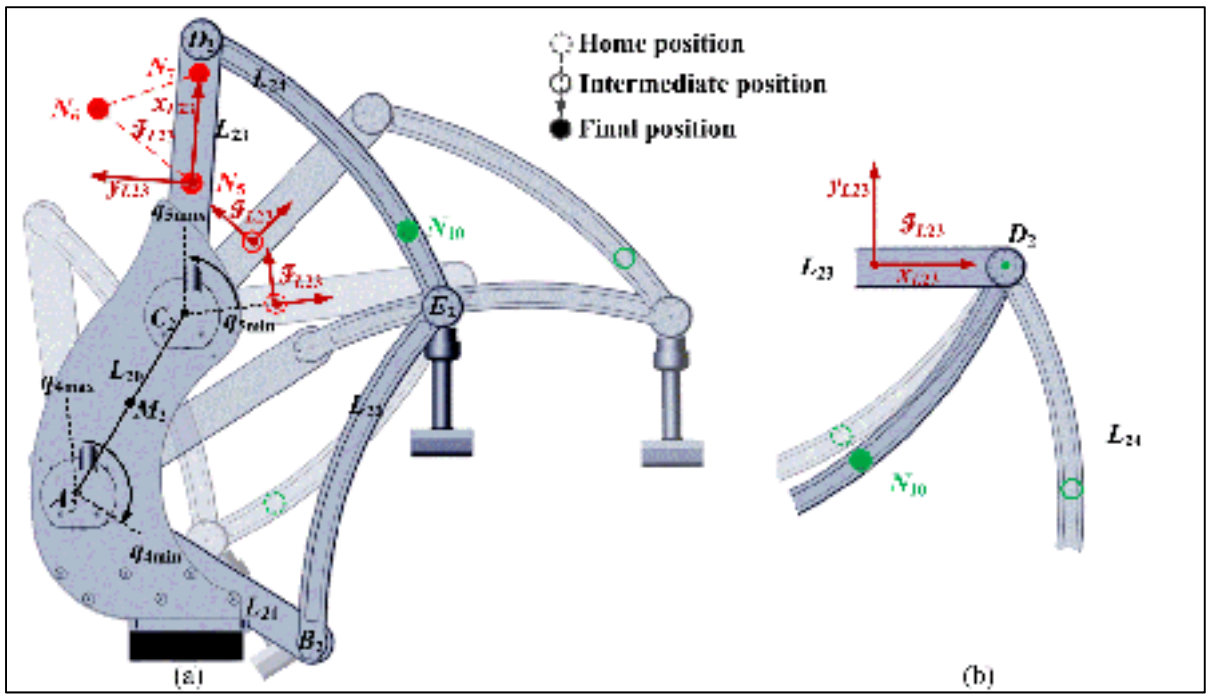

Figure 3.8 Experiment to assess the link length l_{23} (a) link reference frame and nests displacement during robot motion (b) trajectory of nest N_{10} w.r.t. to link reference frame $\mathcal{F}_{L23}$

The assembling parameters are y_{O1}, z_{O1}, y_{O2}, z_{O2}, θ_1, θ_2, and these describe the assembly of the two five-bar mechanisms on the robot base. The i^{th} (i = 1, 2) five-bar mechanism is assembled on the robot base at joints A_i and C_i. As shown in Figure 3.2(a), O_i is the middle point of link L_{i0} defined by A_i and C_i. Angle θ_i illustrates the orientation of link L_{i0} in y_0z_0 plane. Knowing that the coordinates of A_i and C_i are obtained in previous subsection, the assembling parameters are calculated as follows:

$$y_{O_i} = \frac{y_{A_i} + y_{C_i}}{2}, \tag{3.33}$$

$$z_{O_i} = \frac{z_{A_i} + z_{C_i}}{2}, \tag{3.34}$$

$$\theta_i = \text{atan2}\left(-\left(y_{C_i} - y_{A_i}\right), \left(z_{C_i} - z_{A_i}\right)\right). \tag{3.35}$$

3.4.4 Link length parameters

The assessment of the link length parameters is demonstrated by using the second five-bar mechanism (i.e. l_{20}, l_{21}, l_{22}, l_{23} and l_{24}), while those for the first mechanism (i.e. l_{10}, l_{11}, l_{12}, l_{13}, l_{14}) are obtained similarly.

The link length of L_{20} is determined by using the coordinates of A_2 and C_2 w.r.t. $\mathcal{F}_0$, which were obtained in subsection 4.2:

$$l_{20} = \sqrt{\left(x_{C_2} - x_{A_2}\right)^2 + \left(y_{C_2} - y_{A_2}\right)^2 + \left(z_{C_2} - z_{A_2}\right)^2} \,. \tag{3.36}$$

The identification of l_{21}, l_{22}, l_{23} and l_{24} is carried out by moving simultaneously joints q_5 and q_4 inside their limit ranges, as shown in Figure 3.8(a).

Note that link L_{20} has both endpoints A_2 and C_2 fixed w.r.t. $\mathcal{F}_0$. However, for the other links, one or both endpoints change positions during the experiment. To find the position of endpoints B_2, D_2 and E_2, reference frames are attached to the corresponding links. For example, Figure 3.8(a) shows a link frame $\mathcal{F}_{L23}$, which is associated with link L_{23} and defined by N_5, N_6 and N_7. Therefore, the movement of the nest N_{10}, seen from $\mathcal{F}_{L23}$ as shown in Figure 3.8(b), makes a circle centered at D_2. The coordinates of D_2 w.r.t. $\mathcal{F}_{L23}$ are then transformed to be w.r.t. $\mathcal{F}_0$.

The coordinates of B_2 and E_2 w.r.t. $\mathcal{F}_0$ are determined in similar ways as D_2. Point B_2 is determined by observing nest N_4 in link reference frame $\mathcal{F}_{L21}$ (built by nests N_1, N_2 and N_3). Then, E_2 is determined by observing nest N_4 in link reference frame $\mathcal{F}_{L24}$ (built by nests N_8, N_9 and N_{10}). With all coordinates of A_2, B_2, C_2, D_2 and E_2 given w.r.t. $\mathcal{F}_0$, the length of the links are estimated as follows:

$$
\begin{aligned}
l_{21} &= \sqrt{\left(x_{B_2} - x_{A_2}\right)^2 + \left(y_{B_2} - y_{A_2}\right)^2 + \left(z_{B_2} - z_{A_2}\right)^2} \\
l_{22} &= \sqrt{\left(x_{E_2} - x_{B_2}\right)^2 + \left(y_{E_2} - y_{B_2}\right)^2 + \left(z_{E_2} - z_{B_2}\right)^2} \\
l_{23} &= \sqrt{\left(x_{D_2} - x_{C_2}\right)^2 + \left(y_{D_2} - y_{C_2}\right)^2 + \left(z_{D_2} - z_{C_2}\right)^2} \\
l_{24} &= \sqrt{\left(x_{E_2} - x_{D_2}\right)^2 + \left(y_{E_2} - y_{D_2}\right)^2 + \left(z_{E_2} - z_{D_2}\right)^2}
\end{aligned}
\tag{3.37}
$$

3.4.5 Parameter calibration results and validation

To validate the proposed calibration method, we perform the same experiment with nominal and calibrated parameters. Both the nominal and identified values of calibrated parameters are listed in Table 3.4.

Table 3.4 Nominal and identified parameter values

	Nominal value	**Calibrated value**
Link length of Five-bar mechanisms (unit)		
l_{10} (mm)	150	151.580
l_{11} (mm)	400	400.510
l_{12} (mm)	520	518.605
l_{13} (mm)	400	400.656
l_{14} (mm)	520	523.003
l_{20} (mm)	150	151.007
l_{21} (mm)	400	400.401
l_{22} (mm)	520	523.075
l_{23} (mm)	400	400.926
l_{24} (mm)	520	526.285

(Table continued)		
Assembling of five-bar mechanisms (unit)		
y_{O1} (mm)	−158	−153.714
z_{O1} (mm)	308	305.442
y_{O2} (mm)	−158	−156.169
z_{O2} (mm)	308	309.001
θ_1 (°)	150	148.906
θ_2 (°)	150	150.583
Active joint offset error (unit)		
$\tilde{q}_2$ (°)	0	1.445
$\tilde{q}_3$ (°)	0	−0.730
$\tilde{q}_4$ (°)	0	1.521
$\tilde{q}_5$ (°)	0	−0.093
The world reference frame (unit)		
x_W (mm)	−110	−115.587
y_W (mm)	−136	−140.868
z_W (mm)	30	27.452
γ_W (°)	0	0.292
β_W (°)	0	−0.057
α_W (°)	0	0.286

The robot's position accuracy assessment after calibration obtained by using the ISO 9283 evaluation approach is shown in Table 3.5. The maximum absolute position error (i.e. absolute accuracy) has been improved from 5.770 mm before calibration to 0.764 mm after calibration. The relative accuracy is also important in the medical application, and its accuracy is satisfactory after calibration. The maximum relative position error was improved from 3.018 mm before calibration to 0.489mm after calibration, as shown in Table 3.5.

Table 3.5 Absolute position accuracy (*APA*) and relative position accuracy (*RPA*) after calibration (mm)

	P_1	P_2	P_3	P_4	P_5	P_6	P_7	P_8	P_9
APA	0.612	0.497	0.449	0.351	0.764	0.341	0.343	0.751	0.576
APA_x	0.527	0.469	0.353	0.309	0.752	0.284	0.341	0.730	0.499
APA_y	0.235	0.152	0.228	0.158	0.053	0.122	0.040	0.165	0.284
APA_z	0.202	0.054	0.155	0.047	0.123	0.144	0.003	0.057	0.020
RPA	—	0.259	0.382	0.253	0.276	0.489	0.396	0.294	0.201
RPA_x	—	0.066	0.132	0.156	0.157	0.313	0.249	0.254	0.029
RPA_y	—	0.107	0.029	0.058	0.212	0.103	0.235	0.070	0.076
RPA_z	—	0.227	0.357	0.191	0.082	0.361	0.198	0.130	0.184

Figure 3.9 illustrates the improvement of accuracy when the robot is tracking a reference command line, which is marked in blue solid line. As shown in Figure 3.9(a) and Figure 3.9(b), which represent the trajectory projection on planes *xy* and *xz* respectively, the trajectory before calibration has a significant error (poor absolute accuracy), and it is greatly improved after the calibration.

Figure 3.9(c) and Figure 3.9(d) illustrate the relative position offset between adjacent points. Since the reference command line is created by a set of points with constant offsets, the relative position offsets are represented as a fixed point (illustrated by an asterisk). The obtained offsets before calibration are illustrated by green squares: ideally all these squares should coincide with the reference offset (i.e. the blue asterisk mark). However, they scattered around the reference offset because of the robot parameter residuals. The obtained results (offsets) after calibration are illustrated in red triangles and it clearly demonstrates the improvement of the robot relative accuracy: i.e. the obtained relative position offsets converge towards to the reference offset.

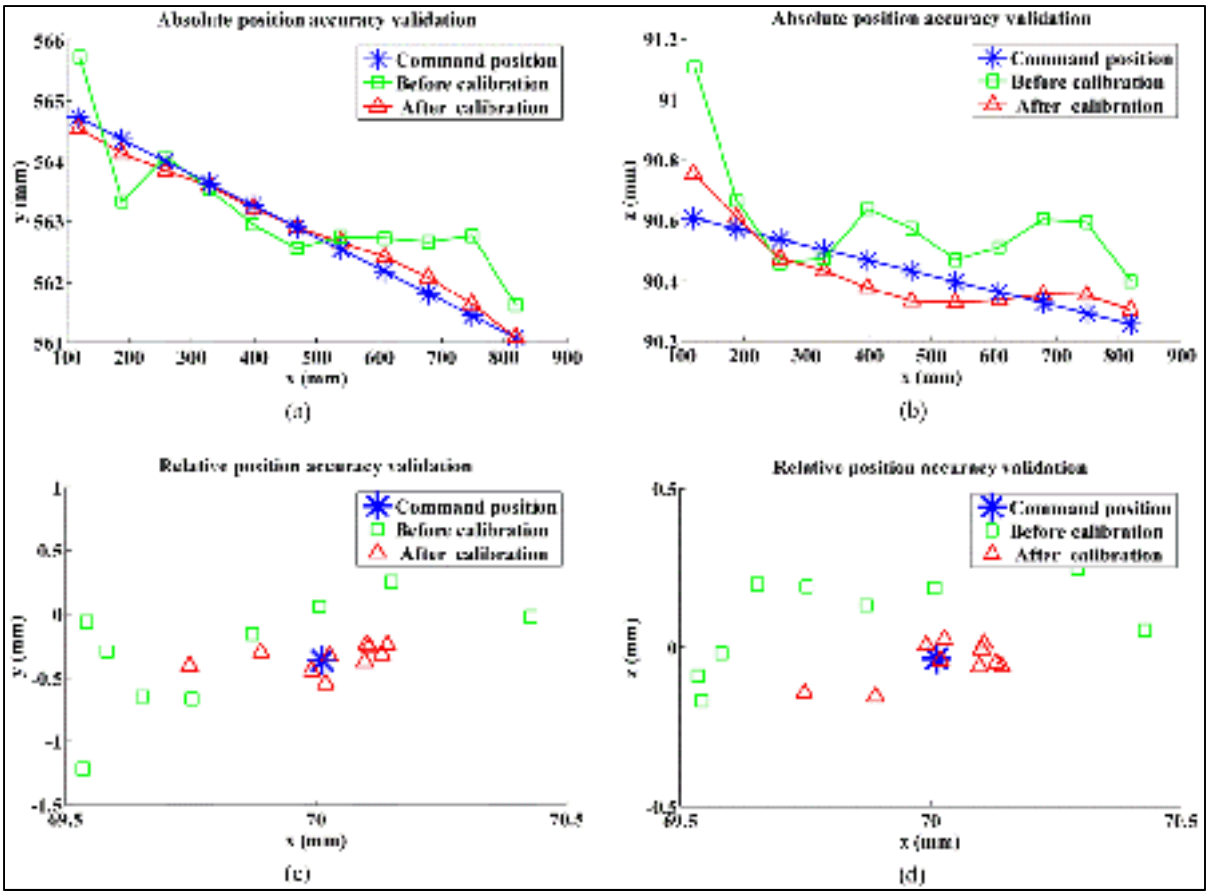

Figure 3.9 Accuracy improvement in tracking a reference (command) line: Absolute accuracy improvement by observing the trajectory in *xy* plane (a) and *xz* plane (b); Relative accuracy improvement in *xy* plane (c) and *xz* plane (d)

Table 3.6 Comparison of proposed calibration method and standard calibration method

	Proposed method	**Standard calibration method**
Kinematic parameter identification	Individually, more accurate	All parameters identified simultaneously, less accurate
End-effector accuracy	Good	Optimized for end-effector accuracy
Complex computation	No	Yes
Robotic calibration knowledge	Basic	Advanced
Time consumption	More time for experiment	Less time for experiment, more time in method developing and computation

The calibration method demonstrated in this section can be used for many other kinds of serial or parallel robots as well. As it is based on direct measurements, it provides more accurate parameter identification than conventional standard calibration methods based on optimization (e.g. forward calibration and reverse calibration method). The proposed method also requires no complex computation (e.g. identification Jacobian matrix, observability analysis) or advanced optimization knowledge in calibration. The comparison between proposed calibration method and standard calibration method are summarized in Table 3.6.

3.5 Conclusion

An assessment method of the repeatability and the accuracy of a new medical robot were presented. The complete kinematic model of the robot was introduced, and the corresponding parameters were calibrated by a direct measurement method. The proposed method is very easy to implement and requires minimum knowledge on advanced calibration techniques. This approach was validated through experiments, which demonstrated a significant improvement of the position accuracy from about 6 mm before calibration to less than 1 mm after calibration. Thus, the presented method has great potential value in robot calibration when advance techniques are not available or not necessary.

CHAPTER 4

A NEW PASSIVITY-BASED APPROACH OF VARIABLE ADMITTANCE CONTROL

Longfei Zhao, Ilian A. Bonev and Pascal Bigras
Department of Automated Manufacturing Engineering, École de technologie supérieure,
1100 Rue Notre-Dame Ouest, Montréal, Québec H3C 1K3

This paper has been submitted as an article in
Control Engineering Practice

Abstract

Variable admittance control extends applications of conventional admittance control to variable environments. However, it is hard to find a general solution to stability analysis that can be qualified with different variation laws. In this paper, a new passivity-based control is presented to ensure the passivity of the general variable admittance control, and it ensures the stability of variable admittance model consequently. Our proposed control law detects the active state of the variable admittance model, and modifies the parameter of the admittance model to work under a passive state. The proposed controller is validated on a parallel robot with a general variable admittance controller.

Keywords: Passivity-based control, stability, variable admittance control, human-robot interaction.

4.1 Introduction

Admittance control has become a popular method for designing force controllers in human-robot interaction. An admittance model takes force as an input, and its output is the desired motion (position, velocity, and acceleration) to the robot's motion controller (Hayward and MacLean, 2007; Linde and Lammertse, 2003; Maclean and Hayward, 2008). However, the conventional admittance model has fixed parameters, which are determined by the properties of its solitary environment. Studies on human-robot interaction show that the stiffness of the human arm varies greatly, depending on the degree of muscle activation (Gomi, Koike and Kawato, 1992). In such a case, an admittance controller with an unchanged configuration would exhibit a sluggish response in a softer environment, and may become unstable in a harder one.

The variable admittance control has already been studied to enhance its performance in interacting with a variable environment. Nevertheless, the stability issue of variable admittance control has been rarely studied. Moreover, in variable admittance control it is hard to find a general solution to stability analysis under diverse parameter variation laws (PVL). A variable control for human-robot interaction has been proposed, based on estimating human arm stiffness and damping properties (Ikeura and Inooka, 1995; Tsumugiwa, Yokogawa and Hara, 2002). However, their results are based on a pre-set motion routine, rather than on the arbitrary motion of most human-robot interactions. Proof of stability was not provided either. Many variable admittance controllers only adjust virtual damping, and neglect the potential contribution of variations of virtual mass (Duchaine and Gosselin, 2007; Rahman, Ikeura and Mizutani, 1999; Tsumugiwa, Yokogawa and Hara, 2002). The stability of this approach is discussed in (Duchaine and Gosselin, 2008; Duchaine et al., 2012). Nevertheless, the virtual mass is set to constant in variable admittance design. Consequently, the flexibility of the variable admittance model is restrained to a certain degree. In a general variable admittance controller, however, both virtual mass and virtual damping should be adjustable to achieve the desired dynamic property of the admittance model. Recently, a practical implementation of variable admittance control was developed

(Lecours, Mayer-St-Onge and Gosselin, 2012), and both virtual mass and damping were modified according to an estimated stable region. However, the stable region was estimated by interpolating certain discrete parameter samples. Notwithstanding, this modification is insufficient to prove stability in the cases other than the parameter samples. Moreover, a stable region estimated by invariant parameter samples is inappropriate for validating the stability of a dynamic admittance control with variable parameters.

Passivity theory has become a common method in the stability analysis of robot control systems (Albu-Schäffer, Ott and Hirzinger, 2007; Berghuis and Nijmeijer, 1993; Canudas-de-Wit and Kelly, 2007; Jee-Hwan, Dong-Soo and Hannaford, 2004; Siciliano and Villani, 1996; Yongqiang et al., 2011). Passive systems have been proved to be stable in a conservative approach (Bao and Lee, 2007). The passivity theory analyzes stability from the point view of energy, and does not require the explicit model of the system. This great advantage makes passivity theory popular in the analysis of complex nonlinear systems, whose stability issues are very hard to analyze by conventional methods.

In this paper, a passivity-based variable admittance controller is presented for human-robot interaction. The main contribution of our proposed controller is a novel implementation of the passivity theory, that of integrating passivity theory into a variable admittance controller. It provides a general solution to the stability analysis of the admittance model, regardless of the diversity of the parameter variation laws of admittance model. The proposed controller has been improved based on simulation analysis, and validated on a new parallel medical robot.

The remainder of this paper is organized as follows: In Section 2, the passivity property of a general variable admittance model is discussed, and our proposed method is presented to ensure the passivity property of the admittance model. The passivity control law has been improved to reduce the chatter effect of the proposed variable structure control. Simulation results are provided to illustrate the design and improvement of the proposed passivity controller. In Section 3, the proposed passivity-based variable admittance controller is tested

on a robot platform, and the experiment's result is discussed. Finally, a conclusion together with future work is presented in Section 4.

4.2 Passivity control in variable admittance model

4.2.1 Passivity of variable admittance model

In a conventional admittance controller design, an admittance model is conceived with fixed admittance parameters. The most common admittance model is a second-order mass-damping system, which can be demonstrated as:

$$f_h = m\ddot{x} + c\dot{x} + kx \tag{4.1}$$

where x is the position offset from the equilibrium position; f_h is the interaction force on the robot and m, c and k are constant admittance parameters, namely mass, damping, and stiffness.

In the variable admittance control, the admittance parameters are modified by the desired PVL, according to the dynamic properties of the interaction in real time. The stiffness parameter is generally negligible in human-robot interaction according to the research result in (Ikeura, Monden and Inooka, 1994). Thus, the variable admittance model can be expressed as:

$$f_h = m(t)\ddot{x} + c(t)\dot{x} \tag{4.2}$$

The PVL of $m(t)$ and $c(t)$ are functions of time. The dynamic property of the admittance model is characterized by the PVL of $m(t)$ and $c(t)$, which may be designed very differently according to the desired motion and property of the robot's system and the human element.

The passivity theory describes the system from the point of view of energy flow. The general form of the passivity theory can be expressed as follows:

$$\dot{E}(t) = y^T u - g(t). \tag{4.3}$$

where u is the system input and y is the system output; $E(t)$ is the stored energy, and $g(t)$ is the dissipative power. A system is said to be passive if, in the equation of the form of (4.3), $E(t)$ is lower bounded and $g(t) \geq 0$ (Slotine and Li, 1991).

Regarding to the variable admittance model (4.2), the stored energy is

$$E(t)=\frac{1}{2}m(t)\dot{x}^2 \tag{4.4}$$

Differentiating (4.4) on both sides, and substituting (4.2) into the result gives:

$$\dot{E}(t)=f_h\dot{x}-\frac{1}{2}\left(2c(t)-\dot{m}(t)\right)\dot{x}^2 \tag{4.5}$$

Equation (4.5) demonstrates the energy of the general variable admittance model (4.2) in the passivity theory format (4.3). The interaction force f_h and the velocity $\dot{x}$ are respectively the input and output of the admittance model, while the dissipative power is

$$g(t)=\frac{1}{2}\left(2c(t)-\dot{m}(t)\right)\dot{x}^2 \tag{4.6}$$

According to the definition of the passivity theory, the variable admittance model (4.2) is passive if (4.4) is lower bounded and (4.6) is non-negative. The quadratic form of (4.4) guarantees that the stored energy $E(t)$ has a lower boundary. Thus, if (4.6) is greater or equal to zero, the variable admittance model is a passive system. By eliminating the quadratic terms in (4.6), the passivity criterion for the variable admittance model is simplified as

$$\dot{m}(t)-2c(t)\le 0 \tag{4.7}$$

If (4.7) is satisfied, then the admittance model with parameters $m(t)$ and $c(t)$ is passive. Otherwise, the admittance model is active.

4.2.2 A passivity controller design for variable admittance model

We propose a passivity controller (PC) to ensure that the variable admittance model will possess a passivity property in real time. The PC has no effect when the system is working in a passive state. However, when the system desists from the passive state, the PC modifies the parameters of the variable admittance model, in order to satisfy the passivity criterion (4.7) with the modified parameters. The PC aims to constrain the system in a passive state, but preserve the features of the variable admittance control to their utmost. Since virtual damping has more influence over virtual mass in variable admittance control (Ikeura, Monden and Inooka, 1994), $c(t)$ retains the same value in the PVL, but virtual mass $m(t)$ is modified to

$\hat{m}(t)$ to satisfy the passivity criterion. Therefore, the passivity criterion will always be satisfied with the modified virtual mass $\hat{m}$ after the execution of the PC:

$$\dot{\hat{m}}(t) - 2c(t) \le 0 \tag{4.8}$$

It is important to notice the different significance of (4.7) and (4.8). The former acts as a passivity observer, and monitors the passivity property of the variable admittance controller. More precisely, it checks the passivity property of admittance model with parameters provided by the PVL. When (4.7) is violated, the PC starts its execution. Therefore, (4.7) is the passivity criterion for triggering the proposed PC. In contrast, the latter represents the result of the PC. The virtual mass will be modified to $\hat{m}$ by the PC, so that (4.8) stands true. Consequently the passivity property of the admittance model is ensured according the discussion in 2.1. From an energy point of view, the dissipative power of the admittance model after the execution of the PC is:

$$g(t) = \frac{1}{2}\left(2c(t) - \dot{\hat{m}}(t)\right)\dot{x}^2 \ge 0 \tag{4.9}$$

Since the execution of the PC depends on the observation of the passivity criterion (4.7), the PC law is designed as a variable structure controller:

$$\hat{m}(t) = \begin{cases} -2\int c(t)\,\mathrm{sign}\left(\tilde{m}(t)\right)dt + m_{\Pi} & \text{if } \Pi \text{ is } True \\ m(t) & \text{if } \Pi \text{ is } False \end{cases} \tag{4.10}$$

where $\tilde{m}(t) = \hat{m}(t) - m(t)$ represents the modification difference of the virtual mass; Π is a Boolean value, which is also considered as an active flag of admittance model with parameters from the PVL:

$$\Pi = \begin{cases} True & \text{if } \dot{m}(t) - 2c(t) > 0 \\ False & \text{if } \dot{m}(t) - 2c(t) \le 0 \end{cases} \tag{4.11}$$

where m_{Π} is the instantaneous value of $m(t)$ when the PC starts its execution. The sign function is-defined as

$$\mathrm{sign}(x) = \begin{cases} 1 & \text{if } x > 0 \\ -1 & \text{if } x \le 0 \end{cases} \tag{4.12}$$

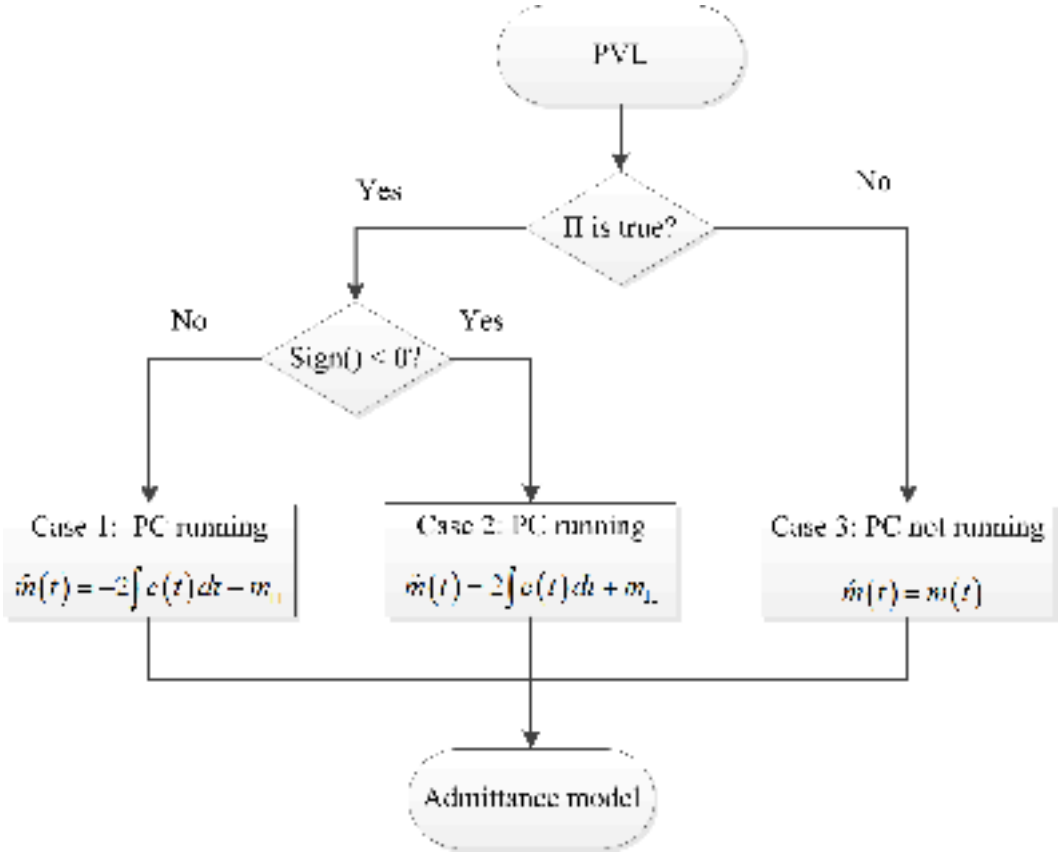

Figure 4.1 Diagram of the PC law

The PC law (4.10) is demonstrated in the diagram in Figure 4.1. The active flag Π is checked by parameters from the PVL. In Case 3, the admittance model is passive under the parameters from the PVL. Virtual mass $m(t)$ is passed directly as $\hat{m}(t)$ to the admittance model, and thus the PC does not execute. In both Case 1 and Case 2, the admittance model is active under the parameters from the PVL. According to the sign function, $\hat{m}(t)$ may have two different formulas, and they both satisfy (4.8) as virtual damping $c(t)$ is a positive value. Thus, the admittance model becomes passive with PC. Furthermore, the PC law in (4.10) is designed to achieve three purposes:

i. $\hat{m}(t)$ is decreased in Case 1 (i.e. $\hat{m}(t) > m(t)$) and increased in Case 2 (i.e. $\hat{m}(t) \le m(t)$). Therefore, with the premise of satisfying (4.8), $\hat{m}(t)$ is modified to

approach $m(t)$. This means that the PC modifies the admittance parameters at least degree to respect the PVL.

ii. When system is passive, $\hat{m}(t)$ equals $m(t)$. When system is active, $\hat{m}(t)$ only decreases if $\hat{m}(t) > m(t)$. Therefore, $\hat{m}(t)$ is ensured to be larger or equal than the minimum value of $m(t)$ in all cases. Since $m(t)$ as defined by the PVL is assumed to be positive, $\hat{m}(t)$ is positive as well.

iii. The specified m_{Π} provides a smooth change at the moment when the PC starts its execution.

4.2.3 Simulation of passivity controller in a variable admittance controller

In this subsection, the proposed PC law (4.10) is simulated with a general variable admittance model. The objective of the simulation is to demonstrate that the proposed PC modifies the admittance parameter to ensure the admittance model is working in a passive state.

A general variable admittance model is provided in (4.2). For simplicity, the interaction force f_h is a square wave with a unit amplitude and frequency. The PVL is designed to set the system in a passive state and active state alternately:

$$m(t) = \cos\left(\frac{2\pi}{5}t\right) + 2 \tag{4.13}$$

$$c(t) = 0.1\sin(t) + 0.2 \tag{4.14}$$

The coefficients in (4.13) and (4.14) are chosen for the purpose of demonstration.

Figure 4.2 shows the comparison of the two simulation results: variable admittance control with and without the PC. The force inputs and the PVL are the same in both experiments. The admittance model starts in a passive state at **A**, and violates the passivity criterion (4.7) at phase **B**-**C** and **D**-**E** with admittance parameters from the given PVL (illustrated in Figure 4.2(a)). The active phases (i.e. Π is true) are illustrated by the red shading, and the PC is

executing during these time phases. Figure 4.2(b) shows the modification of the virtual mass in the second simulation with the PC. During phase **F**-**G**, where the system is passive, $\hat{m}(t)$ is equal to $m(t)$ since the virtual mass from the PVL is passed directly to the admittance model. When the PC begins its execution, $\hat{m}(t)$ deviates from $m(t)$ at **G**. The modified virtual mass changes according to the PC law in (4.10) until **H**, when the admittance model is passive under parameters from the PVL (i.e. Π is false). Figure 4.2(c) compares the change of dissipative power of the admittance model without the PC (4.6) and with the PC (4.9). The PC efficiently regulates $g(t)$ to be non-negative (except for a transient glitch at **N**, which will be discussed in 4.2.4), as a proof of the passivity of the variable admittance model discussed in 4.2.1.

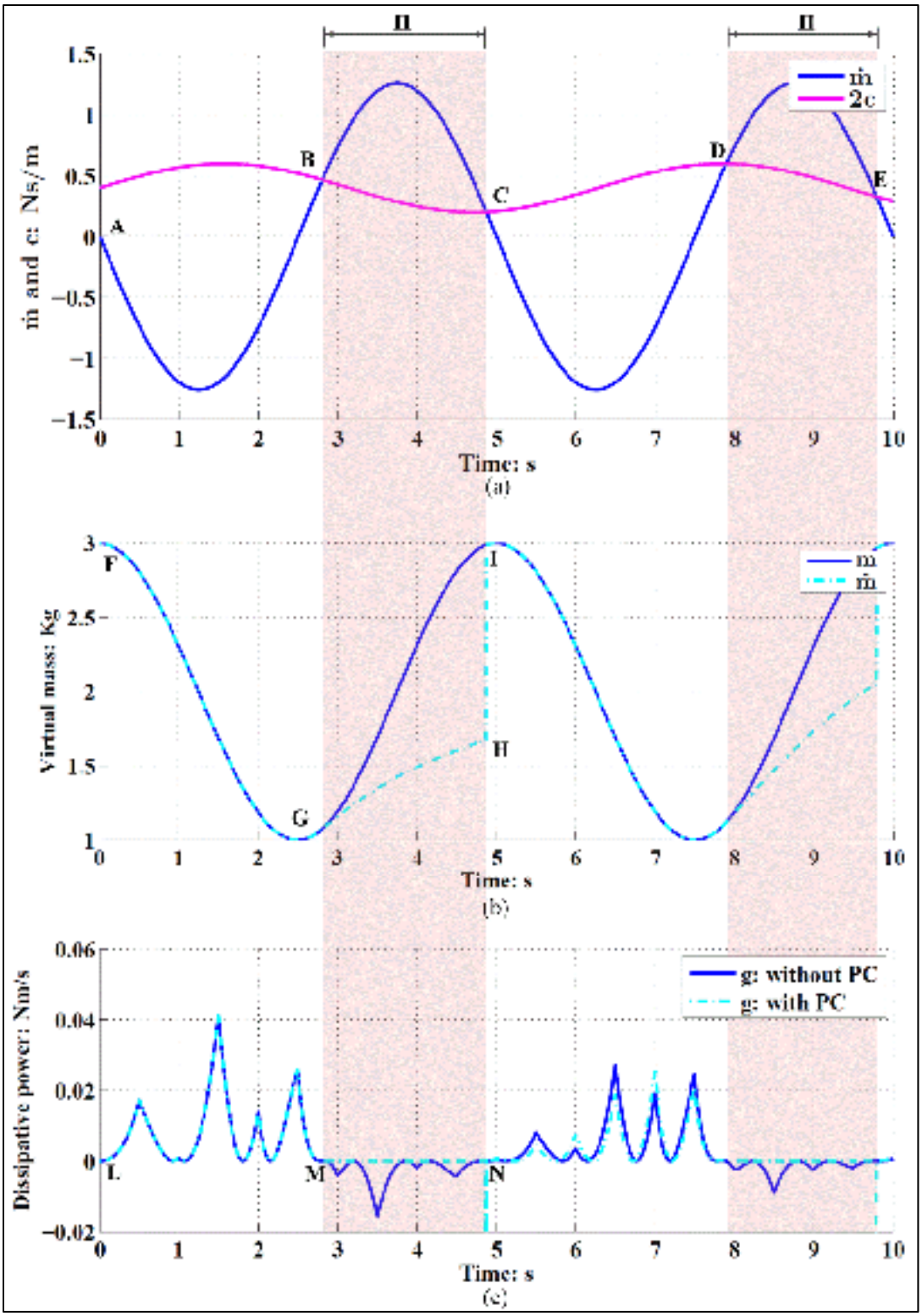

Figure 4.2 PC's effect on the variable admittance model and chatter effect reduction

4.2.4 Chatter effect and its reduction

The chatter effect is a common concern in variable structure controllers in general and is mainly due to the instantaneous change of states when the switch condition is satisfied. Regarding the proposed PC, the controller switches between the two equations in (4.10) when the value of Π is changed, and the moments are illustrated on both sides of the red shaded sections in Figure 4.2. When Π changes to true (e.g. at **B** in Figure 4.2(a)), the virtual mass has a smooth curve at the switch point **G**, thanks to m_{Π} as the integration initial value in (4.10). The chatter effect only occurs when Π returns to false. As shown in Figure 4.2(b), the value of $\hat{m}(t)$ at **H** resets to $m(t)$ at **I** after a sampling-time interval. This instantaneous change in the virtual mass of the admittance model causes the chatter effect of the system, which results in a glitch impulse of the dissipative power at **N** in Figure 4.2(c). It is assumed that the admittance parameters (i.e. virtual mass and damping) have bounded values for ordinary applications, so the dissipative power $g(t)$ is lower-bounded according to (4.9). The glitch impulse has a limited value and only survives for a sampling-time interval.

The chatter effect is reduced by the application of a virtual mass threshold κ. The cessation of the PC's execution is only permitted when $\left|\tilde{m}(t)\right| \le \kappa$, so that the chatter caused by the difference between $\hat{m}(t)$ and $m(t)$ is restrained within a predefined range. A small value of κ provides a smooth change of the virtual mass when the PC stops executing. If $\kappa = 0$, the discontinuity of the state switch is theoretically eliminated. However, the curves of $\hat{m}(t)$ and $m(t)$ can seldom exactly meet at the same value due to certain practical reasons, such as discrete computational precision and sampling-time intervals. It is reasonable to set κ to a proper small value according to the variation rate of the virtual mass. As a reference, the value of κ should be larger than the maximum difference in virtual mass between two successive sampling-time intervals. Given the frequency 500Hz in the simulation, the maximum difference value for successive $m(t)$ and $\hat{m}(t)$ are obtained by the PVL (4.13) and (4.14) — at about 0.0025 and 0.0012 respectively. The chatter effect is eliminated when κ

equals 0.01 in the simulation. The diagram of the improved PC is demonstrated in Figure 4.3. Comparing it to the PC law in Figure 4.1, additional criteria are checked when the admittance model with the PVL parameters is passive. When the PC is running, it continues to reduce chatter if $|\tilde{m}(t)| > \kappa$. Otherwise, the PC stops executing as in Case 3.

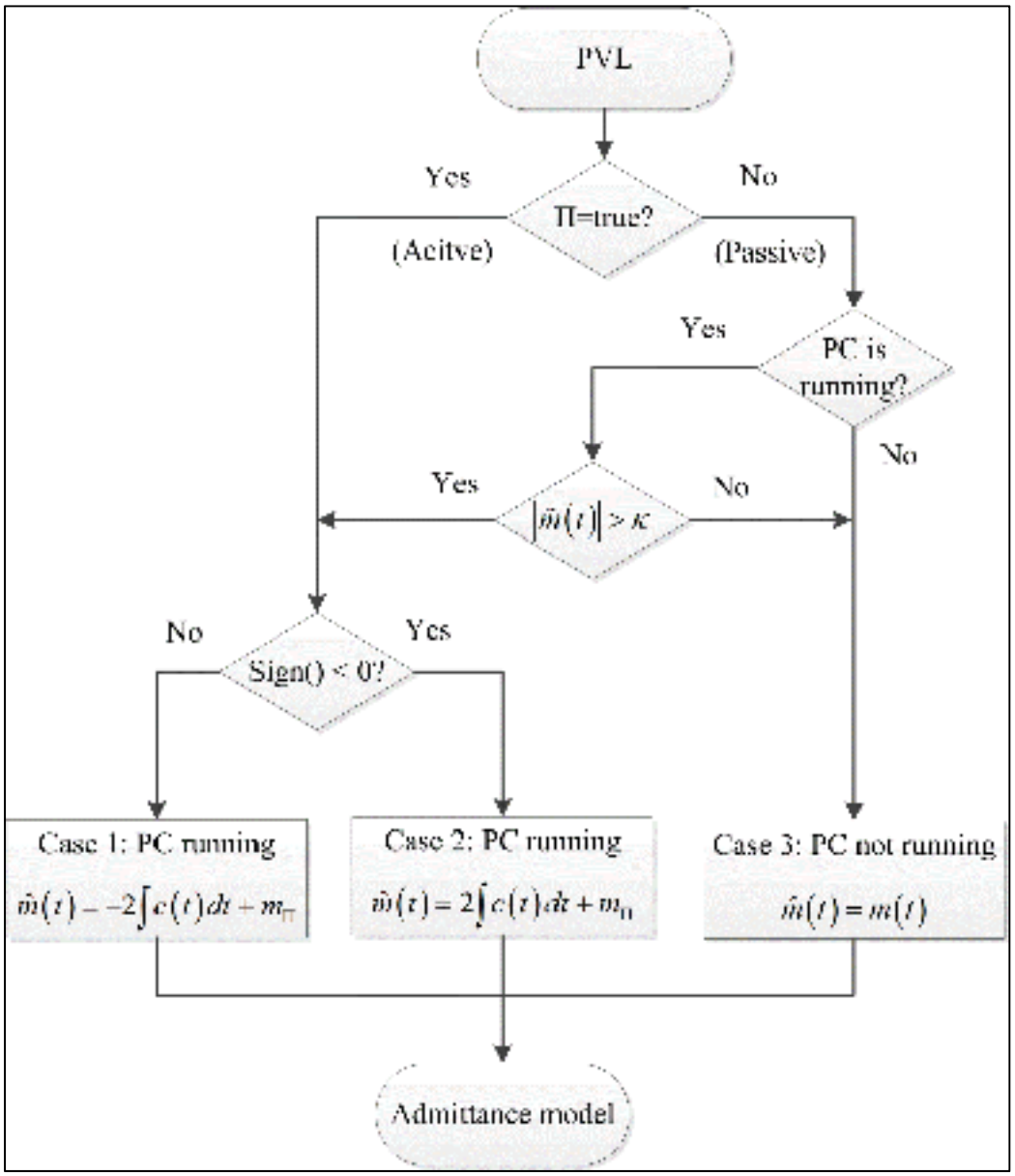

Figure 4.3 Diagram of the improved PC law

According to diagram in Figure 4.3, the PC law (4.10) is rewritten as:

$$\hat{m}(t) = \begin{cases} -2\int c(t)\,\mathrm{sign}\left(\tilde{m}(t)\right)dt + m_{\Pi} & \text{if } \Pi^* \text{ is } \textit{True} \\ m(t) & \text{if } \Pi^* \text{ is } \textit{False} \end{cases} \tag{4.15}$$

where

$$\Pi^* = (\Pi) \ \vee \ (\neg\Pi \wedge \mathrm{P} \wedge \mathrm{K}) \tag{4.16}$$

Symbols $\wedge, \vee$ and $\neg$ are respectively logical *AND*, *OR* and *NEGATION* operators; P and K are Boolean values: P is true if the PC is running, and K is true if $|\tilde{m}(t)| > \kappa$. In (4.16), the term $(\neg\Pi \wedge \mathrm{P} \wedge \mathrm{K})$ represents the condition under which the chatter effect may occur. Though admittance model under PVL parameters is passive in this case, the improved PC continues to execute to reduce chatter effect. Therefore, Π* represents the execution of the improved PC, and the time phase of Π* is equal or longer than the active state flag Π.

Given the same interaction force and PVL as in Figure 4.2(a), the simulation result of the improved PC is shown in Figure 4.4. The virtual mass $\hat{m}(t)$ does not reset to $m(t)$ when Π is false at **H** in Figure 4.4(a) as in the non-improved PC. On the contrary, $\hat{m}(t)$ is continuously modified by the PC until it reaches **H***, where the difference between the two curves $\hat{m}(t)$ and $m(t)$ are below the threshold κ. Thus, the execution period of the PC is extended from **Π** to **Π***. The glitch impulse of dissipative power (at **N** for non-improved PC) disappears correspondingly at **N*** as shown in Figure 4.4(b).

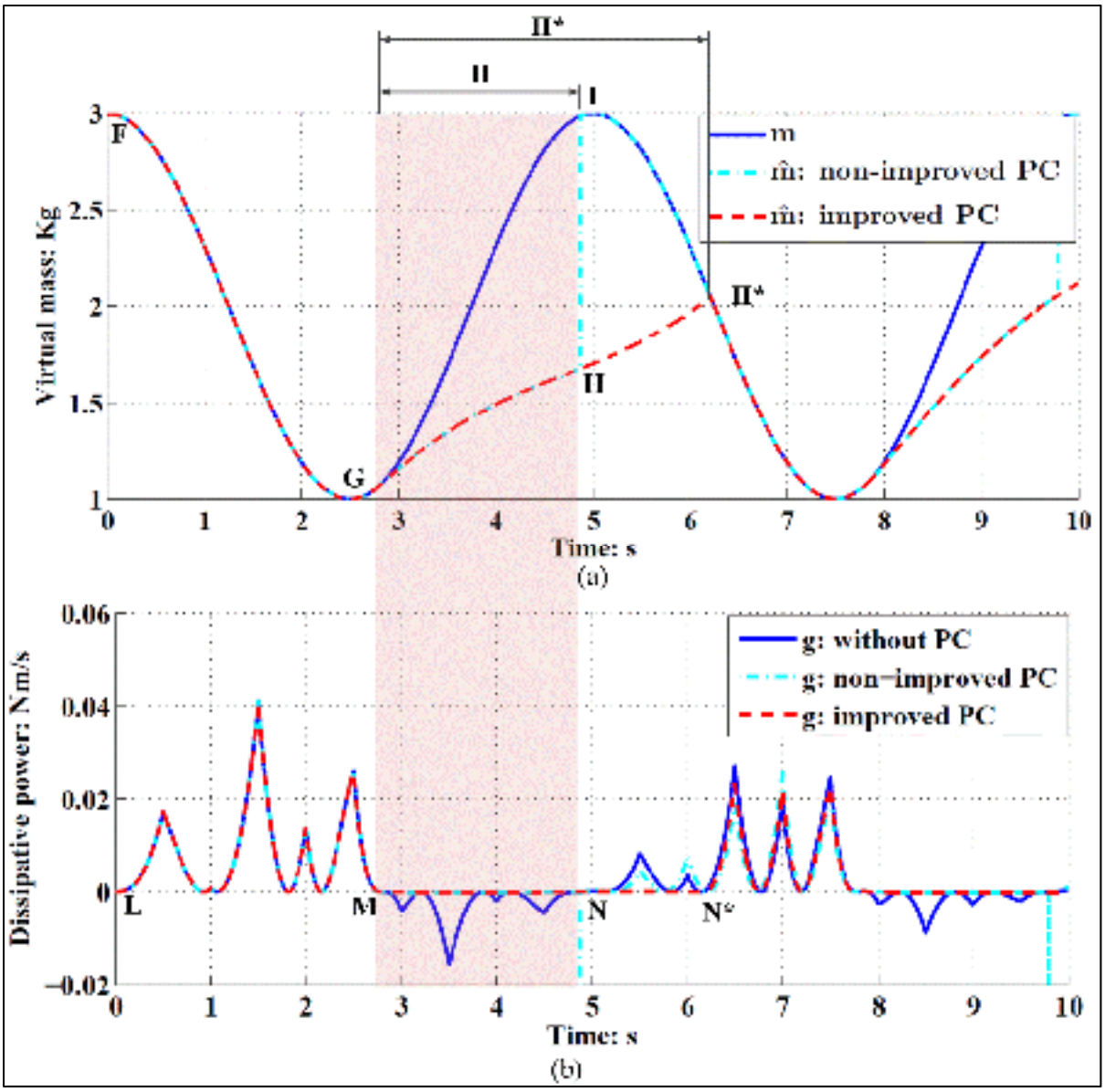

Figure 4.4 Chatter effect reduction by the PC on the variable admittance model

4.3 Experiment on the robot platform

In this section, the experimental setup is presented for the proposed passivity controller of a variable admittance model. Two experiments — variable admittance control with/without the proposed PC — were conducted, and the dissipative powers were monitored to validate the

proposed PC. Discussions of the experiment's hardware, robot control system and the experiments' results are included in this section.

4.3.1 Robot platform and the experiment setup

In our experiments, a parallel robot (i.e. MedRUE) was used to validate our proposed control method. As shown in Figure 4.5, MedRUE is a patented 6 degrees-of-freedom(DOF) parallel robot designed for medical examinations (Zhao et al., 2013). A Mini40 6-channel force/torque sensor is located at the root of the probe. Quanser's hardware-in-the-loop (HIL) card reads data from the force and position sensors, and sends them to the Simulink model at the computer station at a frequency of 500Hz.

Figure 4.5 Experimental setup

Figure 4.5 shows a view of the set-up for validating the proposed control method. An operator holds the probe to lead MedRUE's motion, and the interaction force is recorded from the force sensor as the input of the robot's control system. To maximize the repeatability of the operator's motion in each experiment, an ABB robot was programmed to provide a predefined reference motion. Therefore, the operator endeavors to follow the pointer tool of the ABB robot closely in each experiment, in order to offer an appropriate comparison between the different experiments.

4.3.2 Robot control system

Figure 4.6 demonstrates the implementation of the proposed passivity controller for variable admittance controller in a general robot's motion controller. The variable admittance controller takes the interaction force (i.e. f_h) as input and provides a reference motion (i.e. $\dot{x}, \ddot{x}$) for the robot's motion controller. In the variable admittance controller, the parameters of the admittance model (i.e. $m(t)$ and $c(t)$) are provided by the PVL, and the virtual mass $m(t)$ is regulated to $\hat{m}(t)$ by the PC before being applied to the admittance model. The motion controller of MedRUE contains a computed torque controller, a proportional-integral-derivative (PID) controller and a friction compensator. The proposed passivity-based variable admittance controller is implemented in all 6-DOF of the robot, and the system exhibits a similar performance in each DOF of MedRUE. For demonstration, only the performance of the translation along the linear guide is discussed.

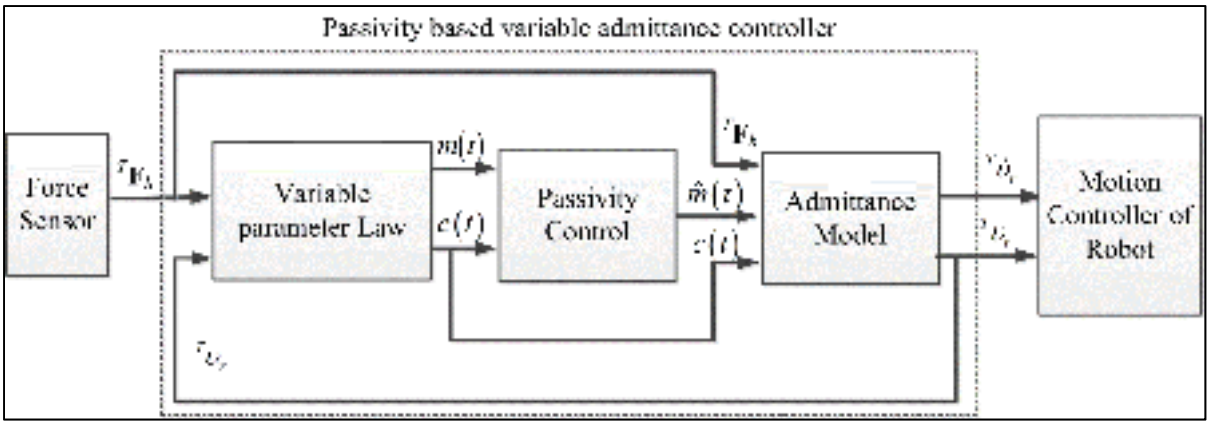

Figure 4.6 Passivity-based variable admittance controller

The PVL of MedRUE is developed based on the method proposed in (Lecours, Mayer-St-Onge and Gosselin, 2012). The PVL of the virtual damping is defined as

$$c(t)=\begin{cases} c_r-\dfrac{c_r-c_{\min}}{|f_h|_{\max}}\left|f_h(t)\right| & \text{robot in acceleration} \\ c_r-\dfrac{c_r-c_{\max}}{|f_h|_{\max}}\left|f_h(t)\right| & \text{robot in deceleration} \end{cases} \tag{4.17}$$

where c_r is a reference damping when the robot is neither in acceleration nor deceleration, $c_{\min}$ and $c_{\max}$ are constant virtual damping limits for the admittance model, and the $|f_h|_{\max}$ is the saturation limit of the interaction force. Their values are experimentally-defined according to the application and the robot platform. The PVL (4.17) decreases the virtual damping when the operator intends to accelerate the robot, and increases it when the operator intends to decelerate the robot. It is assumed that the operator applies force in the same direction as the velocity when he intends to accelerate the robot's motion, and in the opposite direction to decelerate.

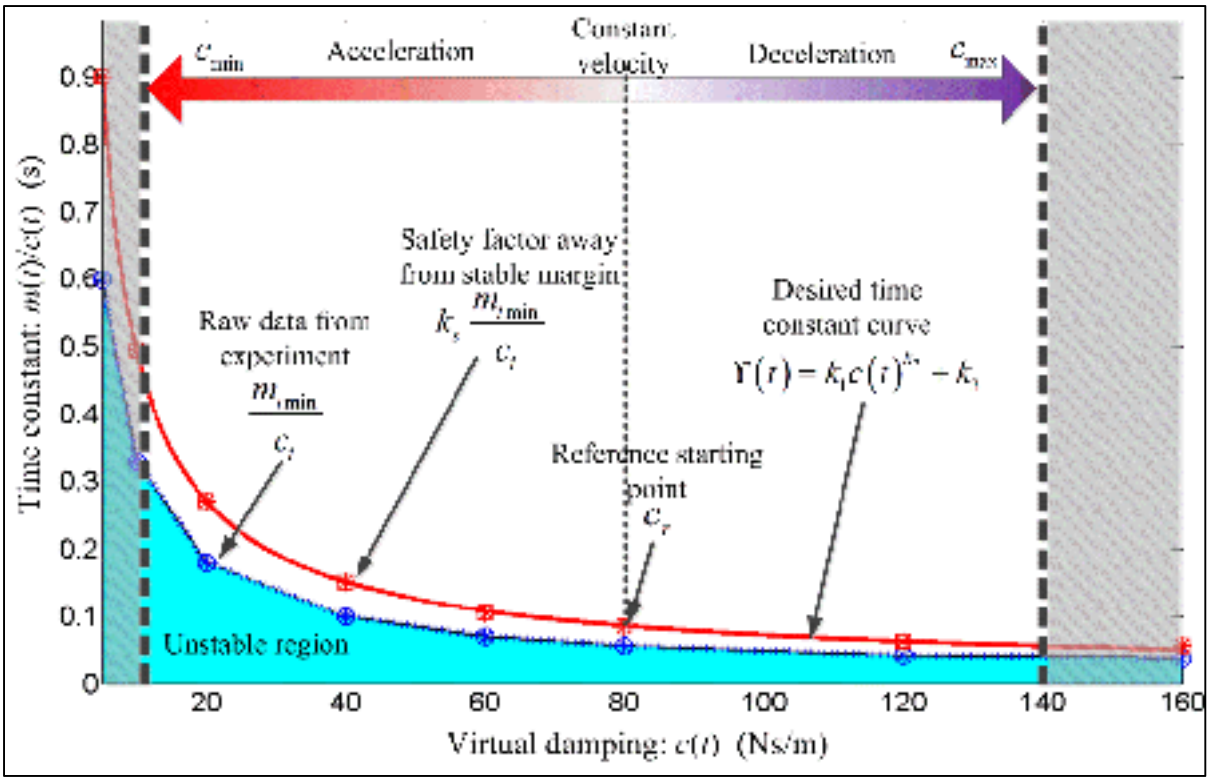

Figure 4.7 Design of the parameter variation law (PVL)

The PVL of virtual mass is determined by designing the time constant function of the admittance model (4.2) as shown in Figure 4.7, and it is obtained by the following steps:

i. Measure the minimum virtual mass: Studies show that the system encounters vibrations and instability problems when the virtual mass is below a certain boundary (Linde and Lammertse, 2003; Tsumugiwa, Yokogawa and Hara, 2002). The minimum virtual mass $m_{i\min}$ is experimentally-measured according to predefined constant samples of virtual damping c_i.

ii. Estimate the unstable region: Knowing that the time constant of the admittance model (4.2) is $m(t)/c(t)$, the unstable region is estimated under the parameter set of *raw samples* $[c_i, m_{i\min}/c_i]$ (Lecours, Mayer-St-Onge and Gosselin, 2012). It is worthy of note that the unstable region was estimated for the design of parameter variation law of admittance model. The stability analysis of admittance model is preceded by our proposed passivity controller.

iii. Build the time constant function: The time constant function $\Upsilon(t) = \frac{m(t)}{c(t)}$ is ideal to provide small values for fast dynamic response. At the meantime, it is practical to keep a certain distance from the unstable margin estimated in the previous step. *Offset samples* are introduced by multiplying a gain k_s to the raw samples, and these are used to fit the curve of the time constant function $\Upsilon(t)$. A candidate curve-fitting function is a power function

$$\Upsilon(t) = k_1 c(t)^{k_2} + k_3 \tag{4.18}$$

where k_1, k_2 and k_3 are parameters of the curve-fitting of the offset samples $k_s \frac{m_{i\min}}{c_i}$.

iv. Obtain the PVL of the virtual mass: Given that $\Upsilon(t)$ has been determined, the PVL of the virtual mass is obtained by

$$m(t) = \Upsilon(t) c(t) \tag{4.19}$$

The parameters for the design of the PVL are based on our experiments and the values are listed in Table 4.1.

Table 4.1 Parameter values for the design of the PVL

PVL	Variable [Unit]	Value
Virtual damping $c(t)$	$\|f_h\|_{\max}$ [N]	10
	c_r [Ns/m]	80
	$c_{\min}$ [Ns/m]	5
	$c_{\max}$ [Ns/m]	160
Virtual mass $m(t)$	k_s	1.5
	k_1	3.712
	k_2	-0.887
	k_3	0.010

4.3.3 Experiment results and discussion

To demonstrate the improvement of our proposed controller, the experiment results without the proposed PC and the experiment results with the improved PC are provided. In practice, two distinct experiments as shown in Figure 4.5 cannot have identical motion. Therefore, the experiment results with/without PC are analyzed individually, rather than being compared in parallel in time phase as they are in the simulation.

The first experiment was performed on MedRUE using a variable admittance control without the PC. Figure 4.8(a) shows that admittance model is possible to work under active state with variable admittance control. The admittance model offends the passivity criterion in phase **B-C** and in phase **D-E**. Accordingly, the dissipative power is below zero during the same time phase (shown in Figure 4.8(b)), which also indicates that the admittance model is generating energy, rather than dissipating energy according to passivity theory definition.

The second experiment was conducted on MedRUE using a variable admittance control with the PC. The virtual mass threshold κ was tuned to 0.2 based on experiments. The passivity criterion (4.7), the virtual mass modification (4.15) and the dissipative power (4.9) are plotted in Figure 4.9. The passivity criterion is violated in both phase **B-C** and phase **D-E** in Figure 4.9(a). The virtual mass is modified by the PC in phase **G-H*** in Figure 4.9(b). In Figure 4.9(c), the dissipative power of the experiment (i.e. g: based on $\hat{m}(t)$) is plotted with dot-dashed line. The dissipative power without the PC from Figure 4.8(b) is not comparable to the dissipative power with the PC in Figure 4.9(c) as these are two different experiments. To provide a general illustration on the effect of PC on dissipative power, a reference dissipative power without PC is provided in a solid line in Figure 4.9(c) for demonstration purpose. It is worthy to notice that the reference dissipative power is computed by $m(t)$—virtual mass before PC's modification. It is an imitation of the dissipative power, rather than a real experiment result as shown in Figure 4.8(b).

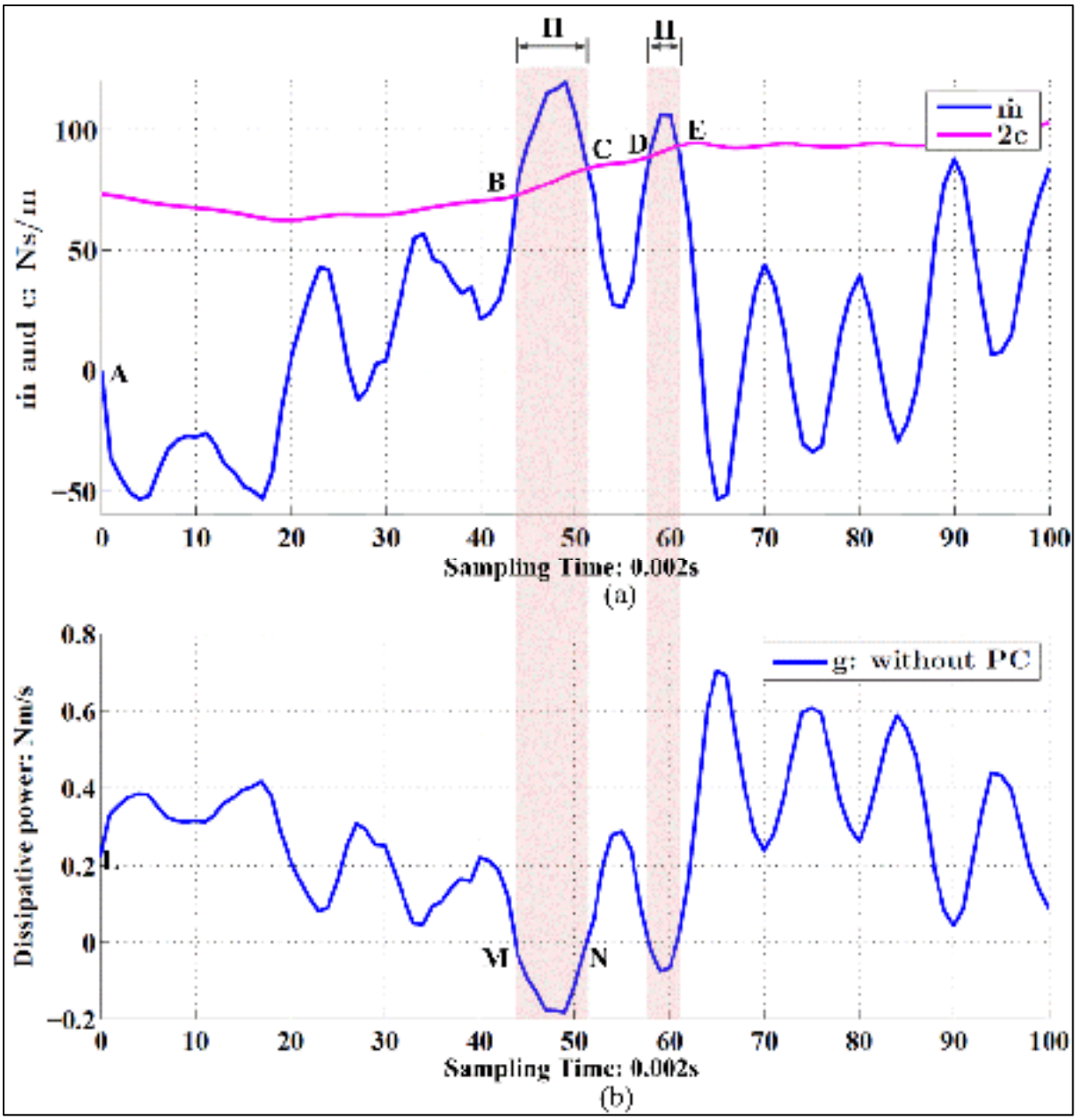

Figure 4.8 Experiment results on MedRUE without PC

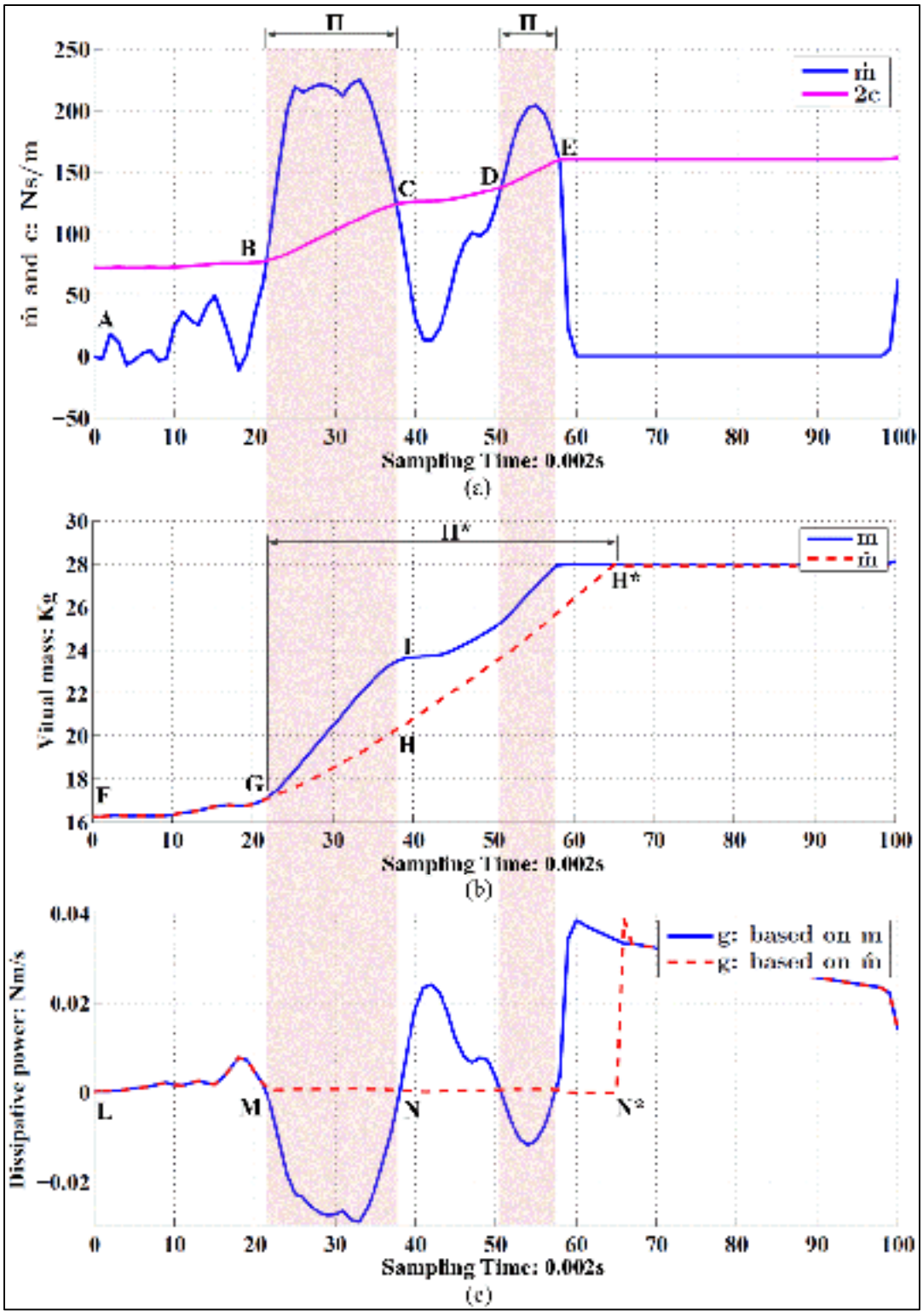

Figure 4.9 Experiment results on MedRUE with the PC

As shown in Figure 4.9(b), the proposed PC takes effect when the passivity criterion is violated (i.e. Π becomes true). When the passivity criterion is satisfied at **C**, the virtual mass does not rise from **H** to **I** abruptly. However, the PC continues to execute until $\hat{m}(t)$ meets $m(t)$ under a predefined threshold κ at **H***. The dissipative power with the PC is constrained to be non-negative as illustrated by the dot-dashed line in Figure 4.9(c). The reference dissipative power (solid line in Figure 4.9(c)) also provides a general concept for demonstrating the effect of the proposed PC in dissipative power.

4.4 Conclusions

In this paper, a novel implementation of the passivity theory is presented for admittance controllers. It constrains the passivity property to provide the stable behavior of admittance model. The proposed passivity controller has a variable structure and the chatter effects are attenuated through the improved design. Simulations on the variable admittance controller are presented to elaborate the development of the passivity control. Experiment results are discussed to validate the proposed methods. The proposed methodology provides a general solution for ensuring the stability of admittance controllers, regardless of the diversity of their parameter variation laws. It can be further developed for the stability analysis of model-based controllers.

GENERAL CONCLUSION

The goal of this research was to provide a solution for assisting sonographers to diagnose peripheral arterial disease in lower limbs. The medical ultrasound robot (MedRUE) and its kinematic model were presented, as well as singularity issues and workspace. Regarding manufacturing and assembling errors in the prototype, the robot was calibrated to improve its position accuracy. The force control of the robot's system to provide stable interaction with humans was discussed.

Compared to other medical ultrasound robots, MedRUE stands out for its capability to diagnose peripheral arterial disease in the lower limbs. It is a six degree-of-freedom parallel robot with an intuitive geometric structure optimized for the workspace required for lower limb diagnosis. The solutions of the forward/inverse kinematic model are simplified by decomposing MedRUE into the mobile base, two five-bar mechanisms and the tool part. Most singularity cases of MedRUE are unreachable due to its mechanical joint limits. The hardware setup of MedRUE was also introduced. MedRUE is easy to install, and can be controlled directly by personal computer via a peripheral component interconnect (PCI) card.

The calibration method of MedRUE is based on a direct measurement method. It is simple and practical to implement without advanced calibration knowledge. A laser tracker is used for measurement due to its superior accuracy over optical measurement methods. Certain points on the robot's links are measured in the predefined robot trajectory. The measured position data determine the coordinates of the joints, and thereafter identify the kinematic parameters. The proposed method determines the parameters individually, and thereafter decouples the nonlinear interference between kinematic parameters. As opposed to most calibration methods based on optimization techniques, all kinematic parameters are identified as a bound solution.

Force control is a major concern in human-robot interaction systems. The force control of MedRUE is designed considering human as a variable environment. An admittance control

with variable parameters, therefore, is applied in the force controller. The variation law of the admittance parameters is built upon an operator intention indicator, which uses sensor data to predict the operator's wish to accelerate or decelerate. The admittance parameters are modified to facilitate the operator's movements. A novel implementation of the passivity theory was proposed for the variable admittance control to ensure the passivity property of the admittance model.

This research accomplishes the first stages of the MedRUE system. It can be used as an ultrasound probe holder to assist the sonographer in peripheral arterial disease diagnosis in the lower limbs. The robot can place the probe in the desired position either by a reference position command or the guide of the sonographer's hand. The robot releases the sonographer from the weight load of the ultrasound probe, and can provide accurate position information paired with medical images. There are many tasks to achieve in the future work of following stages. Image-based control can be implemented in parallel with force control, to provide the solution of a fully-automated ultrasound scan for peripheral arterial disease diagnosis in the lower limbs. Computer vision technologies will be required to extract boundary features and the geometric center of the artery. The scanned artery can then be reconstructed via the medical images and the corresponding position data, and the reconstruction will be invaluable for further treatment.

This project is the initial study of a medical ultrasound robot for the diagnosis of peripheral arterial disease in the lower limbs. Compared to other medical imaging technologies, such as CT and MRI, it has the advantages of low cost and non-radiation. These are very valuable features in the daily diagnosis of peripheral arterial disease given its high prevalence. In sum, MedRUE is outstanding for the application of ultrasound scanning in the lower limbs, and it can be used for ultrasound scans of other areas as well. It aims to meet the need of sonographers and patients, and benefits both with improved health.

APPENDIX I

MOTION CONTROLLER DESIGN OF MEDRUE

The design of the MedRUE's motion controller is based on the MedRUE's dynamic model, which can be represented in joint level as

$$\boldsymbol{\tau} = \mathbf{M}(\mathbf{q})\ddot{\mathbf{q}} + \mathbf{V}(\mathbf{q},\dot{\mathbf{q}}) + \mathbf{F}(\dot{\mathbf{q}}) + \mathbf{G}(\mathbf{q}) \tag{I.1}$$

where $\mathbf{q}$ is the vector of joint values, $\boldsymbol{\tau}$ is the vector of torques in active joints, $\mathbf{M}$ is the inertia matrix, matrix $\mathbf{V}$ contains Coriolis and centrifugal force terms, $\mathbf{F}$ represents the frictions in joints, and $\mathbf{G}$ includes the gravity terms. In the motor lever, the dynamic model is written as

$$\boldsymbol{\tau}_m = \mathbf{I}_m\ddot{\mathbf{q}}_m + \mathbf{F}_m(\dot{\mathbf{q}}_m) + \mathbf{K}_r\boldsymbol{\tau} \tag{I.2}$$

where $\mathbf{q}_m$ is vector of rotation angle of motors, $\boldsymbol{\tau}_m$ is the vector of torques in each motor, $\mathbf{I}_m$ is the inertia of motors, $\mathbf{F}_m$ represents the friction in the motors, and $\mathbf{K}r$ includes the gear ratios between motors and joints. The inertia matrix $\mathbf{M}$ is decomposed in to the format as follows :

$$\mathbf{M}(\mathbf{q}) = \bar{\mathbf{M}} + \Delta\mathbf{M}(\mathbf{q}) \tag{I.3}$$

where $\bar{\mathbf{M}}$ is the mean values of inertia matrix $\mathbf{M}$, and $\Delta\mathbf{M}$ is the residue term (Yen, 2011).

Substituing $\boldsymbol{\tau}$ in (I.2) with (I.1) leads to

$$\boldsymbol{\tau}_m = \bar{\mathbf{M}}_m\ddot{\mathbf{q}}_m + \mathbf{F}_c\,\mathrm{sgn}(\dot{\mathbf{q}}_m) + \mathbf{G}_m(\mathbf{q}_m) + \mathbf{d}_m \tag{I.4}$$

where $\bar{\mathbf{M}}_m = \mathbf{I}_m + \mathbf{K}_r^{-1}\bar{\mathbf{M}}\mathbf{K}_r^{-1}$, $\mathbf{F}_c$ is the Coulomb friction coefficient involving both motors and joints, $\mathbf{G}_m$ is the mapping of gravity matrix $\mathbf{G}$ from joint lever to motor lever, and $\mathbf{d}_m = \mathbf{K}_r^{-1}\Delta\mathbf{M}(\mathbf{q})\mathbf{K}_r^{-1}\ddot{\mathbf{q}}_m + \mathbf{K}_r^{-1}\mathbf{V}(\mathbf{q},\dot{\mathbf{q}})$. Since during the application of MedRUE, the robot speed is slow, the nonlinear term $\mathbf{d}_m$ is considered as the disturbance of robot system.

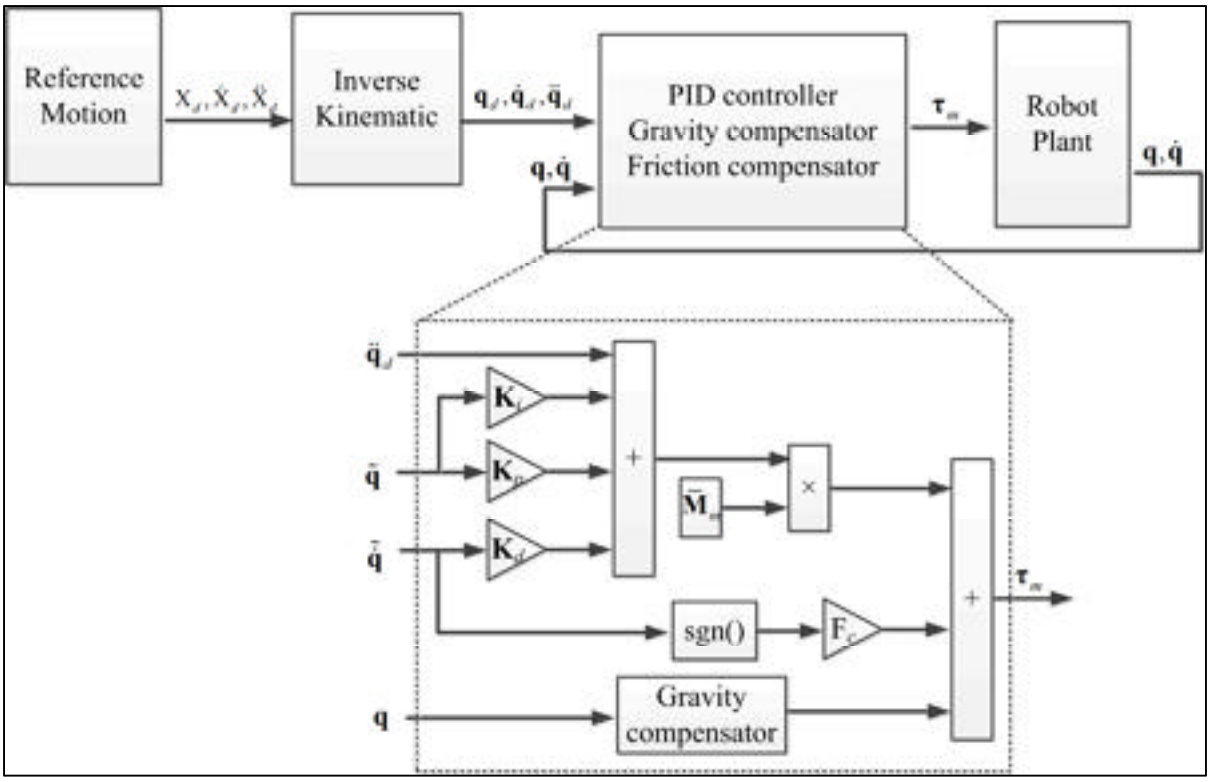

Figure I.1 Motion controller of MedRUE

According to dynamic model in (I.4), the motion controller of MedRUE is designed with PID controller, friction compensator and gravity compensator. As shown in Figure I.1, given the desired motion in Cartesian space (i.e. acceleration $\ddot{\mathbf{X}}_d$, velocity $\dot{\mathbf{X}}_d$ and position $\mathbf{X}_d$), the inverse kinematic model provides desired motion in joint space. In PID controller, $\tilde{\mathbf{q}} = \mathbf{q}_d - \mathbf{q}$ represents the joint errors (gear ratio $\mathbf{K}_r$ is ignored in the diagram). The PID coefficient matrix $\mathbf{K}_i$, $\mathbf{K}_p$ and $\mathbf{K}_d$ are designed according to (Bigras, 2009). The Coulomb friction coefficient $\mathbf{F}_c$ is measured directly on the joint with a weight balance. The design of gravity compensator has been studied in (Lessard, 2007).

LIST OF REFERENCES

Abolmasesumi, Purang, Septimiu E. Salcudean, Wen Hong Zhu, Mohammad Reza Sirouspour and Simon P. DiMaio. 2002. " Image-guided control of a robot for medical ultrasound ". *IEEE Transactions on Robotics and Automation,* vol. 18, n^{o} 1, p. 11-23.

Albu-Schäffer, Alin, Christian Ott and Gerd Hirzinger. 2007. " A Unified Passivity-based Control Framework for Position, Torque and Impedance Control of Flexible Joint Robots ". *The International Journal of Robotics Research,* vol. 26, n^{o} 1, p. 23-39.

Arbeille, Philippe, GERARD POISSON, Pierre Vieyres, Jean Ayoub, Maryannick Porcher and Jean Louis Boulay. 2003. " Echographic examination in Isolated Sites Controlled from an Expert Center Using a 2-D Echograph Guided by a Teleoperated Robotic Arm ". *Ultrasound in Medicine and Biology,* vol. 29, n^{o} 7, p. 993-1000.

Augugliaro, Federico, and Raffaello D'Andrea. 2013. " Admittance control for physical human-quadrocopter interaction ". In *Control Conference (ECC), 2013 European*. p. 1805-1810. IEEE.

Baharin, I. B., and M. M. Hasan. 1994. " Identification of manipulator kinematics parameters through iterative method ". In *Systems, Man, and Cybernetics, 1994. Humans, Information and Technology., 1994 IEEE International Conference on*. (2-5 Oct 1994) Vol. 2, p. 1263-1268 vol.2.

Bai, Ying, Hanqi Zhuang and Zvi S Roth. 2003. " Experiment study of PUMA robot calibration using a laser tracking system ". In *Soft Computing in Industrial Applications, 2003. SMCia/03. Proceedings of the 2003 IEEE International Workshop on*. p. 139-144. IEEE.

Bao, Jie, and Peter L. Lee. 2007. *Process Control: The Passive Systems Approach*. Springer, 253 p.

Barati, M, AR Khoogar and M Nasirian. 2011. " Estimation and Calibration of Robot Link Parameters with Intelligent Techniques ". *Iranian Journal of Electrical and Electronic Engineering,* vol. 7, n^{o} 4, p. 225-234.

Bennett, David J, and John M Hollerbach. 1991. " Autonomous calibration of single-loop closed kinematic chains formed by manipulators with passive endpoint constraints ". *Robotics and Automation, IEEE Transactions on,* vol. 7, n^{o} 5, p. 597-606.

Berghuis, H., and H. Nijmeijer. 1993. " A passivity approach to controller-observer design for robots ". *Robotics and Automation, IEEE Transactions on,* vol. 9, n^{o} 6, p. 740-754.

Bigras, Pascal. 2009. “Commande des robots”. <https://cours.etsmtl.ca/sys827/Documents/Transparents/chap6_fp.pdf> Retrieved on Sep.1, 2015.

British Columbia Ultrasonographer's Society, Healthcare Benefit Trust and Health Sciences Association. 1996. *Sonographer's work, health & disability surver*.

Buchli, J., F. Stulp, E. Theodorou and S. Schaal. 2011. “ Learning variable impedance control ”. *International Journal of Robotics Research,* vol. 30, n° 7, p. 820-833.

Byrnes, C. I., A. Isidori and J. C. Willems. 1991. “ Passivity, feedback equivalence, and the global stabilization of minimum phase nonlinear systems ”. *Automatic Control, IEEE Transactions on,* vol. 36, n° 11, p. 1228-1240.

Canudas-de-Wit, Carlos, and Rafael Kelly. 2007. “ Passivity analysis of a motion control for robot manipulators with dynamic friction ”. *Asian Journal of Control,* vol. 9, n° 1, p. 30-36.

Chan, Danny, Matthew E. Anderson and Bart L. Dolmatch. 2010. “ Imaging Evaluation of Lower Extremity Infrainguinal Disease: Role of the Noninvasive Vascular Laboratory, Computed Tomography Angiography, and Magnetic Resonance Angiography ”. *Techniques in Vascular and Interventional Radiology,* vol. 13, n° 1, p. 11-22.

Chan, SP, Bin Yao, WB Gao and M Cheng. 1991. “ Robust impedance control of robot manipulators ”. *International Journal of Robotics & Automation,* vol. 6, n° 4, p. 220-227.

Chien, Ming-Chih, and An-Chyau Huang. 2004. “ Adaptive Impedance Control of Robot Manipulators based on Function Approximation Technique ”. *Robotica,* vol. 22, n° 04, p. 395-403.

Conti, François, Jaeheung Park and Oussama Khatib. 2014. “ Interface Design and Control Strategies for a Robot Assisted Ultrasonic Examination System ”. In *Experimental Robotics*, sous la dir. de Khatib, Oussama, Vijay Kumar and Gaurav Sukhatme. Vol. 79, p. 97-113.

Cortesao, R., C. Sousa and P. Queiros. 2010. “ Active Impedance Control Design for Human-Robot Comanipulation ”. *2010 American Control Conference*, p. 2805-2810.

Courreges, Fabien, Pierre Vieyres and Robert Istepanian. 2004. “ Advances in Robotic Tele-Echography Services - The OTELO System ”. In *Proceedings of the 26th Annual International Conference of the IEEE/EMBS*. (San Francisco, CA, USA, September 1-5), p. 5371-5374.

Craig, John J. 2004. *Introduction to Robotics: Mechanics and Control*, 3rd. Upper Saddle River, New Jersey: Prentice Hall, 408 p.

Craig, Marveen. 1985. " Sonography: An occupational health hazard ". *Journal of Diagnostic Medical Sonography*, p. 1:121-124.

Criqui, Michael H., Arnost Fronek, Elizabeth Barrett-Connor, Melville R. Klauber, Sam Gabriel and Deborah Goodman. 1985. " The prevalence of peripheral arterial disease in a defined population". *Circulation,* vol. 71, p. 510.

Criqui, Michael H., R. D. Langer and Arnost Fronek. 1992. " Mortality over a period of 10 years in patients with peripheral arterial disease ". *Survey of Anesthesiology,* vol. 36, n° 5, p. 304.

Ma, Song. D. 1996. " A self-calibration technique for active vision systems ". *Robotics and Automation, IEEE Transactions on,* vol. 12, n° 1, p. 114-120.

de Queiroz, Marcio S. 2000. *Lyapunov-based control of mechanical systems*. Springer Science & Business Media.

Deep, Kusum, Madhuri Arya, Manoj Thakur and Balasubrmanian Raman. 2013. " Stereo camera calibration using particle swarm optimization ". *Applied Artificial Intelligence,* vol. 27, n° 7, p. 618-634.

Delgorge, Cécile, Fabien Courrèges, Lama Al Bassit, Cyril Novales, Christophe Rosenberger, Natalie Smith-Guerin, Concepció Brù, Rosa Gilabert, Maurizio Vannoni, Gérard Poisson and Pierre Vieyres. 2005. " A Tele-Operated Mobile Ultrasound Scanner Using a Light-Weight Robot ". *IEEE Transactions on information technology in biomedicine,* vol. 9, n° 1, p. 50-58.

Denavit, Jacques. 1955. " A kinematic notation for lower-pair mechanisms based on matrices ". *Trans. of the ASME. Journal of Applied Mechanics,* vol. 22, p. 215-221.

Diehm, Curt, Alexander Schuster, Jens R. Allenberg, Harald Darius, Roman Haberl, Stefan Lange, David Pittrow, Berndt von Stritzky, Gerhart Tepohl and Hans-Joachim Trampisch. 2004. " High prevalence of peripheral arterial disease and co-morbidity in 6880 primary care patients: cross-sectional study ". *Atherosclerosis,* vol. 172, n° 1, p. 95-105.

Dong, X. X., G. Li, G. F. Liu and J. Zhao. 2013. " Cartesian Impedance Control for Space Robotic Arm Based on End Force/Torque Sensor ". *Materials, Mechanical Engineering and Manufacture, Pts 1-3,* vol. 268-270, p. 1531-1537.

Dormandy, John A., and Robert B. Rutherford. 2000. " Management of peripheral arterial disease(PAD) ". *Journal of Vascular Surgery,* vol. 31, n° 1, p. S1-S296.

Doulgeri, Zoe, Nikolaos Fahantidis and Richard P Paul. 1998. " Kinematic stability of hybrid position/force control for robots ". In *Intelligent Robots and Systems, 1998. Proceedings., 1998 IEEE/RSJ International Conference on*. Vol. 2, p. 1138-1144. IEEE.

Driels, Morris R, Lt W Swayze and Lt S Potter. 1993. " Full-pose calibration of a robot manipulator using a coordinate-measuring machine ". *The International Journal of Advanced Manufacturing Technology,* vol. 8, n° 1, p. 34-41.

Duchaine, Vincent, and C. M. Gosselin. 2007. " General Model of Human-Robot Cooperation Using a Novel Velocity Based Variable Impedance Control ". In *EuroHaptics Conference, 2007 and Symposium on Haptic Interfaces for Virtual Environment and Teleoperator Systems. World Haptics 2007. Second Joint*. (22-24 March 2007), p. 446-451.

Duchaine, Vincent, and C. M. Gosselin. 2008. " Investigation of human-robot interaction stability using Lyapunov theory ". In *Robotics and Automation, 2008. ICRA 2008. IEEE International Conference on*. (19-23 May 2008), p. 2189-2194.

Duchaine, Vincent, B. Mayer St.-Onge, Gao Dalong and Clement Gosselin. 2012. " Stable and Intuitive Control of an Intelligent Assist Device ". *Haptics, IEEE Transactions on,* vol. 5, n° 2, p. 148-159.

Eppinger, S. D., and W. P. Seering. 1987. " Understanding bandwidth limitations in robot force control ". In *Robotics and Automation. Proceedings. 1987 IEEE International Conference on*. (Mar 1987) Vol. 4, p. 904-909.

Eppinger, S. D., and W. P. Seering. 1989. " Three dynamic problems in robot force control ". In *Robotics and Automation, 1989. Proceedings., 1989 IEEE International Conference on*. (14-19 May 1989), p. 392-397 vol.1.

Evans, Kevin, Shawn Roll and Joan Baker. 2009. " Work-related musculoskeletal disorders (WRMSD) among registered diagnostic medical sonographers and vascular technologists: a representative sample ". *Journal of Diagnostic Medical Sonography,* vol. 25, n° 6, p. 287-299.

Fisher, William D, and M Shahid Mujtaba. 1992. " Hybrid position/force control: a correct formulation ". *The International Journal of Robotics Research,* vol. 11, n° 4, p. 299-311.

Fixel, Peter. 2006. *Absolute Accuracy Marketing Presentation*. ABB Automation Technologies AB.

Fowkes, F. Gerald R., Diana Rudan, Igor Rudan, Victor Aboyans, Julie O. Denenberg, Mary M. McDermott, Paul E. Norman, Uchechukwe K. A. Sampson, Linda J. Williams, George A. Mensah and Michael H. Criqui. 2013. " Comparison of global estimates of prevalence and risk factors for peripheral artery disease in 2000 and 2010: a systematic review and analysis ". *The Lancet,* vol. 382, n° 9901, p. 1329-1340.

Gandhi, Sanjay, Ido Weinberg, Ronan Margey and Michael Jaff. 2011. " Comprehensive medical management of peripheral arterial disease ". *Progress in cardiovascular diseases,* vol. 54, n° 1, p. 2-13.

Gomi, H., Y. Koike and M. Kawato. 1992. " Human hand stiffness during discrete point-to-point multi-joint movement ". In *Engineering in Medicine and Biology Society, 14th International Conference of the IEEE*. (Oct. 29 1992-Nov. 1 1992). Vol. 4, p. 1628-1629.

Gonzales, Adriana Vilchis, Philippe Cinquin, Jocelyne Troccaz, Agnès Guerraz, Bernard Hennion, Franck Pellissier, Pierre Thorel, Fabien Courreges, Alain Gourdon, Gérard Poisson, Pierre Vieyres, Pierre Caron, Olivier Mérigeaux, Loïc Urbain, Cédric Daimo, Stéphane Lavallée, Philippe Arbeille, Marc Althuser, Jean-Marc Ayoubi, Bertrand Tondu and Serge Ippolito. 2001. " TER: A system for robotic tele-echography ". *Medical Image Computing and Computer-Assisted Intervention,* vol. 2208, p. 326-334.

Gornik, Heather L., and Joshua A. Beckman. 2005. " Peripheral Arterial Disease ". *Circulation,* vol. 111, n° 13, p. e169-e172.

Gosline, A. H. C., and V. Hayward. 2007. " Time-Domain Passivity Control of Haptic Interfaces with Tunable Damping Hardware ". In *EuroHaptics Conference, 2007 and Symposium on Haptic Interfaces for Virtual Environment and Teleoperator Systems. World Haptics 2007. Second Joint*. (22-24 March 2007), p. 164-179.

Gourdon, Alain, Philippe Poignet, Gerard Poisson, Pierre Vieyres and Pierre Marche. 1999. " A new robotic mechanism for medical application ". In *Proc. IEEE/ASME Internaitnal Conterence on Advanced Intelligent Mechatronics*. (Atlanta, USA, September 19-23), p. 33-38.

Guillaume, P., and R. Pintelon. 1996. " A Gauss-Newton-like optimization algorithm for “weighted” nonlinear least-squares problems ". *Signal Processing, IEEE Transactions on,* vol. 44, n° 9, p. 2222-2228.

Hace, A., K. Jezernik and S. Uran. 1996. " Robust impedance control ". *Proceedings of the 1998 Ieee International Conference on Control Applications, Vols 1 and 2*, p. 583-587.

Hannaford, B., and Ryu Jee-Hwan. 2002. “ Time-domain passivity control of haptic interfaces ”. *Robotics and Automation, IEEE Transactions on,* vol. 18, n° 1, p. 1-10.

Hanqi, Zhuang. 1997. “ Self-calibration of parallel mechanisms with a case study on Stewart platforms ”. *Robotics and Automation, IEEE Transactions on,* vol. 13, n° 3, p. 387-397.

Hayward, V., and K. E. MacLean. 2007. “ Do it yourself haptics: Part I ”. *IEEE Robotics & Automation Magazine,* vol. 14, n° 4, p. 88-104.

Hirsch, Alan T., Michael H. Criqui and Mark A. Creager. 2001. “ Peripheral Arterial Disease Detection,Awareness, and Treatment in Primary Care ”. *American Medical Association,* vol. 286, p. 1317.

Ikeura, Ryojun, and Hikaru Inooka. 1995. “ Variable impedance control of a robot for cooperation with a human ”. In *Robotics and Automation, 1995. Proceedings., 1995 IEEE International Conference on*. (21-27 May 1995). Vol. 3, p. 3097-3102 vol.3.

Ikeura, Ryojun, H. Monden and Hikaru Inooka. 1994. “ Cooperative motion control of a robot and a human ”. In *Robot and Human Communication, 1994. RO-MAN '94 Nagoya, Proceedings., 3rd IEEE International Workshop on*. (18-20 Jul 1994), p. 112-117.

ISO-9283. 1998. *manipulating industrial robots -- Performance criteria and related test methods*. Geneva, Switzerland: International Organization for Standardization.

Janvier, Marie-Ange, Louis-Gilles Durand, Marie-Hélène Roy Gardinal, Isabelle Renaud, Boris Chayer, Pascal Bigras, Jacques De Guise, Gilles Soulez and Guy Cloutier. 2008. “ Performance evaluation of a medical robotic 3D-ultrasound imaging system ”. *Medical Imaging Analysis,* vol. 12, p. 275.

Janvier, Marie-Ange, Gilles Soulez, Louise Allard and Guy Cloutier. 2010. “ Validation of 3D reconstructions of a mimicked femoral artery with an ultrasound imaging robotic system ”. *Medical physics,* vol. 37, n° 7, p. 3868-3879.

Jee-Hwan, Ryu, Kwon Dong-Soo and B. Hannaford. 2004. “ Stability guaranteed control: time domain passivity approach ”. *Control Systems Technology, IEEE Transactions on,* vol. 12, n° 6, p. 860-868.

Jee-Hwan, Ryu, C. Preusche, B. Hannaford and G. Hirzinger. 2005. “ Time domain passivity control with reference energy following ”. *Control Systems Technology, IEEE Transactions on,* vol. 13, n° 5, p. 737-742.

Joubair, Ahmed, and Ilian A. Bonev. 2013. “ Comparison of the efficiency of five observability indices for robot calibration ”. *Mechanism and Machine Theory,* vol. 70, p. 254-265.

Joubair, Ahmed, Mohamed Slamani and Ilian A. Bonev. 2012a. “ Kinematic calibration of a 3 - DOF planar parallel robot ”. *Industrial Robot: An International Journal,* vol. 39, n° 4, p. 392-400.

Joubair, Ahmed, Mohamed Slamani and Ilian A. Bonev. 2012b. “ A novel XY-Theta precision table and a geometric procedure for its kinematic calibration ”. *Robotics and Computer-Integrated Manufacturing,* vol. 28, n° 1, p. 57-65.

Joubair, Ahmed, Long-Fei Zhao, Pascal Bigras, Ilian A Bonev and Clive Loughlin. 2015. “ Absolute accuracy analysis and improvement of a hybrid 6-DOF medical robot ”. *Industrial Robot: An International Journal,* vol. 42, n° 1.

Judd, Robert P, and Al B Knasinski. 1990. “ A technique to calibrate industrial robots with experimental verification ”. *Robotics and Automation, IEEE Transactions on,* vol. 6, n° 1, p. 20-30.

Kawai, Hiroyuki, Toshiyuki Murao, Ryuichi Sato and Masayuki Fujita. 2011. “ Passivity-based control for 2DOF robot manipulators with antagonistic bi-articular muscles ”. *Canadian Communication Association, Proceeding of* p. 1451-1456.

Khalil, Wisama, and Etienne Dombre. 2004. *Modeling, identification and control of robots*. Butterworth-Heinemann.

Khatib, O. 1987. “ A unified approach for motion and force control of robot manipulators: The operational space formulation ”. *Robotics and Automation, IEEE Journal of,* vol. 3, n° 1, p. 43-53.

Kim, C., D. Chang, D. Petrisor, G. Chirikjian, M. Han and D. Stoianovici. 2013. “ Ultrasound Probe and Needle-Guide Calibration for Robotic Ultrasound Scanning and Needle Targeting ”. *Ieee Transactions on Biomedical Engineering,* vol. 60, n° 6, p. 1728-1734.

Kirchner, H.O.K., B. Gurumoorthy and F.B. Prinz. 1987. “ A perturbation approach to robot calibration ”. *The International Journal of Robotics Research,* vol. 6, n° 4, p. 47-59.

Klodmann, Julian, R. Konietschke, A. Albu-Schaffer and Gerhard Hirzinger. 2011. “ Static calibration of the DLR medical robot MIRO, a flexible lightweight robot with integrated torque sensors ”. In *Intelligent Robots and Systems (IROS), 2011 IEEE/RSJ International Conference on*. (25-30 Sept. 2011), p. 3708-3715.

Koizumi, Norihiro, Shin'ichi Warisawa, Hiroyuki Hashizume and Mamoru Mitsuishi. 2008. “ Continuous path controller for the remote ultrasound diagnostic system ”. *IEEE/ASME Transactions on Mechatronics,* vol. 13, n° 2, p. 206-218.

Kurfess, Thomas R. 2005. *Robotics and automation handbook*. CRC press.

Lau, Joseph, David Kent, Athina Tatsioni, Yannan Sun, Chenchen Wang, Priscilla Chew, Bruce Kupelnick and Harmon Jordan. 2004. “ Vulnerable Plaques: A Brief Review of the Concept and Proposed Approaches to Diagnosis and Treatment ”. *Agency for Healthcare Research and Quality*.

Lawrence, D. A. 1988. “ Impedance control stability properties in common implementations ”. In *Robotics and Automation, 1988. Proceedings., 1988 IEEE International Conference on*. (24-29 Apr 1988) Vol. 2, p. 1185-1190.

Lecours, Alexandre, Boris Mayer-St-Onge and Clément Gosselin. 2012. “ Variable admittance control of a four-degree-of-freedom intelligent assist device ”. In *IEEE International Conference on Robotics and Automation*. (RiverCentre, Saint Paul, Minnesota,USA, May 14-18), p. 3903-3908.

Lee, Bum-Joo. 2013. “ Geometrical Derivation of Differential Kinematics to Calibrate Model Parameters of Flexible Manipulator ”. *International Journal of Advanced Robotic Systems,* vol. 10, n° 106.

Lei, Sun, Liu Jingtai, Sun Weiwei, Wu Shuihua and Huang Xingbo. 2004. “ Geometry-based robot calibration method ”. In *Robotics and Automation, 2004. Proceedings. ICRA'04. 2004 IEEE International Conference on*. Vol. 2, p. 1907-1912. IEEE.

Lessard, Simon. 2008. “ Conception d'un système robotique sécuritaire pour la prise d'images échographiques ”. Montréal, École de technologie supérieure, 171 p.

Lessard, Simon, Pascal Bigras and Ilian A. Bonev. 2007. “ A New Medical Parallel Robot and Its Static Balancing Optimization ”. *Journal of Medical Devices,* vol. 1, n° 4, p. 272-278.

Socovar, Societe En Commandite (Montreal, CA). 2010. *Parallel Manipulator*. 7673537.

Li, Changsheng, Tianmiao Wang, Lei Hu, Lihai Zhang, Hailong Du, Lifeng Wang, Sheng Luan and Peifu Tang. 2014. “ Accuracy Analysis of a Robot System for Closed Diaphyseal Fracture Reduction ”. *International Journal of Advanced Robotic Systems,* vol. 11, n° 169.

Li, Yanan, Shuzhi Sam Ge, Qun Zhang and Tong Heng Lee. 2013. “ Neural networks impedance control of robots interacting with environments ”. *IET Control Theory & Applications*. Vol. 7, n° 11, p. 1509-1519.

Linde, R.Q. van der, and P. Lammertse. 2003. " HapticMaster – a generic force controlled robot for human interaction ". *Industrial Robot: An International Journal,* vol. 30, n° 6, p. 515-524.

Lindseth, Frank, Geir Arne Tangen, Thomas Langø and Jon Bang. 2003. " Probe calibration for freehand 3-D ultrasound ". *Ultrasound in Medicine & Biology,* vol. 29, n° 11, p. 1607-1623.

Lyapunov, Aleksandr Mikhailovich. 1992. " The general problem of the stability of motion ". *International Journal of Control,* vol. 55, n° 3, p. 531-534.

Maclean, K. E., and V. Hayward. 2008. " Do it yourself haptics: Part II - Interaction design ". *Ieee Robotics & Automation Magazine,* vol. 15, n° 1, p. 104-119.

Martinelli, Thomas, Jean-Luc Bosson, Luc Bressollette, Franck Pelissier, Eric Boidard, Jocelyne Troccaz and Philippe Cinquin. 2007. " Robot-based tele-echography: clinical evaluation of the TER system in abdominal aortic exploration ". *Ultrasound in Medicine,* vol. 26, n° 11, p. 1611-1616.

Masuda, Kohji, Eizen Kimura, Norihiko Tateishi and Ken Ishhara. 2001a. " Three dimensional motion mechanism of ultrasound probe and its application for tele-echography system ". In *IEEE/RSJ International Conference on Intelligent Robots and Systems*. (Maui, Hawaii, USA, 29 Oct 2001-03 Nov 2001) Vol. 2, p. 1112-1116.

Masuda, Kohji, Eizen Kimura, Norihiko Tateishi and Ken Ishihara. 2001b. " Construction of 3D Movable Echographic Diagnosis Robot and Remote Diagnosis via Fast Digital Network ". In *23rd Annual International Conference of the IEEE Engineering in Medicine and Biology Society*. (Istanbul, Turkey, October 25) Vol. 4, p. 3634-3637.

Masuda, Kohji, Eizen Kimura, Norihiko Tateishi, Yasuyuki Suzuki and Ken Ishihara. 2002. " Robotic Tele-diagnosis System of echography and Wireless Experiment for Mobile Telemedicine ". In *Proceedings of the Second Joint EMBS/BMES Conference*. (Houston, Texas, USA, October 23), p. 1855-1856.

Maurine, Patrick, and Etienne Dombre. 1996. " A calibration procedure for the parallel robot Delta 4 ". In *Robotics and Automation, IEEE International Conference on*. (Minneapolis, MN 22-28 Apr 1996). Vol. 2, p. 975-980.

Maye, J., P. Furgale and R. Siegwart. 2013. " Self-supervised calibration for robotic systems ". In *Intelligent Vehicles Symposium (IV), 2013 IEEE*. (23-26 June 2013), p. 473-480.

Mercier, Laurence, Thomas Langø, Frank Lindseth and Louis D. Collins. 2005. " A review of calibration techniques for freehand 3-D ultrasound systems ". *Ultrasound in Medicine & Biology,* vol. 31, n° 2, p. 143-165.

Minar, E. 2009. " Critical limb ischaemia ". *Hämostaseologie,* vol. 29, n° 1, p. 102-109.

Mirman, C. R., and K. C. Gupta. 1992. " Compensation of Robot joint variables using special Jacobian matrices ". *Journal of Robotic Systems,* vol. 9, n° 1, p. 113-137.

Mohler, Emile R. 2003. " Peripheral Arterial Disease Indentification and Implications ". *American Medical Association,* vol. 163, p. 2306.

Mooring, Benjamin W., Morris R. Driels and Zvi S. Roth (135-140). 1991. *Fundamentals of Manipulator Calibration*. John Wiley & Sons, NY, 329 p.

Nahvi, A., J. M. Hollerbach and V. Hayward. 1994a. " Calibration of a parallel robot using multiple kinematic closed loops ". In *Robotics and Automation, 1994. Proceedings., 1994 IEEE International Conference on*. (8-13 May 1994), p. 407-412 vol.1.

Nahvi, Ali, John M. Hollerbach and Vincent Hayward. 1994b. " Calibration of a parallel robot using multiple kinematic closed loops ". In *Robotics and Automation, IEEE International Conference on*. (San Diego, CA 8-13 May 1994). Vol. 1, p. 407-412.

Nakadate, R., H. Uda, H. Hirano, J. Solis, A. Takanishi, E. Minagawa, M. Sugawara and K. Niki. 2009. " Development of a robotic carotid blood measurement WTA-1RII: Mechanical improvement of gravity compensation mechanism and optimal link position of the parallel manipulator based on GA ". In *Advanced Intelligent Mechatronics, 2009. AIM 2009. IEEE/ASME International Conference on*. (14-17 July 2009), p. 717-722.

Nakadate, Ryu, Jorge Solis, Atsuo Takanishi, Motoaki Sugawara, Kiyomi Niki and Eiichi Minagawa. 2010. " Development of the Ultrasound Probe Holding Robot WTA-1RII and an Automated Scanning Algorithm based on Ultrasound Image Feedback ". In *ROMANSY 18 Robot Design, Dynamics and Control*, sous la dir. de Castelli, Vincenzo Parenti, and Werner Schiehlen. Vol. 524, p. 359-366.

Nelson, Thomas R., Amy Tran, Hourieh Fakourfar and Jakob Nebeker. 2012. " Positional Calibration of an Ultrasound Image-Guided Robotic Breast Biopsy System ". *Journal of Ultrasound in Medicine,* vol. 31, n° 3, p. 351-359.

Newman, Wyatt S, and Yuandao Zhang. 1994. " Stable interaction control and coulomb friction compensation using natural admittance control ". *Journal of Robotic Systems,* vol. 11, n° 1, p. 3-11.

Norgren, Lars, William R. Hiatt, John A. Dormandy, Mark R. Nehler, Kenneth A. Harris and Gerry R. Fowkes. 2007. " Inter-Society Consensus for the Management of Peripheral Arterial Disease ". *Journal of Vascular SURGERY* vol. 45, n° 1, p. S5-S67.

Ogata, Katsuhiko. 1997. *Modern Control Engineering*, 3 rd. New Jersey: Tom Robbins.

Onogi, Shinya, Yasuhiro Urayama, Sachie Irisawa and Kohji Masuda. 2013. " Robotic ultrasound probe handling auxiliary by active compliance control ". *Advanced Robotics,* vol. 27, n° 7, p. 503-512.

Ott, C., A. Albu-Schaffer, A. Kugi and G. Hirzinger. 2008. " On the passivity-based impedance control of flexible joint robots ". *Ieee Transactions on Robotics,* vol. 24, n° 2, p. 416-429.

Ott, C., A. Kugi and Y. Nakamura. 2008. " Resolving the problem of non-integrability of nullspace velocities for compliance control of redundant manipulators by using semi-definite Lyapunov functions ". In *Robotics and Automation, 2008. ICRA 2008. IEEE International Conference on*. (19-23 May 2008), p. 1999-2004.

Ott, Christian, Ranjan Mukherjee and Yoshihiko Nakamura. 2010. " Unified Impedance and Admittance Control ". *2010 Ieee International Conference on Robotics and Automation (Icra)*, p. 554-561.

Ouriel, Kenneth. 2001. " Peripheral arterial disease ". *The Lancet,* vol. 358, n° 9289, p. 1257-1264.

Park, Heon, and JangMyung Lee. 2004. " Adaptive impedance control of a haptic interface ". *Mechatronics,* vol. 14, n° 3, p. 237-253.

Pierrot, François, Etienne Dombre, Eric Dégoulange, Loïc Urbain, Pierre Caron, Jérome Gariépy and Jean-Louis Mégnien. 1999. " Hippocrate: a safe robot arm for medical applications with force feedback ". *Medical Image Analysis,* vol. 3, n° 3, p. 285-300.

Powell, Michael JD. 1964. " An efficient method for finding the minimum of a function of several variables without calculating derivatives ". *The computer journal,* vol. 7, n° 2, p. 155-162.

Priester, A. M., S. Natarajan and M. O. Culjat. 2013. " Robotic ultrasound systems in medicine ". *Ultrasonics, Ferroelectrics, and Frequency Control, IEEE Transactions on,* vol. 60, n° 3, p. 507-523.

Rahman, M. M., R. Ikeura and K. Mizutani. 1999. " Investigating the impedance characteristic of human arm for development of robots to co-operate with human operators ". In *Systems, Man, and Cybernetics, 1999. IEEE SMC '99 Conference Proceedings. 1999 IEEE International Conference on*. (1999) Vol. 2, p. 676-681 vol.2.

Raibert, Marc H, and John J Craig. 1981. " Hybrid position/force control of manipulators ". *Journal of Dynamic Systems, Measurement, and Control,* vol. 103, n° 2, p. 126-133.

Ren, Xiao-Dong, Zu-Ren Feng and Cheng-Ping Su. 2009. " A new calibration method for parallel kinematics machine tools using orientation constraint ". *International Journal of Machine Tools and Manufacture,* vol. 49, n° 9, p. 708-721.

Renders, J. M., E. Rossignol, M. Becquet and R. Hanus. 1991. " Kinematic calibration and geometrical parameter identification for robots ". *Robotics and Automation, IEEE Transactions on,* vol. 7, n° 6, p. 721-732.

Roning, Juha, and Alexander Korzun. 1997. " A method for industrial robot calibration ". In *Robotics and Automation, IEEE International Conference on*. (Albuquerque, NM, 20-25 Apr 1997) Vol. 4, p. 3184-3190.

Ryu, Jee-Hwan, Dong-Soo Kwon and Blake Hannaford. 2004. " Stable teleoperation with time-domain passivity control ". *Robotics and Automation, IEEE Transactions on,* vol. 20, n° 2, p. 365-373.

Salcudean, Septimiu E., Gordon Bell, Simon Bachmann, Wen Hong Zhu, Purang Abolmasesumi and Peter D.Lawrence. 1999a. " Robot-assisited diagnositic ultrasound-Design and feasibility experiments ". *Medical Image Computing and Computer Assisted Intervention*, p. 1062.

Salcudean, Septimiu E., Wen Hong Zhu, Purang Abolmasesumi, Simon Bachmann and Peter D.Lawrence. 1999b. " A robot system for medical ultrasound ". In *Robotics research International Symposium*. (Snowbird, Utah, USA, October 9-12, 1999). Vol. 9, p. 195-202.

Schirmang, Todd C, Sun H Ahn, Timothy P Murphy, Gregory J Dubel and Gregory M Soares. 2009. " Peripheral arterial disease: update of overview and treatment ". *Medicine and Health Rhode Island,* vol. 92, n° 12, p. 398.

Schroll, Marianne, and Ole Munck. 1981. " Estimation of peripheral arteriosclerotic disease by ankle blood pressure: measurements in a population study of 60-year-old men and women ". *Journal of Chronic Disease,* vol. 34, p. 261.

Sepulchre, R., M. Janković and P.V. Kokotović. 1997. *Constructive Nonlinear Control*. W.H. Freeman.

Seraji, H. 1994. " Adaptive Admittance Control - an Approach to Explicit Force Control in Compliant Motion ". *1994 Ieee International Conference on Robotics and Automation: Proceedings, Vols 1-4*, p. 2705-2712.

Sharma, Aditya M., and Herbert D. Aronow. 2012. " Lower Extremity Peripheral Arterial Disease ". In *Traditional and Novel Risk Factors in Atherothrombosis*, < http://www.intechopen.com/books/traditional-and-novel-risk-factors-in-atherothrombosis/lower-extremity-peripheral-arterial-disease >.

Sheth, Pradip N, and John J Uicker. 1971. " A generalized symbolic notation for mechanisms ". *Journal of Manufacturing Science and Engineering,* vol. 93, n° 1, p. 102-112.

Siciliano, Bruno, and Luigi Villani. 1996. " A passivity-based approach to force regulation and motion control of robot manipulators ". *Automatica,* vol. 32, n° 3, p. 443-447.

Siciliano, Bruno, and Luigi Villani. 2000. *Robot Force Control*. Kluwer Academic Publishers, 146 p.

Slotine, J. J. E., and Weiping Li. 1991. *Applied nonlinear control*. Prentice-Hall, Englewood Cliffs, N.J.: Prentice-Hall, xv, 459 p.

Slotine, Jean-Jacques E. 1984. " Sliding controller design for non-linear systems ". *International Journal of Control,* vol. 40, n° 2, p. 421-434.

Speich, John E, and Jacob Rosen. 2004. " Medical robotics ". *Encyclopedia of Biomaterials and Biomedical Engineering,* vol. 983, p. 993.

Stone, Henry W. 1987. *Kinematic modeling, identification, and control of robotic manipulators*, 29. Springer.

Tarn, T., Wu Yunging, Xi Ning and A. Isidori. 1996. " Force regulation and contact transition control ". *Control Systems, IEEE,* vol. 16, n° 1, p. 32-40.

Taubin, Gabriel. 1991. " Estimation of planar curves, surfaces, and nonplanar space curves defined by implicit equations with applications to edge and range image segmentation ". *Pattern Analysis and Machine Intelligence, IEEE Transactions on,* vol. 13, n° 11, p. 1115-1138.

Tee, K. P., R. Yan and H. Z. Li. 2010. " Adaptive Admittance Control of a Robot Manipulator Under Task Space Constraint ". *2010 Ieee International Conference on Robotics and Automation (Icra)*, p. 5181-5186.

Traslosheros, Alberto, José Maria Sebastián, Eduardo Castillo, Flavio Roberti and Ricardo Carelli. 2011. " A method for kinematic calibration of a parallel robot by using one camera in hand and a spherical object ". In *Advanced Robotics (ICAR), 15th International Conference on*. (Tallinn, Estonia, 20-23 June 2011), p. 75-81.

Tsumugiwa, Toru, Ryuichi Yokogawa and Kei Hara. 2002. " Variable impedance control based on estimation of human arm stiffness for human-robot cooperative calligraphic task ". In *Robotics and Automation, 2002. Proceedings. ICRA '02. IEEE International Conference on*. (2002). Vol. 1, p. 644-650 vol.1.

van der Linde, R. Q., and P. Lammertse. 2003. " HapticMaster - a generic force controlled robot for human interaction ". *Industrial Robot-an International Journal,* vol. 30, n° 6, p. 515-524.

Vanderpool, Heidi E., Elizabeth A. Friis, Barbara S. Smith and Kenneth L. Harms. 1993. " Prevalence of carpal tunnel syndrome and other work-related musculoskeletal problems in cardiac sonographers ". *Journal of Occupational medicine,* vol. 35, n° 6, p. 604-610.

Vieyres, Pierre, Gérard Poisson, Fabien Courrèges, Olivier Mérigeaux and Philippe Arbeille. 2003. " The TERESA project: from space research to ground tele-echography ". *Industrial Robot,* vol. 30, n° 1, p. 77-82.

Vieyres, Pierre, Gérard Poisson, Fabien Courrèges, Natalie Smith-Guerin, Cyril Novales and Philippe Arbeille. 2006. " A Tele-Operated Robotic System for Mobile Tele-Echography: The Otelo Project ". In *M-Health: Emerging Mobile Health Systems*, sous la dir. de Istepanian, Robert S. H., Swamy Laxminarayan and Constantinos S. Pattichis. p. 461-473.

Vilchis, Adriana, Jocelyne Troccaz, Philippe Cinquin, Agnes Guerraz, Franck Pelli-sier, Pierre Thorel, Bertrand Tondu, Fabien Courrèges, Gérard Poisson, Marc Althuser and Jean-Marc Ayoubi. 2002. " Experiments with the TER tele-echography robot ". *Proceedings of MICCAI,* vol. 2488, p. 138.

Vilchis, Adriana, Jocelyne Troccaz, Philippe Cinquin, Kohji Masuda and Franck Pellissier. 2003. " A New Robot Architecture for Tele-Echography ". *Robotics and Automation, IEEE Transactions on,* vol. 19, n° 5, p. 922-926.

Waibel, Brian J, and Homayoon Kazerooni. 1991. " Theory and experiments on the stability of robot compliance control ". *Robotics and Automation, IEEE Transactions on,* vol. 7, n° 1, p. 95-104.

Wen, J. T., and Steve Murphy. 1991. " Stability analysis of position and force control for robot arms ". *Automatic Control, IEEE Transactions on,* vol. 36, n° 3, p. 365-371.

Wen, John T., and Kenneth Kreutz-Delgado. 1992. " Motion and force control of multiple robotic manipulators ". *Automatica,* vol. 28, n° 4, p. 729-743.

Whitney, Daniel E. 1987. " Historical Perspective and State of the Art in Robot Force Control "". *The International Journal of Robotics Research,* vol. 6, n° 1, p. 3-14.

Widmer, Leo Karl, A. Greensher and William B. Kannel. 1964. " Occlusion of peripheral arteries: a study of 6,400 working subjects ". *Circulation,* vol. 30, p. 836.

Wimboeck, T., C. Ott and G. Hirzinger. 2006. “ Passivity-based object-level impedance control for a multifingered hand ”. *2006 IEEE/RSJ International Conference on Intelligent Robots and Systems, Vols 1-12*, p. 4621-4627.

Wu, Defeng, Aiguo Li, Zi Ma, Yang Wang and Xiang Wu. 2011. “ Novel approach to calibrate main body of a three-dimensional scanning robotic system ”. *Jixie Gongcheng Xuebao(Chinese Journal of Mechanical Engineering),* vol. 47, n° 17, p. 9-14.

Xueyou, Renyzhuj, and Ye Shenghua. 2007. “Method of robot calibration based on laser tracker ”. *Chinese Journal of Mechanical Engineering,* vol. 9, p. 40.

Yamada, Daisuke, Jian Huang and Tetsuro Yabuta. “ Comparison Between Admittance and Impedance Control of a Multi-Finger-Arm Robot using the Guaranteed Manipulability Method “”. *Precision Instrument and Mechanology*.

Yamane, K. 2011. “ Practical kinematic and dynamic calibration methods for force-controlled humanoid robots ”. In *Humanoid Robots (Humanoids), 2011 11th IEEE-RAS International Conference on*. (26-28 Oct. 2011), p. 269-275.

Yang, Guilin, I-Ming Chen, Song Huat Yeo and Wee Kiat Lim. 2002. “ Simultaneous base and tool calibration for self-calibrated parallel robots ”. *Robotica,* vol. 20, n° 04, p. 367-374.

Yen, Andy Kar Wah. 2011. “ Asservissement en position d'un manipulateur robotique pour l'échographie 3D des artères des membres inférieurs ”. Mémoire de maîtrise électronique, Montréal, École de technologie supérieure

Yongqiang, Ye, Pan Ya-Jun, Y. Gupta and J. Ware. 2011. “ A Power-Based Time Domain Passivity Control for Haptic Interfaces ”. *Control Systems Technology, IEEE Transactions on,* vol. 19, n° 4, p. 874-883.

Yoshikawa, T., T. Sugie and M. Tanaka. 1988. “ Dynamic hybrid position/force control of robot manipulators-controller design and experiment ”. *Robotics and Automation, IEEE Journal of,* vol. 4, n° 6, p. 699-705.

Zeng, Ganwen, and Ahmad Hemami. 1997. “ An overview of robot force control ”. *Robotica,* vol. 15, n° 05, p. 473-482.

Zhao, Longfei, Andy Kar Wah Yen, Jonathan Coulombe, Pascal Bigras and Ilian A. Bonev. 2013. “ Kinematic analyses of a new medical robot for 3D vascular ultrasound examination ”. *Transactions of the Canadian Society for Mechanical Engineering,* vol. 38, n° 2, p. 227-239.

Zhuang, Hangi, and Zvi S Roth. 1996. *Camera-aided robot calibration*. CRC press.

Zhuang, Hanqi. 1994. “ A self-calibration approach to extrinsic parameter estimation of stereo cameras ”. In *Robotics and Automation, 1994. Proceedings., 1994 IEEE International Conference on*. p. 3428-3433. IEEE.

Zhuang, Hanqi, Jiahua Yan and Oren Masory. 1998. “ Calibration of stewart platforms and other parallel manipulators by minimizing inverse kinematic residuals ”. *Journal of Robotic Systems,* vol. 15, n^{o} 7, p. 395-405.